2018-12-01

Two-Phase Interactions on Superhydrophobic Surfaces

Kimberly Ann Stevens
Brigham Young University

Two-Phase Interactions on Superhydrophobic Surfaces

Kimberly Ann Stevens

A dissertation submitted to the faculty of
Brigham Young University
in partial fulfillment of the requirements for the degree of

Doctor of Philosophy

Brian D. Iverson, Chair
Julie Crockett
Daniel Maynes
Matthew R. Jones
Dongjin Seo

Department of Mechanical Engineering

Brigham Young University

ABSTRACT

Two-Phase Interactions on Superhydrophobic Surfaces

Kimberly Ann Stevens
Department of Mechanical Engineering, BYU
Doctor of Philosophy

Superhydrophobic surfaces have gained attention as a potential mechanism for increasing condensation heat transfer rates. Various aspects related to condensation heat transfer are explored. Adiabatic, air-water mixtures are used to explore the influence of hydrophobicity on two-phase flows and the hydrodynamics which might be present in flow condensation environments. Pressure drop measurements in a rectangular channel with one superhydrophobic wall (cross-section approximately 0.37×10 mm) are obtained, revealing a reduction in the pressure drop for two-phase flow compared to a control scenario. The observed reduction is approximately 10% greater than the reduction that is observed for single-phase flow (relative to a classical channel).

Carbon nanotubes have been used to create superhydrophobic coatings due to their ability to offer a relatively uniform nanostructure. However, as-grown carbon nanotubes often require the addition of a thin-film hydrophobic coating to render them superhydrophobic, and fine control of the overall nanostructure is difficult. This work demonstrates the utility of using carbon infiltration to layer amorphous carbon on multi-walled nanotubes to achieve superhydrophobic behavior with tunable geometry. The native surface can be rendered superhydrophobic with a vacuum pyrolysis treatment, with contact angles as high as 160° and contact angle hysteresis less than 2–3°.

Drop-size distribution is an important aspect of heat transfer modeling that is difficult to measure for small drop sizes. The present work uses a numerical simulation of condensation to explore the influence of nucleation site distribution approach, nucleation site density, contact angle, maximum drop size, heat transfer modeling to individual drops, and minimum jumping size on the distribution function and overall heat transfer rate. The simulation incorporates the possibility of coalescence-induced jumping over a range of sizes. Results of the simulation are compared with previous theoretical models and the impact of the assumptions used in those models is explored. Results from the simulation suggest that when the contact angle is large, as on superhydrophobic surfaces, the heat transfer may not be as sensitive to the maximum drop-size as previously supposed. Furthermore, previous drop-size distribution models may under-predict the heat transfer rate at high contact angles.

Condensate drop behavior (jumping, non-jumping, and flooding) and size distribution are shown to be dependent on the degree of subcooling and nanostructure size. Drop-size distributions for surfaces experiencing coalescence-induced jumping are obtained experimentally. Understanding the drop-size distribution in the departure region is important since drops in this size are expected to contribute significantly to the overall heat transfer rate.

Keywords: superhydrophobic surfaces, condensation, two-phase flow, drop-size distribution

ACKNOWLEDGMENTS

The work descried in this dissertation is the result of the efforts and influence of numerous people. First, my committee chair, Brian Iverson, has always been incredibly supportive. He, Julie Crockett, and Daniel Maynes have each taught me important lessons that have and will continue to guide me throughout my professional life. I have also had the privilege of working with fantastic undergraduate students, including Joseph Seamons, Clint Hubbard, Jacob Butterfield, Taylor Davis, Courtney Nordgran, and Jonathon Erickson; their work is found throughout the dissertation. Similarly, I treasure my friendships with fellow graduate students in the lab, past and present. Finally, Kevin Cole was an incredible help countless times, and I am grateful for the work he, Jim Fraser, and Nick Hawkins do that made this research possible.

I am grateful to Brigham Young University and the its sponsoring organization, the Church of Jesus Christ of Latter-day Saints, for the education I have received and the atmosphere in which it was administered. I gratefully acknowledge the funding sources that supported this research, including the Utah Space Grant Consortium.

My family has been a support, inspiration, and joy to me for the duration of my PhD and throughout my life. Most of all, I am grateful to my Heavenly Father and Jesus Christ for the guidance I received in my research and the lessons I learned during graduate school.

TABLE OF CONTENTS

LIST OF TABLES

LIST OF FIGURES

NOMENCLATURE

A	Area of the domain (m^2)
A_b	Total area covered by the drop base (m^2)
A_c	Area over which condensation occurs (m^2)
Bi	Biot number
c_p	Heat exchanger coolant heat capacity (J/kg·K)
d	Shortest distance between the surfaces of two drops (m)
d_s	Shortest distance between the surfaces of two drops as one sweeps (m)
D_h	Hydraulic diameter (m)
F	Frictional component of the pressure gradient
F_C	Cavity fraction
h_{fg}	Latent heat of vaporization (J/kg)
j	Superficial fluid velocity (m/s)
l	Average spacing between structures (m)
$< L >$	Average spacing between nucleation sites (m)
H	Channel height
$\dot{m}$	Mass flow rate (kg/s)
N	Drop-size distribution (drops/m^3)
N_s	Nucleation site density (drops/m^2)
n	Number of drops on the surface
n_{new}	Number of new drops that are added in a time step
P	Pressure (Pa)
q_d	Rate of heat transfer to an individual drop (W)
q"	Time-averaged heat flux (W/m^2)
$q"_g$	Heat flux measured based on the temperature gradient in the copper block (W/m^2)
$q"_{\Delta T}$	Heat flux measured based on the change in heat exchanger coolant temperature (W/m^2)
$q"_{inst}$	Instantaneous heat flux (W/m^2)
r	Radius of a simulated drop (m)
$\hat{r}$	Average maximum radius of the drops (m)
r_{CCA}	Radius at which the drop transitions from a variable to constant contact angle (m)
r_e	Radius at which growth transitions from direct-condensation-dominated growth (m) to coalescence-dominated growth (m)
r_j	Minimum size of drops allowed to depart via coalescence-induced jumping (m)
r_{max}	Size at which drops are shed from the surface via gravity (m)
r_{max10}	Average of the 10 largest drops in a single video frame (m)
r_{min}	Size from which drops begin to grow (m)
r_s	Surface roughness
r_{thermo}	Smallest thermodynamically viable drop (m)
Re_L	Liquid-only Reynolds number
Re_G	Gas-only Reynolds number
R	Radius of curvature (m)
ΔT	Degree of surface subcooling (degree K)
δt	Time step size (s)
t	Time elapsed since condensation commenced (s)

T_c	Temperature of the copper block (degree K)
T_{HXin}	Coolant bulk temperature before entering the heat exchanger (degree K)
T_{HXout}	Coolant bulk temperature after exiting the heat exchanger (degree K)
T_s	Temperature of the condensing surface (degree K)
T_{sat}	Saturation temperature (degree K)
U	Overall heat transfer coefficient (W/m^2·K)
U_{HX}	Overall heat transfer coefficient between the heat exchanger coolant and the (W/m^2·K) copper block (W/m^2·K)
V	Volume of collected condensate (m^3)
$\dot{V}$	Volumetric flow rate (m^3/s)
V_{new}	Drop volume at the beginning of a time step (m^3)
V_{old}	Drop volume at the end of a time step (m^3)
w_c	Width of the cavity between the ribs (m)
W	Channel width (m)
x	Vapor quality (chapter 2) or X-location of the center of mass of a simulated drop (m) (chapter 4)
y	Y-location of the center of mass of a simulated drop (m)
Z	Coordinate orientated along the length of the channel (m)
χ	Martinelli parameter
η	Aspect ratio of the channel, H/W
γ	Solid-liquid surface tension (N/m)
μ	Viscosity (kg/ms)
ϕ^2	Two-phase multiplier
σ	Surface tension (N/m)
ρ	Density of the liquid phase (kg/m^3)
θ	Solid-liquid contact angle (°)
θ_a	Intrinsic contact angle (°)
θ_a^{CB}	Apparent contact angle on a superhydrophobic surface in the Cassie-Baxter state(°)
θ_a^{CB}	Apparent contact angle on a superhydrophobic surface in the Wenzel state(°)
τ	Sweeping period (s)

Subscripts, superscripts, and other indicators

$[\,]_p$	Primary drop
$[\,]_s$	Sweeping drop
$[\,]_i$	Secondary, tertiary, and additional drops
$[\,]_{HL}$	Hydrophilic Surface
$[\,]_{SH}$	Superhydrophobic Surface
$[\,]_L$	Liquid phase
$[\,]_G$	Gas phase
$[\,]_M$	Measured
$[\,]_P$	Predicted
$[\,]_{TP}$	Two-phase

CHAPTER 1. INTRODUCTION

1.1 Motivation and Dissertation Organization

The need for more efficient condensation is compelling, affecting in some way the life of every person on earth through our dependence on energy, clean water, and electronics. The majority of the electricity produced globally is generated using the Rankine cycle, the efficiency of which is directly related to condensation heat transfer performance [1, 2]. Nearly one billion people world-wide lack access to clean water, and boiling/re-condensing salt water is one approach to produce pure drinking water [3]. The demand for improved heat dissipation remains constant with increasingly high power densities in electronics, and condensation is involved in a variety of current and proposed electronics cooling devices, including traditional and oscillating heat pipes [4]. Recently, superhydrophobic surfaces have gained much media and scholarly attention as a promising approach for achieving higher condensation rates, but much work remains before they are viable for use in next generation condensing devices.

The present work provides insight regarding issues relevant to increasing condensation heat transfer rates through the use of superhydrophobic surfaces. The motivation of the research was to produce results that were not only novel and interesting from a scientific standpoint, but useful in furthering the quest for more efficient condensation heat transfer. Though distinct in their approach and contribution, each chapter focuses on a different aspect of condensation heat transfer improvement, as enumerated below.

1. In chapter 2, the hydrodynamics in adiabatic two-phase channel flow are quantified, providing insight regarding how the driving pressure force in a superhydrophobic channel changes relative to classical channels. Two-phase channel flows are studied to better understand internal-flow condensation processes. The flow behavior, including hydrodynamics, often significantly impacts the heat and mass transfer in two-phase flows, making it relevant to the problem of condensation heat transfer [5].

2. In chapter 3 a process for manufacturing superhydrophobic surfaces is described offering control of the nanostructure. A nanostructure is necessary to avoid flooding during condensation on a superhydrophobic surface, and evidence suggests that the characteristics of the nanostructure directly influences the heat transfer rate. Furthermore, one challenge with superhydrophobic surfaces is their durability. The work describes a method for creating more robust superhydrophobic surfaces.

3. In chapter 4 an approach to obtain detailed drop-size distributions, an important aspect of condensation heat transfer modeling, is presented, and the influence of various parameters on distribution and predicted overall heat transfer rate are reported. The model accounts for coalescence in small drop sizes and allows for coalescence-induced departure over a range of drop-sizes, in contrast to existing models.

4. In chapter 5 the influence of subcooling and nanostructure on condensate wetting state and drop-size distribution are explored experimentally. The wetting state directly influences condensation heat transfer rates, and improved understanding of the cause and influence of the wetting state transition is necessary for superhydrophobic condenser design.

5. In chapter 6 preliminary heat transfer measurements on surfaces experiencing coalescence-induced jumping are obtained.

This dissertation is organized as follows. The remainder of this chapter highlights particularly relevant background information regarding condensation on superhydrophobic surfaces. Chapters 2-5 present the contributions outlined above as prepared for archival journals. Accordingly, each chapter contains an abstract, introduction, brief review of relevant literature, and conclusion in addition to the description of new work. Chapter 6 describes preliminary work, preparatory for additional work which will eventually be prepared for publication. Chapter 7 draws conclusions from the work as a whole and discusses future work.

1.2 Condensation Heat Transfer

1.2.1 Dropwise and Flimwise Condensation

Heterogeneous condensation occurring on a solid surface will result in formation of a film (filmwise condensation) or discrete drops (dropwise condensation), depending on the wettability of the surface and degree of subcooling. In both cases, condensate can be removed by gravity, acceleration, and/or vapor-flow-induced shear stresses. However, the presence of a liquid film creates high thermal resistance to heat transfer, generally resulting in lower heat transfer coefficients relative to dropwise condensation. One oft-sited study measured a 5-7 times improvement in heat transfer coefficient for dropwise condensation relative to filmwise condensation, leading to great interest in the creation of surfaces which can maintain dropwise condensation [6]. Traditionally, such surfaces are created by modifying the wettability of the surface. The use of superhydrophobic surfaces is an extension of the pursuit for improved heat transfer rates through surface modification.

1.2.2 Influence of Noncondensable Gases

The condensation heat transfer rate is extremely sensitive to the presence of small concentrations (even a few ppm) of noncondensable gases (NCG) during both film and dropwise condensation [7–12]. The presence of NCG results in formation of a water vapor/air boundary layer through which water vapor must diffuse to reach a condensing surface. The boundary layer thickness is dependent on the spatial distribution of drops, shape of the surrounding apparatus, and time since condensation initiation. While heat transfer data obtained in the presence of NCG may illustrate trends in heat transfer performance, they are not useful for comparison due to the dependence of performance on the characteristics of the boundary layer [8]. The difficulty of maintaining a system free from non-condensable gases is often used as an explanation for the large discrepancies in measured condensation heat transfer coefficients [7]. NCG are assumed to be absent in the numerical simulation described in chapter 4 of this work, and great care is taken to minimize the NCG concentration in the experimental work described in chapter 5.

1.3 Superhydrophobic Surfaces

In addition to modifying the native surface chemistry to promote dropwise condensation, the addition of surface structures has also been used to enhance condensation. The combination of a rough surface with an intrinsically high contact angle (achieved by roughening a natively hydrophobic surface or rendering hydrophobic a rough hydrophilic surface) can result in a superhydrophobic surface with a solid-liquid contact angle greater than 150° and contact angle hysteresis less than 10° [13, 14].

Contact angle hysteresis is the difference between the advancing and receding contact angles, and low hysteresis is indicative of high droplet mobility [15]. Advancing and receding angles are the maximum and minimum contact angles a drop experiences, such as when volume is being added to or subtracted from a static droplet. Both the advancing and receding contact angles are necessary to fully characterize a surface since a static contact angle could be measured at any angle between the advancing and receding contact angles [14, 16]. Gao and McCarthy reviewed the findings of several investigators emphasizing the importance of the advancing and receding contact angles [16]. However, measurement of the static contact angle is more convenient, and on superhydrophobic surfaces suitable for condensation the hysteresis is so low that the static contact angle is frequently used to characterize the surface in practice. Nevertheless, the static contact angle is sensitive to the interactions at the three-phase contact line and not necessarily indicative of the hydrophobicity of the surface anywhere, including directly beneath the drop, besides the three-phase contact line.

When a stationary droplet is placed on top of a rough, superhydrophobic surface, surface tension can prevent the liquid from penetrating into the cavities, creating a layer of air between the solid and liquid surfaces. In this case, the droplet is said to be in a non-wetting, or Cassie state. If the pressure in the liquid is too high, it will overcome surface tension and liquid will enter the cavities; the surface is then said to be in a wetting, or Wenzel state. An estimate for the pressure required for the liquid to wet a superhydrophobic surface is traditionally given by the Laplace pressure, given by the Young-Laplace Equation,

$$\Delta P = P_{\text{water}} - P_{\text{air}} = \gamma\left(\frac{1}{R_1} + \frac{1}{R_2}\right), \tag{1.1}$$

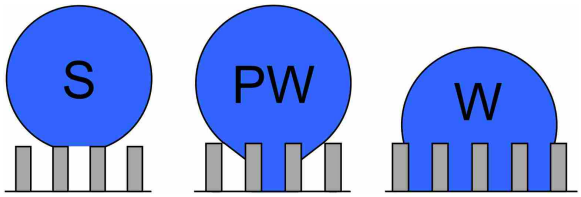

Figure 1.1: Schematics showing suspended (S), partially wetting (PW), and wetting (W) drop mythologies, adapted from work by Miljkovic *et al.* [17].

where γ is the surface tension, R_1 and R_2 are the surface radii of curvature. The Cassie/Wenzel distinction in wetting state and Young-Laplace equation applies to liquid initially external to the surface cavities, as when liquid is placed or impinged on or flowed over a surface (see chapter 2). When water originates within the structure cavities, as occurs during condensation, different distinctions in wetting state are appropriate (see chapter 5).

1.4 Condensation on Superhydrophobic Surfaces

For years researchers believed that superhydrophobic surfaces were not beneficial for condensation since condensing drops always wet the structures and were highly pinned. Initial investigations of condensation on superhydrophobic surfaces found that the nucleation sites for condensation were evenly spread over the entire surface. As a result, a significant percentage of the initial condensate drops formed within the cavities, resulting in an irreversibly wetted state with highly pinned, immobile drops deleterious to heat transfer [18–20, 20–25]. However, Chen *et al.* [26] showed that drops can grow out of the structure cavities in a non-wetting state when the surface has two-tiered (nano- and microscale) roughness, renewing interest in condensation on superhydrophobic surfaces. Formation of condensate drops in a non-wetting state on surfaces with nanoscale or two-tiered roughness was observed by other investigators [27–33], and eventually a consensus emerged that two-tiered structuring was not necessary to avoid wetting. Highly mobile drops of condensate in a non-wetting state have been found on surfaces both with [34–36] and without a microstructure, [29, 30, 37–39] as long as a nanostructure is present. Enright *et al.* developed a model to predict drop morphology [29], and researchers have observed that condensing drops can emerge in one of three states: wetted, partially wetted, or suspended as illustrated in Figure 1.1 [8]. Suspended drops nucleate on the tops of the structures, and will remain on top of the

structures as they grow if it is energetically favorable to do so. Wetted and partially wetted drops begin growing from nucleation sites within the surface structure. Depending on the surface structure, wettability, and nucleation density, drops will either grow up out of the structure (partially wetted) or they will merge with other drops and continue to to grow within the structures (wetted). Drops which are wetted fill the cavities between structures, similar to the traditional Wenzel state. When drops are in the wetted state they will eventually flood the surface, leading to formation of a film and generally poor heat transfer performance.

1.4.1 Coalescence-Induced Jumping

Superhydrophobic surfaces make possible coalescence-induced jumping, which can significantly alter condensation dynamics. When two drops coalesce on a surface with sufficiently low surface energy, the resulting drop can jump normal to the condensing surface. First described by Kollera and Grigull for mercury drops [40], interest in the phenomenon was revived when Boreyko and Chen demonstrated the phenomenon for water drops on superhydrophobic surfaces [41]. Coalescence-induced jumping results from the surface energy released by the drop merger. When the liquid bridge between the coalescing drops impinges on the substrate surface, this bridge pushes the drop away from the substrate if the adhesive force between the merged drop and the surface is smaller than the impinging force, as shown in Figure 1.2. On vertically oriented surfaces, the departed drop can be completely removed as it jumps away from the surface and then falls due to gravity. Coalescence-induced drop removal has been demonstrated for drops as small as 1 μm in diameter [42–44]. The possibility for small drop removal captured the attention of researchers as a possible mechanism for improving heat transfer rates and potential application in a variety of other phase-change driven systems [45–47].

1.4.2 Use of Superhydrophobic Surfaces as a Mechanism for Heat Transfer Enhancement

Existing heat transfer models suggest the majority of the heat transfer during condensation takes place on small drops, and experimental evidence suggests that the heat transfer coefficient increases as the maximum drop size decreases [7]. With the increased mobility of non-wetted drops and the potential for spontaneous jumping, superhydrophobic surfaces can facilitate drop re-

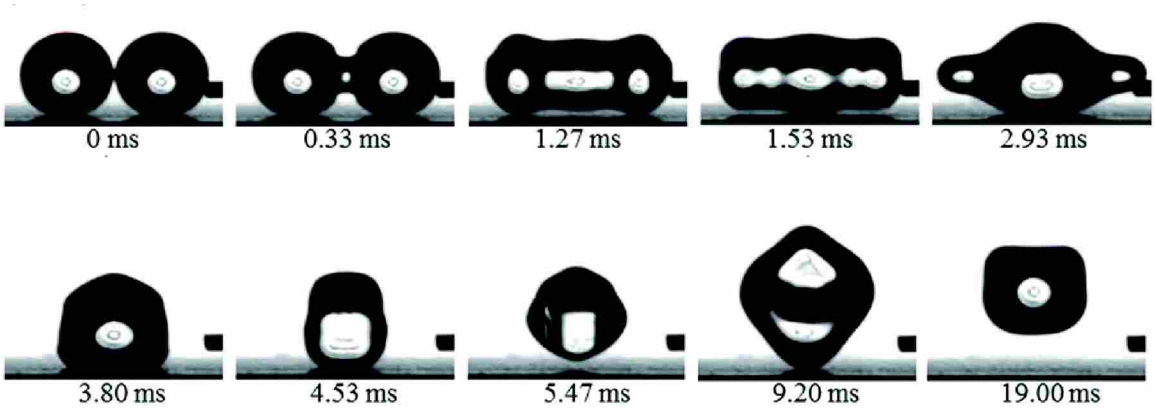

Figure 1.2: Time-lapse images of coalescence-induced jumping, adapted from work by Wang *et al.* [48].

moval at sizes significantly smaller than the capillary length, which is the traditional limit for drop removal due to gravity-induced sweeping. The idea that minimizing the maximum drop size to increase heat transfer rates, achievable with superhydrophobic surfaces, has inspired considerable research activity. Several works have quantified metrics which indirectly relate to the heat transfer rate, such as maximum droplet diameter, coarse drop size distributions, and individual droplet growth rates [34, 39, 49–55]. Additionally, several models for condensation on superhydrophobic surfaces have been developed [17, 39, 55, 56]. However, only a few works have experimentally measured the overall heat transfer rate directly, and their primary focus was on the heat transfer enhancement that could be achieved with superhydrophobic surfaces relative to traditional surfaces [35, 51, 52, 57, 58]. The studies found an improvement in heat transfer performance when drops were in a suspended or partially wetting state. Wen *et al.* measured the heat transfer enhancement that could be obtained by varying the height and microstructure spacing for a specific type of nanostructure [51, 57, 58]. Structure geometry (height, spacing, size, two-tiered vs nano) affects heat transfer performance, but the relationship between structure design and heat transfer rate is not clear. Furthermore, surfaces on which drops were initially in a partially wetting or suspended state can transition to wetting with increased subcooling. Wen *et al.* demonstrated that with densely spaced nanostructures, the wetting transition can be delayed [51, 57, 58]. Though additional understanding regarding the relationship between the surface structure, wetting transition, subcooling and heat transfer performance is needed, superhydrophobic surfaces have exhibited great promise in their potential to improve condensation heat transfer rates.

CHAPTER 2. TWO-PHASE FLOW PRESSURE DROP IN SUPERHYDROPHOBIC CHANNELS

This chapter is published in the International Journal of Heat and Mass Transfer [59]. The format of this paper has been modified to meet the stylistic requirements of this dissertation.

2.1 Contribution Authors and Affiliations

Kimberly A. Stevens, Julie Crockett, Daniel Maynes, Brian D. Iverson
Department of Mechanical Engineering, Brigham Young University, Provo, Utah 84602

2.2 Abstract

Superhydrophobic surfaces have been shown to reduce drag in single-phase channel flow; however, little work has been done to characterize their drag-reducing ability found in two-phase flows. Adiabatic, air-water mixtures were used to explore the influence of hydrophobicity on two-phase flows and the hydrodynamics which might be present in flow condensation environments. Pressure drop measurements in a rectangular channel with one superhydrophobic wall (cross-section approximately 0.37 $\times$ 10 mm) and three transparent hydrophilic walls were obtained. Data for air/water mixtures with superficial Reynolds numbers ranging from 22–215 and 55–220, respectively, were obtained for superhydrophobic surfaces with three different cavity fractions. Agreement between experimentally obtained two-phase pressure drop data and correlations in the literature for conventional smooth control surfaces was better than 20 percent, which is within the accuracy of the correlations. The data reveal a reduction in the pressure drop for two-phase flow in a channel with a single superhydrophobic wall compared to a control scenario. The observed reduction is approximately 10 percent greater than the reduction that is observed for single-phase flow (relative to a classical channel).

2.3 Introduction

Superhydrophobic surfaces have recently gained media and scholarly attention due to their drag-reducing, self-cleaning, and ice-preventing properties. One particularly promising application for superhydrophobic surfaces is in condensation. It has been shown that condensation on superhydrophobic surfaces promotes drop-wise condensation; drop-wise condensation is known to increase heat transfer around 5–7 times relative to film-wise condensation [7, 60]. A number of researchers have explored condensation on superhydrophobic surfaces and found potential for improving heat transfer rates [35, 39, 41].

Increased heat transfer rates would benefit a number of applications such as desalination, energy conversion [61], atmospheric water harvesting [62, 63], and other high heat flux applications involving condensation [64]. However, very little work has been done with condensation on superhydrophobic surfaces in a flow environment. The objective of this work is to investigate the effect of hydrophobicity on the hydrodynamics of an adiabatic two-phase channel flow.

2.3.1 Superhydrophobic Surfaces

A superhydrophobic surface has a solid-liquid contact angle (CA) greater than 150° [13], as shown in Figure 2.1a, and contact angle hysteresis less than 10°.

Superhydrophobic surfaces can be created by combining micro- or nano-structured features with a hydrophobic surface coating. When a static droplet rests on top of a superhydrophobic surface, surface tension can prevent the liquid from penetrating into the cavities, creating a layer of air between the solid and liquid surfaces, as shown in Figure 2.1. In this case, the droplet is said to be in a non-wetting, or Cassie state. If the pressure in the liquid is high, it can overcome the surface tension and liquid will enter the cavities; the droplet is then said to be in a wetting, or Wenzel state. The Young-Laplace equation describes the surface tension-induced pressure difference between two static fluids:

$$\Delta P = P_{water} - P_{air} = \gamma(\frac{1}{R_1} + \frac{1}{R_2}) \tag{2.1}$$

where γ is the surface tension, and R_1 and R_2 are the surface radii of curvature. For superhydrophobic microribs, where R_2 goes to ∞ it can be shown that an approximate threshold for the pressure

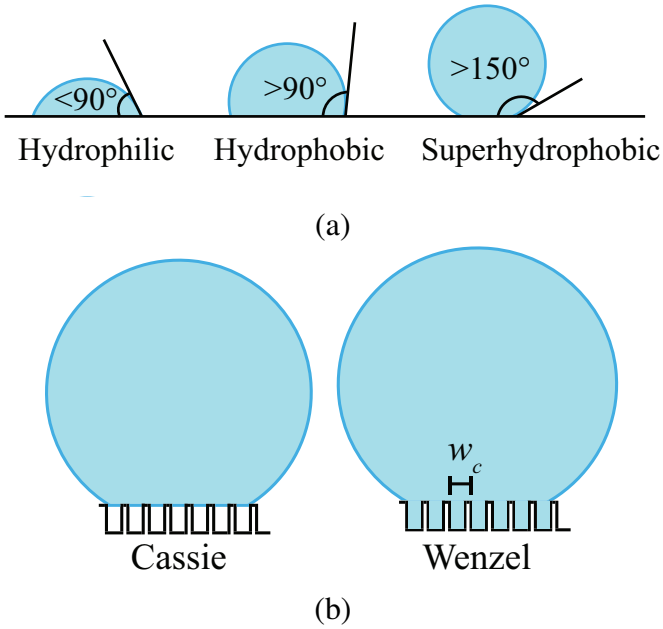

Figure 2.1: (a) The solid-liquid contact angle determines the hydrophobicity of a surface. Hydrophilic surfaces have a contact angle less than 90°, while hydrophobic surfaces have contact angles greater than 90°. Superhydrophobic surfaces have a solid-liquid contact angle of greater than 150°. (b) For a non-wetting droplet (Cassie state), the liquid interacts with a fraction of the substrate surface. In a Wenzel state, liquid fills surface cavity structures, as shown on right.

required to wet the surface, or the Laplace pressure, is

$$\Delta P = -\frac{2\gamma cos(\theta)}{w_c} \tag{2.2}$$

where θ is the contact angle for a droplet on a smooth surface, and w_c is the width of the cavity between the ribs.

2.3.2 Adiabatic Two-Phase Flow

Adiabatic two-phase flows composed of a liquid and gas are commonly studied to gain insight into condensing and boiling flows. In adiabatic flows, the vapor fraction and flow regime do not change along the length of the channel, thereby isolating the hydrodynamic phenomena. In this manner, the time-average streamwise pressure gradient, vapor fraction, and flow regime are constant for a given liquid/gas mixture in a channel flow.

Early work by Lockhart and Martinelli [65] and Chisholm and Laird [66, 67] laid the foundation for predicting the pressure gradient for two-phase flow in channels. In their work, the two-phase pressure gradient is expressed in terms of a two-phase multiplier, ϕ^2, which is the two-phase pressure gradient normalized by the single-phase pressure gradient that would result if the liquid (subscript L) or gas (subscript G) component of the two-phase flow was the only fluid in the channel,

$$\phi_L^2 = (\frac{\mathrm{d}P}{\mathrm{d}z}F)_{\mathrm{TP}}/(\frac{\mathrm{d}P}{\mathrm{d}z}F)_{\mathrm{L}} \tag{2.3}$$

$$\phi_G^2 = (\frac{\mathrm{d}P}{\mathrm{d}z}F)_{\mathrm{TP}}/(\frac{\mathrm{d}P}{\mathrm{d}z}F)_{\mathrm{G}} \tag{2.4}$$

Here, F denotes the component of the pressure gradient necessary to overcome friction, as opposed to that associated with a phase change or gravity. The multipliers are often correlated in terms of the Martinelli parameter, χ, which is a ratio of the gas to liquid two-phase multiplier,

$$\chi = [(\frac{\mathrm{d}P}{\mathrm{d}z}F)_{\mathrm{L}}/(\frac{\mathrm{d}P}{\mathrm{d}z}F)_{\mathrm{G}}]^{1/2} \tag{2.5}$$

In practice, χ reduces to:

$$\chi = \frac{\dot{m}_{\mathrm{L}}}{\dot{m}_{\mathrm{G}}}\sqrt{\frac{\rho_{\mathrm{G}}}{\rho_{\mathrm{L}}}} = \sqrt{\frac{\mu_{\mathrm{L}}\dot{V}_{\mathrm{L}}}{\mu_{\mathrm{G}}\dot{V}_{\mathrm{G}}}} \tag{2.6}$$

Chisholm and Laird [66] found that the two-phase multipliers could be roughly correlated with the Martinelli parameter using the following relations:

$$\phi_L^2 = 1 + \frac{C}{\chi} + \frac{1}{\chi^2} \tag{2.7}$$

$$\phi_G^2 = 1 + C\chi + \chi^2 \tag{2.8}$$

where C is a constant, dependent on the flow regime of the liquid and gas phases. Though it is known that these correlations deviate significantly from reality for many flow conditions, they are the basis for much of the two-phase flow work that followed. Dozens of correlations exist for predicting two-phase flow for a variety of channel geometries and orientations, working fluids, and

velocities. Sun and Mishima [68] and Asadi *et al.* [69] have provided excellent reviews specifically for mini- and micro-channel flows. Kim and Mudawar developed a universal correlation for a wide range of fluids, flow rates, and channel shapes, constructed from over 7000 data points compiled from over 36 studies [70, 71]. However, with all the work that has been done for pressure drop in two-phase flow, there has been limited discussion of the effect of surface wettability, and even less exploration of the specific influence of the combination of structuring and hydrophobicity associated with superhydrophobic surfaces.

Wettability and Two-Phase Flow

It is recognized that changing the contact angle has an influence on the transition between the flow regimes that occur in two-phase flow [72,73]. Huh *et al.* [74] observed more flow regimes for hydrophobic than hydrophilic microchannels for contact angles in the range CA = 35 to 111°. Barajas and Panton [75] found different flow maps for hydrophilic relative to hydrophobic 1.6 mm I.D tubes with contact angles in the range CA = 34 to 106°. The degree of influence of wettability on flow regime transition is likely to vary with factors such as the size of the channel, since the boundary condition will exert a larger influence on a smaller channel; however, each of the studies above showed that wettability did influence the location of the flow regime transition.

While it is clear that wettability influences the flow regime, there is wide disagreement between studies on the effect of wettability on pressure drop. Takamasa *et al.* [76] found the effect of wettability for contact angles in the range of CA = 7 to 146° to be insignificant on the pressure drop in fairly large 20 mm diameter tubes. Phan *et al.* [77] investigated flow boiling in a 0.5 $\times$ 5 mm rectangular channel with surface contact angles of 26, 49, 63 and 103°, mass fluxes of 100 and 120 kg/m^{2}s, and a vapor quality range of 0.01–0.06. They found that a higher contact angle leads to higher pressure drop. Cho and Wang [72] observed differences in pressure drop for three surfaces of varying wettability (CA = 80, 103, and 124°). The surface with the highest contact angle had a significantly higher pressure drop, but it was also much rougher than the other surfaces. There was no conclusive difference in pressure drop between the other two surfaces. Choi *et al.* [78] measured flow in two different 530 $\times$ 499 μm channels with walls exhibiting contact angles of 25° and 105°, respectively. The liquid and air superficial velocities ranged from 0.25–0.43 m/s and 4.5–40 m/s, respectively. They found that the hydrophobic channel had a smaller

pressure drop, but also pointed out that the fluid was in a different flow regime. Wang *et al.* [79] observed a decrease in pressure drop for two-phase flow in a square channel (4 mm $\times$ 4 mm) with a superhydrophobic surface created from randomly distributed silica particles coated with PDMS (CA = 155°) of approximately 40%. The vapor quality ranged from 0.2–0.4 with a single superficial liquid velocity of 0.015 m/s and superficial gas velocities ranging from approximately 3 to 9 m/s.

In summary, there are inconsistent findings in the literature on the effect of wettability on two-phase flow pressure drop. The variation can be accounted for by the fact that the range of flow rates and channel sizes tested, as well as the degree of hydrophobicity, likely influence the effect of wettability on two-phase pressure drop. In single-phase liquid flows in the Cassie state, it is well established that channels with superhydrophobic walls experience a reduction in pressure drop due to the slip that occurs at the wall (shear-free condition above a gas-filled cavity), and this reduction in pressure drop becomes more significant with smaller channels [80–84]. It is significant to note that in the studies cited above, only two included superhydrophobic surfaces. Of those, only one used a channel sufficiently small that the presence of a superhydrophobic boundary would cause a measureable decrease in pressure drop. Therefore, it is not surprising that this is the only study that found a reduction in pressure drop. With the exception of the study by Wang *et al.* [79], the influence of a superhydrophobic microchannel wall on two-phase pressure drop has not been explored. The focus of the Wang *et al.* paper was to determine how superhydrophobic surfaces affect the performance of polymer electrolyte membrane fuel cells. For their application, an appropriately narrow range of flow rates was explored. Other potential applications of two-phase flow on superhydrophobic surfaces, such as flow boiling or flow condensation, would span a much larger range of flow rates. Data for a wider range of flow rates is necessary to understand how superhydrophobic surfaces influence two-phase pressure drop.

As fundamental understanding of condensation on superhydrophobic surfaces continues to improve, exploration of condensation behavior will move from quiescent vapor environments to more industrially relevant, internal flow environments. Torresin *et al.* [85] performed experiments with flow condensation in superhydrophobic channels and found that the shear provided by the vapor flow can decrease droplet departure size, which has tremendous implications for heat transfer. Birbarah and Miljkovic [86] proposed that a convective environment could entrain drops that have

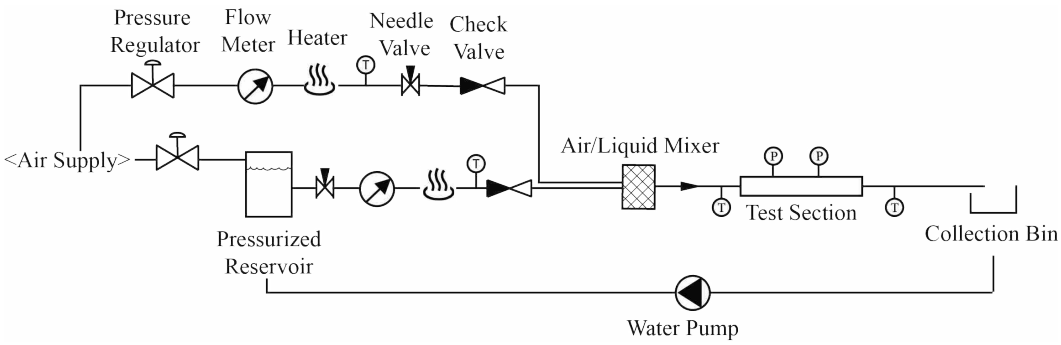

Figure 2.2: Schematic of the air/water, two-phase flow loop.

departed the surface due to coalescence induced jumping, preventing their return to the surface and thereby improving heat transfer. The potential for superhydrophobic surfaces in a flow-condensing environment lies not only in its drag reducing abilities, but in its ability to improve heat transfer rates. Understanding of the fundamental fluid dynamics governing two-phase flows over superhydrophobic surfaces will become increasingly important as exploration of flow condensation on superhydrophobic surfaces continues. The results of the present study are an important initial contribution to the understanding of how flow rate impacts the pressure drop in a channel with superhydrophobic walls

This paper specifically addresses how the pressure drop of a two-phase (air and water) flow is affected when flowing in a channel with a single superhydrophobic wall. Comparison is made relative to classical channels for a range of flow rates corresponding to superficial gas and liquid Reynolds numbers from 22–215 and 55–220 (superficial velocities from 0.48–4.7 and 0.07–0.29 m/s), respectively. These ranges result in a vapor quality range from 0.002 to 0.08, which is much lower than that explored by Wang *et al.* [79] and includes multiple liquid flow rates.

2.4 Methods

An adiabatic flow loop was designed and constructed to measure and observe two-phase channel flow, as shown in Figure 2.2. Compressed air was used to pressurize a tank containing deionized water. The air and water flow rates were controlled with needle valves and pressure regulators and then measured with in-line flow meters (Omega FLR1004-D, 200-1000 mL/min with accuracy $\pm$ 30 mL/min and Omega FLR1007, 13–100 mL/min with accuracy $\pm$ 1 mL/min).

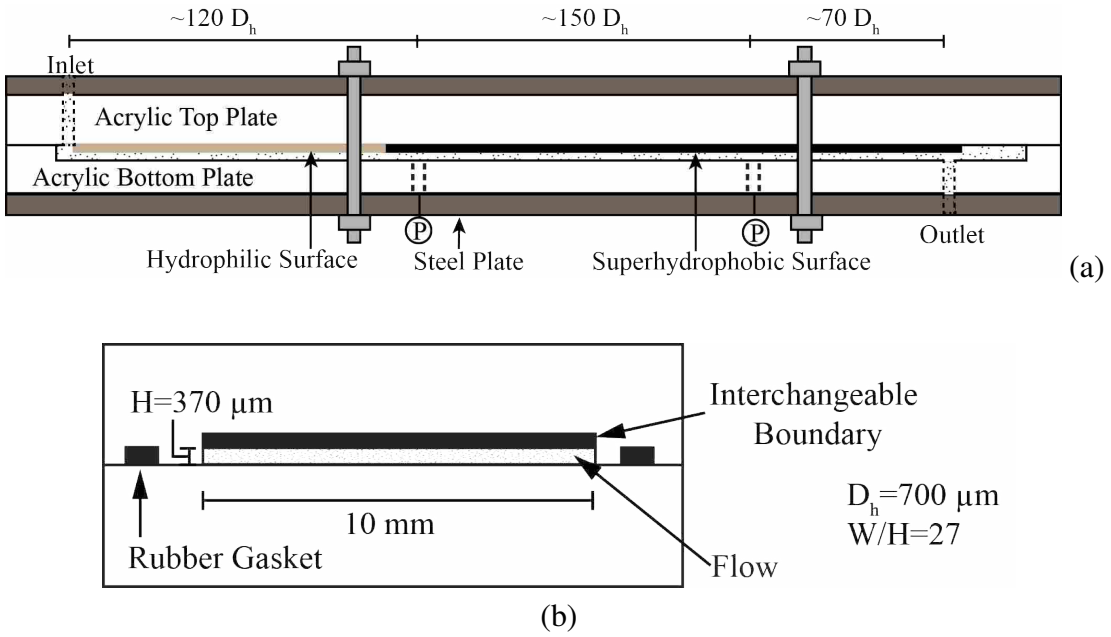

Figure 2.3: (a) Test section schematic with a hydraulic diameter of 700 $\pm$ 30 μm, height of 370 $\pm$ 10 μm, and width to height ratio of 27. A cross-sectional view of the channel is shown in (b) with gasket seal.

The air and water flows were mixed in a 1/16 inch T-shaped junction before entering the rectangular channel detailed in Figure 2.3a. The flow was allowed to develop for approximately 120 hydraulic diameters before the differential pressure (Omega PX409-2.5DWU5V, accuracy $\pm$ 0.02 psi) was measured across the test section, which had a length of approximately 150 hydraulic diameters. The taps leading to the pressure transducer were filled with water, and positioned on the bottom of the channel to prevent air bubbles from entering the taps. The flow exited the test section to atmosphere approximately 70 hydraulic diameters downstream from the downstream pressure tap. Temperature was measured with T-type thermocouples directly upstream and downstream of the test section. Flow rate, pressure, and temperature were recorded at 200 Hz. The pressure signal was filtered with a Butterworth filter at 45 Hz to remove electrical noise. During testing for each flow rate, the two-phase flow was allowed to reach steady behavior (approximately 5 minutes) and the flow rate, pressure, and temperature measurements were time-averaged over a period of greater than 30 seconds, sufficiently long that the mean signal was not influenced by the fluctuations in the flow.

Three sides of the rectangular test section were made of clear acrylic to allow visual access, and the remaining side was an interchangeable silicon surface that could be designated as superhydrophobic or hydrophilic, as shown in Figure 2.3b. The interchangeable surface was held in place with a strip of double-sided tape that ran the length of the surface. The height of the channel was measured with a depth micrometer (accuracy of $\pm$ 0.01 mm) before and after pressure measurements were recorded. The acrylic channel was precision machined to be flat, and the channel was held together with two steel plates that ran the length of the channel in order to prevent any deflection caused by the rubber gasket seal. The two sides of the channel were held together with eight bolts, which were each tightened with a torque wrench to 17 N·m. The height of the channel varied from 360 to 380 μm, measured to an accuracy of $\pm$ 10 μm. For each test case, the measured height was used to calculate the Poiseuille number, Reynolds number, superficial velocities, and other variables. The width of the channel was 9.92 $\pm$ 0.01 mm . This corresponded to a range of hydraulic diameters of 690 to 730 μm and an aspect ratio (W/H) of approximately 27. For this high aspect ratio, the channel approached parallel plate conditions.

After assembling the channel for testing of each surface, the single-phase liquid flow pressure gradient was measured for a range of liquid-only flow rates corresponding to the two-phase flow rates to be tested. Subsequently, the two-phase pressure gradient measurements were conducted. Finally, the pressure gradient measurements for single-phase liquid flow were retaken to ensure the two-phase testing did not significantly influence the integrity of the test surface. After multiple sets of tests, the hydrophobic Teflon coating on the superhydrophobic surfaces began to wear off in certain locations on the surface and portions of the surface would irreversibly wet, impacting the single-phase pressure gradient. Thus for all superhydrophobic surfaces tested here, each surface was only tested once at each of the twelve flow rates measured. Repeatability was ensured by testing multiple surfaces under the same conditions. Importantly, the two-phase multiplier was calculated using the measured single-phase (liquid) pressure gradient in order to eliminate any differences in channel assembly from affecting the results.

The superhydrophobic surfaces were manufactured using standard photolithography and a deep reactive ion etch before coating with a thin layer of Teflon, as described in by Prince [87]. All of the superhydrophobic surfaces had a structure that consisted of parallel ribs 15–20 microns in height, as shown in Figure 2.4. Three different cavity fractions (ratio of the surface area between

the ribs to the total surface area) were tested: F_C = 0.5, 0.8, and 0.91. The cavity width was held constant at 32 microns. By maintaining a constant cavity width, the Laplace pressure was constant for all superhydrophobic surfaces tested. The implication of a constant Laplace pressure is that the propensity of surface wetting was the same regardless of cavity fraction. In the present study, the liquid flow rates were chosen such that the pressure in the channel was at or below the Laplace pressure (2.8 kPa) during single-phase flow, ensuring that the surfaces were in a Cassie, or non-wetting state during testing. Wetting of the structured surface was visually apparent in reflection from the surface due to the absence of the air layer between the water and surface. During single-phase testing, the surfaces were visually monitored to ensure wetting did not occur over the majority of the surface. During two-phase testing, alternating slugs caused local pressure spikes significantly larger than the Laplace pressure. However, the air present in the two-phase flow continually re-filled the cavities with air so that neither long term nor widespread wetting occurred on the surfaces. Breaker ridges, or ribs 8 microns wide were placed perpendicular to the ribs every 2.5 mm in order to locally contain any wetting that might occur during the two-phase tests. Static contact angles for the 0.5, 0.8, and 0.91 cavity fraction surfaces were 146, 157, and 155° in the longitudinal direction and 132, 149, 146° in the transverse direction, respectively. Contact angle measurements had a $\pm$ 2° accuracy. Control, or hydrophilic, surfaces were smooth silicon surfaces with no Teflon coating and a static contact angle of 60°.

2.4.1 Validation

In order to validate the channel setup, liquid single-phase pressure drop measurements were compared with predictive models in the literature. Differential pressure measurements for single-phase flow were taken in a classical hydrophilic channel and channels with one hydrophilic and one superhydrophobic surface. The Poiseuille number in a classical, hydrophilic, rectangular channel was predicted with a correlation developed by Shah and London [88],

$$f \cdot Re = 24(1 - 1.3553\eta + 1.9467\eta^2 - 1.7012\eta^3 + 0.9564\eta^4 - 0.2537\eta^5), \qquad (2.9)$$

where η is the aspect ratio of the channel, H/W. The pressure drop for parallel plate flow with one superhydrophobic surface was predicted using relations developed by Philip [80] and Enright *et*

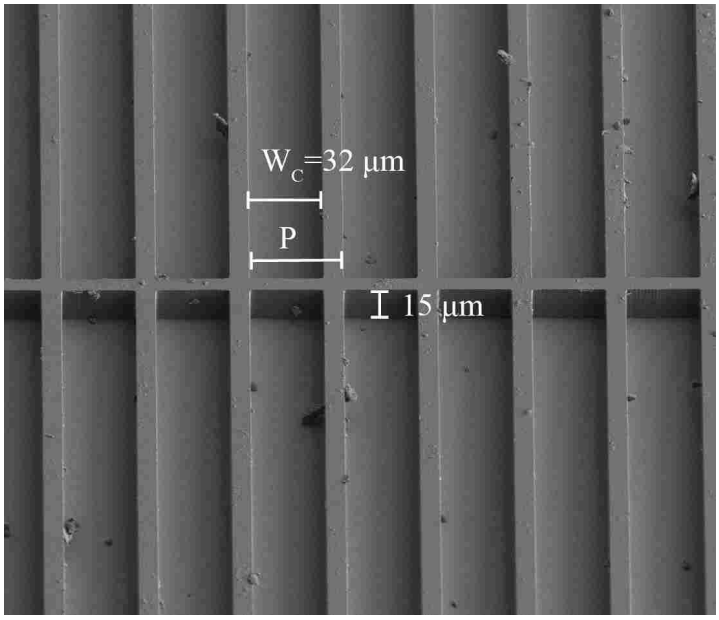

Figure 2.4: SEM image of a surface with cavity fraction $F_C = 0.80$. The perpendicular rib pictured is a breaker rib, which was placed every 2.5 mm in order to compartmentalize any wetting that occurred.

al. [84]. These relations are for parallel-plate flow with asymmetric slip at the wall. It was assumed that the percent reduction in Poiseuille number predicted for parallel plate flow with one superhydrophobic wall would be very similar to the percent reduction for a high aspect ratio rectangular channel with one superhydrophobic wall. Therefore, the predicted Poisieulle number for a rectangular channel with one wall superhydrophobic was calculated by applying the appropriate percent reduction to the value obtained using Equation 2.9. A 5.4, 10.6, and 14.7% reduction in Poiseuille number is predicted for surfaces with cavity fractions $F_C = 0.5$, 0.8, and 0.91, respectively. The predicted and average measured Poiseuille numbers for hydrophilic (HL) and superhydrophobic (SH) channels with single-phase flow are shown in Figure 2.5. The average percent error between the measured and predicted Poiseuille number was 2.2, 2.5, 4.2, and 2.6% for the hydrophilic, 0.5, 0.8, and 0.91 cavity fraction superhydrophobic surfaces respectively.

2.5 Results

Twelve different two-phase flow rates were tested, corresponding to liquid-only Reynolds numbers (Re_L) of 55–220 and gas-only Reynolds numbers (Re_G) of 22–215. The liquid- and gas-

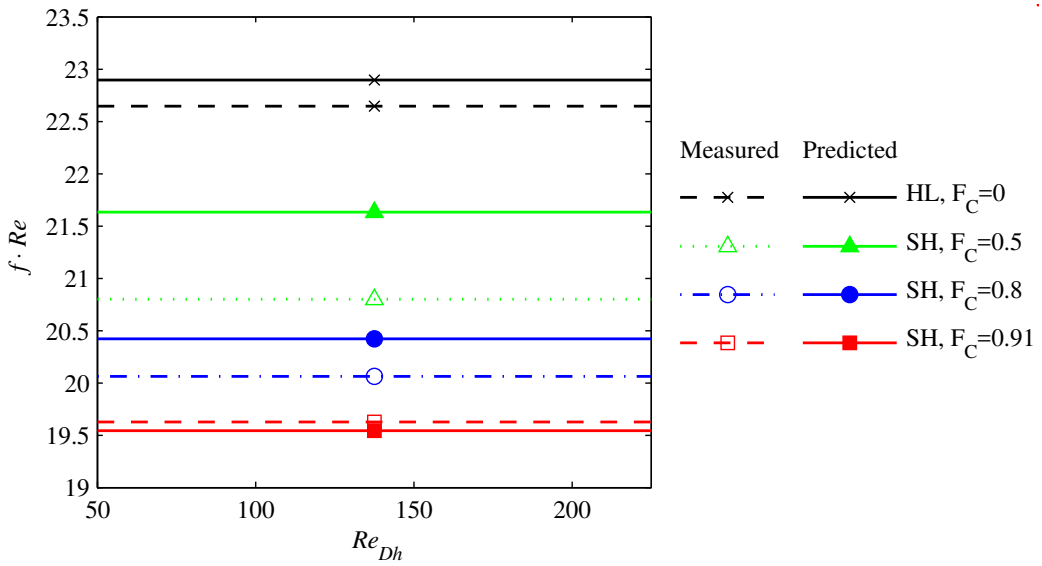

Figure 2.5: Poiseuille number using the Fanning friction factor for single-phase channel flow in channels for the hydrophilic and F_C = 0.5, 0.8, and 0.91 surfaces. The dashed lines indicate the average of the measured values. The solid lines/markers show the predicted Poiseuille number based on the percent reduction used by Philip [80] and Enright *et al.* [84] applied to Eqn. 2.9. The average percent error between the measured and predicted Poiseuille number was 2.2, 2.5, 4.2, and 2.6% for the hydrophilic, 0.5, 0.8, and 0.91 cavity fraction superhydrophobic surfaces respectively.

only Reynolds numbers refer to the Reynolds number that would occur if the liquid or gas portion of the flow were the only fluid in the channel,

$$Re_{(L,G)} = \frac{\rho_{(L,G)} j_{(L,G)} D_H}{\mu_{(L,G)}}, \tag{2.10}$$

where $j_{(L,G)}$ is the superficial liquid or gas velocity. The value of liquid- and gas-only Reynolds numbers are listed in Table 1 for each test scenario. Representative images of three test conditions are shown in Figure 2.6. The flow regime is slug for all flow rates tested, as described in Wambsganss *et al.* [89].

Four types of surfaces were tested, with multiples of each type for repeatability. Four hydrophilic surfaces were used as control surfaces; three F_C = 0.5, four F_C = 0.8, and three F_C = 0.91 superhydrophobic surfaces were also tested. The square root of the two-phase multiplier, (ϕ_M, see Equation 2.3) was calculated for each of the 14 surfaces. The single-phase pressure gradient in the equation was obtained using measurements taken directly before and after the two-phase

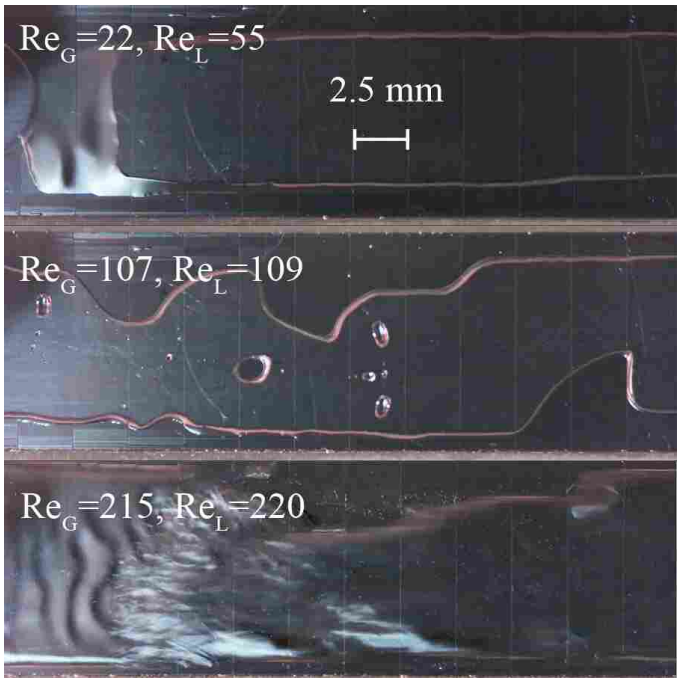

Figure 2.6: Top-down representative images of the flow across the cavity fraction F_C = 0.8 superhydrophobic surface at three different flow rates. Flow is from right to left. The fluid in the middle of the channels pictured in the top and center panels is air, with water positioned toward the edges. The channel in the bottom panel shows a liquid slug leaving the field of view; water is on the left, leaving the field of view, and air is entering on the right. The ambiguous transition from liquid to air is typical of the transition from liquid to air at higher flow rates.

flow tests. Results were averaged for each surface type; error bars on experimental measurements indicate the maximum and minimum of the values used for averaging.

The square root of the measured two-phase multiplier (ϕ_M) for all channels was compared with that predicted (ϕ_P) using a universal correlation for classical channels developed by Kim and Mudawar [70] as a percent difference, as shown in Figure 2.7. Agreement between the prediction and that measured for the control (hydrophilic) channels is better than 20%; this is excellent agreement given that the accuracy of the correlation is expected to be within $\pm$30%.

The channels containing a superhydrophobic surface showed an average reduction in ϕ of approximately 10% more than the hydrophilic control channels, regardless of the cavity fraction. This reduction of approximately 10% is observed in Figure 2.7 by comparing the deviation from the classical channel prediction (from Kim and Mudawar [70]) for a channel with a superhydrophobic boundary to a corresponding hydrophilic channel, at a given test condition. It should be noted that

Table 2.1: Liquid and gas only Reynolds number (Re_L, Re_G) and superficial velocities (j_L and j_G for each test condition.

test condition	Re_L	Re_G	j_L (m/s)	j_G (m/s)
1	55	22	0.07	0.48
2	55	107	0.07	2.34
3	55	215	0.07	4.7
4	109	22	0.15	0.48
5	109	107	0.15	2.34
6	109	215	0.15	4.7
7	163	22	0.22	0.48
8	163	107	0.22	2.34
9	163	215	0.22	4.7
10	220	22	0.29	0.48
11	220	107	0.29	2.34
12	220	215	0.29	4.7

ϕ_M is obtained by normalizing by the single-phase liquid pressure gradient. The single-phase liquid pressure gradient is approximately 5–15% lower for channels with a superhydrophobic surface than a corresponding hydrophilic channel, depending on the cavity fraction. Therefore the 10% reduction observed in Figure 2.7 for a channel with a superhydrophobic boundary is an additional reduction in pressure drop beyond the 5–15% reduction experienced for single-phase flow. Further, the effect of cavity fraction on the two-phase multiplier (as seen in Figure 2.7) appears to be small, and generally within the measurement uncertainty. However, averaged values of the two-phase multiplier seem to indicate that the two-phase multiplier may decrease slightly with increasing cavity fraction.

In order to compare the influence of flow rate on the two-phase multiplier, the ratio of the square root of the two-phase multipliers for a parallel-plate channel with one superhydrophobic wall and a channel with both hydrophilic walls is plotted in Figure 2.8, and defined as.

$$\frac{\phi_{SH}}{\phi_{HL}} = \frac{\sqrt{(\frac{dp}{dz})_{TP,SH}/(\frac{dp}{dz})_{L,SH}}}{\sqrt{(\frac{dp}{dz})_{TP,HL}/(\frac{dp}{dz})_{L,HL}}} \tag{2.11}$$

For two-phase flow in a channel with no reduction in pressure drop relative to a control channel with hydrophilic control surfaces, this ratio would be 1. The lower the value of the ratio, the greater

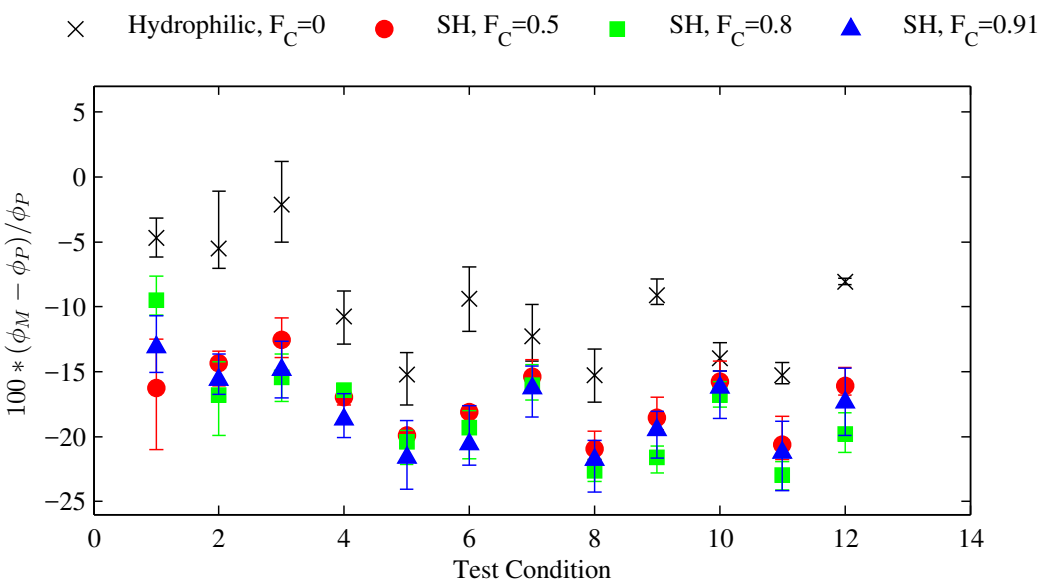

Figure 2.7: The square root of the two-phase multiplier obtained from the average measured value (ϕ_M) for each test condition in Table 1 compared with prediction by Kim and Mudawar [70] (ϕ_P). Test conditions correspond to Re_L of 55–220 and Re_G of 22–215. The three superhydrophobic surfaces have cavity fractions of 0.5, 0.8, and 0.91.

the reduction in pressure drop. Each data marker in Figure 2.8 represents the average ϕ_{SH} for all ten of the superhydrophobic surfaces divided by the average ϕ_{HL} for the four hydrophilic surfaces for the same test condition. The variation in ϕ for the different cavity fractions was significantly smaller than the difference between the hydrophilic and superhydrophobic surfaces; therefore the average of all the superhydrophobic surfaces, regardless of cavity fraction, is presented in Figure 2.8.

The reduction in pressure drop (smaller values of ϕ_{SH}/ϕ_{HL}) is more significant for increasing Re_G over the range of flow rates tested. As Re_G increases, the flow increasingly departs from a single-phase flow behavior and the influence of the slip condition becomes more pronounced, resulting in a larger drag reduction (lower values of ϕ_{SH}/ϕ_{HL}). With the exception of a Re_G = 22, the ratio is relatively constant with liquid-only Reynolds number, indicating that the percent drag reduction may not change appreciably with liquid flow rate in this flow regime. For Re_G = 22, the vapor quality is very low and approaches single-phase flow behavior with increasing liquid-only Reynolds number. As the quality approaches zero, the square root of the two-phase multiplier for

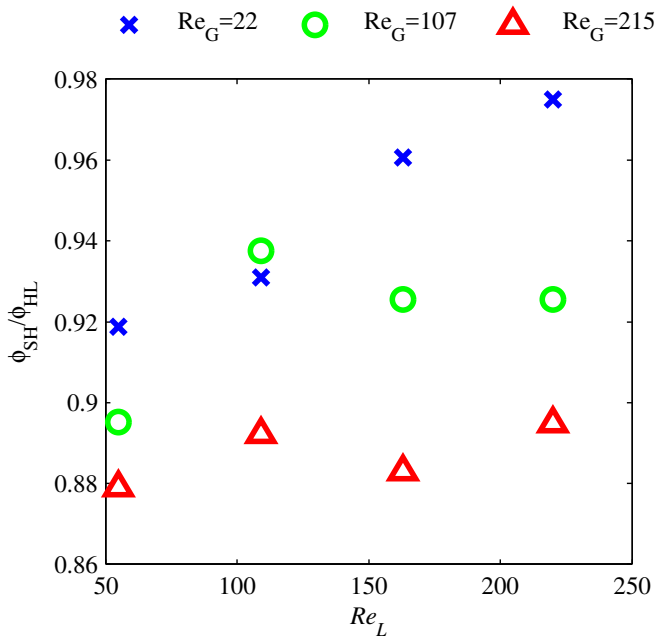

Figure 2.8: Ratio of the square root of the two-phase multiplier for a superhydrophobic surface and a classical surface as a function of Re_{L} and Re_{G}. The reduction in pressure drop appears to be more significant for increasing Re_{G}. Error bars representing the 95% confidence interval are shown in Figure 2.9.

both the superhydrophobic channel (ϕ_{SH}) and the hydrophilic control channel (ϕ_{HL}) approaches one, causing the ratio between them to also approach one.

In order to more closely examine the effect that increasing vapor quality has on drag reduction, the ratio $\phi_{\mathrm{SH}}/\phi_{\mathrm{HL}}$ is also shown as a function of vapor quality (x) in Figure 2.9. The maximum uncertainty associated with measuring the vapor quality is 0.0026. The ratio decreases with increasing vapor quality, for $x \lesssim 0.03$. For qualities $x \gtrsim 0.03$, the impact of quality on drag reduction appears to have a minimal effect for the gas and liquid flow rates considered here.

The results presented here are consistent with the approximately 40% drag reduction Wang *et al.* [79] observed for a channel with superhydrophobic walls. In contrast to the present study, all of the walls of their study were superhydrophobic. Furthermore, the range of flow rates in their study was at a much higher vapor fraction (0.2–0.4). While direct comparison cannot be made, the outcome that superhydophobic walls causes drag reduction is the same. The present study indicates that vapor fraction does impact the magnitude of the drag reduction. In addition, it is anticipated

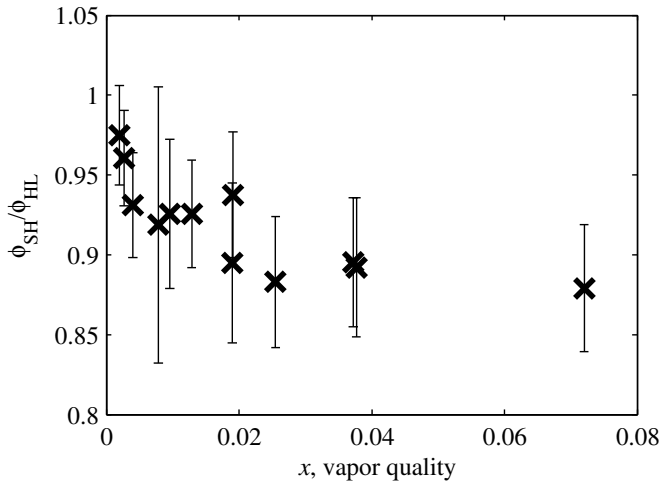

Figure 2.9: Ratio of the square root of the two-phase multiplier for a superhydrophobic surface and a classical surface as a function of vapor fraction. The reduction in pressure drop appears to increase with increasing vapor fraction. Error bars represent the 95% confidence interval.

that channel size would also impact drag reduction, with smaller sized channels leading to a greater percentage of drag reduction (relative to classical channels), as is true in single-phase flows.

2.6 Conclusion

The use of superhydrophobic surfaces in applications involving two-phase flow, including flow-boiling and -condensing, has the potential to be transformative across several industries. However, it is important to understand how the presence of superhydrophobic walls will impact the hydrodynamics of two-phase channel flow. The results of this study suggest that for a parallel plate channel (approximately 0.37 $\times$ 10 mm) with a single superhydrophobic wall, an average reduction of about 10% in the square root of the two-phase multiplier (ϕ) relative to a classical channel can be expected for superficial gas and liquid Reynolds numbers from 22–215 and 55–220, respectively. This corresponds to a reduction in drag of 10% in addition to that observed for single-phase liquid flow in a channel with a superhydrophobic boundary for the same conditions. The ratio of the reduction in drag for a superhydrophobic surface relative to a hydrophilic surface decreases with increasing vapor qualities, indicating that the effect of the superhydrophobicity is greater with increasing vapor fraction. Previous studies in channels with hydrophobic walls have found that a hydrophobic wall either slightly increases the drag or has no effect, dependent on the

flow regime and channel size. [72, 76–78] In contrast, from the present study and that of Wang *et al.* [79], it is clear that superhydrophobic walls have the potential to reduce drag in two-phase flows, again, depending on the channel size and flow regime. When conducting and reporting experiments involving two-phase flows in micro- and mini-channels, the wettability of the surfaces should be considered and reported.

CHAPTER 3. SUPERHYDROPHOBIC, CARBON-INFILTRATED CARBON NANOTUBES ON SI AND 316L STAINLESS STEEL WITH TUNABLE GEOMETRY

This chapter is published in Applied Physics Letters [90]. The format of this paper has been modified to meet the stylistic requirements of this dissertation.

3.1 Contribution Authors and Affiliations

Kimberly A. Stevens, Christian D. Esplin, Taylor M. Davis, D. Jacob Butterfield, Philip S. Ng, Anton E. Bowden, Brian D. Jensen, Brian D. Iverson

Department of Mechanical Engineering, Brigham Young University, Provo, Utah 84602

3.2 Abstract

Use of carbon nanotubes to create superhydrophobic coatings has been considered due to their ability to offer a relatively uniform nanostructure. However, carbon nanotubes (CNTs) may be considered delicate with a typical diameter of tens of nanometers for a multi-walled CNT; as-grown carbon nanotubes often require the addition of a thin-film hydrophobic coating to render them superhydrophobic. Furthermore, fine control over the diameter of the as-grown CNTs, or overall nanostructure is difficult. This work demonstrates the utility of using carbon infiltration to layer amorphous carbon on multi-walled nanotubes to improve structural integrity and achieve superhydrophobic behavior with tunable geometry. These carbon-infiltrated carbon nanotube (CICNT) surfaces exhibit an increased number of contact points between neighboring tubes, resulting in a composite structure with improved mechanical stability. Additionally, the native surface can be rendered superhydrophobic with a vacuum pyrolysis treatment, with contact angles as high as 160° and contact angle hysteresis less than 2–3°. CICNT diameter, static contact angle, sliding angle, and contact angle hysteresis were examined for varying levels of carbon-infiltration to determine the effect of infiltration on superhydrophobicity. The same superhydrophobic behavior

and tunable geometry was also observed with CICNTs grown directly on stainless steel without an additional catalyst layer. The ability to tune the geometry while maintaining superhydrophobic behavior offers significant potential in condensation heat transfer, anti-icing, microfluidics, anti-microbial surfaces and other bio-applications where control over the nanostructure is beneficial.

3.3 Introduction

Since their discovery, the unique properties of carbon nanotubes (CNTs) have made them a popular option for creating superhydrophobic surfaces. In particular, CNTs offer the ability to create a relatively uniform nanostructure, facile options for altering the surface chemistry (i.e. hydrophobic coatings or modification to the native surface chemistry), and flexibility in configuration (e.g. ability to grow directly onto a substrate, create patterns at the microscale, create two-tiered surfaces, etc.). Such properties have allowed superhydrophobic CNTs to be used in a range of applications such as enhanced droplet mobility during condensation [26, 43, 91–93], oil-water filtration [94, 95], absorption [96], self-cleaning, drag reduction [97], antifouling [98], lab-on-chip, creation of antimicrobial surfaces [99–101], and other bio-applications.

Carbon-infiltrated carbon nanotubes (CICNTs), also known as densified carbon nanotubes or carbon nanotube/carbon composite fibers [102–109], are comprised of CNTs with additional layers of carbon deposited on the nanotube framework. The resulting composite is stronger than CNTs alone [102, 103, 106–109] and can display higher electrical conductivity [109], depending on the level of infiltration.

Superhydrophobic surfaces are considered to have a solid/liquid contact angle greater than 145° and low contact angle hysteresis [13, 14]. Commonly, superhydrophobic surfaces are created through a combination of tailored surface roughness and surface chemistry. As described above, CNTs have been used to provide nanoscale surface roughness. Since as-grown CNTs are frequently not hydrophobic, CNT surfaces have been rendered superhydrophobic through the addition of a non-wetting coating using silanes, fluorination, or polymers like poly(tetrafluoroethylene) (PTFE) [26, 43, 91–93, 110–113].

However, post-growth surface treatments have also been shown to alter the wettability of carbon surfaces. Various plasma treatments have been used to render as-grown CNTs superhydrophobic [104, 114]. Li *et al.* demonstrated that the hydrophobicity of native CNTs could be

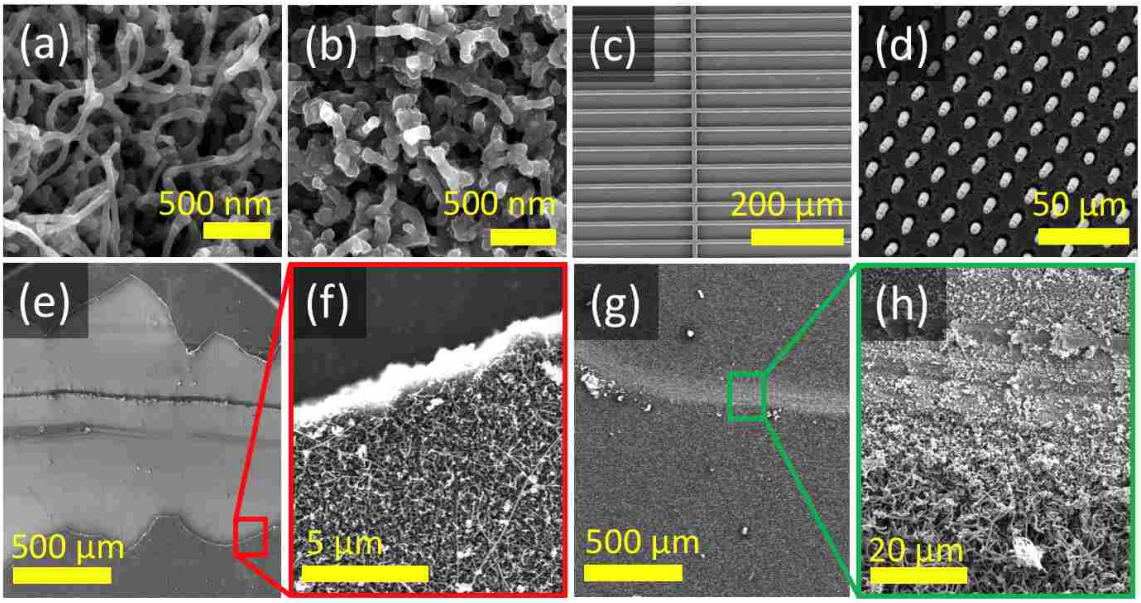

Figure 3.1: (a) Top-down view of vertically aligned CNT forest without infiltration. (b) Top-down view of a CICNT forest with reduced porosity and inter-CNT spacing. Microscale (c) rib and (d) post pattern comprised of CICNTs. (e-h) SEM images showing where a diamond scribe scratched CICNTs grown on (e,f) Si with an Fe catalyst and on (g,h) 316L stainless steel without a catalyst (direct growth). CICNTs remain attached to the stainless steel surfaces everywhere except where they came in direct contact with the diamond scribe.

controlled using reactive ion etching and laser pruning [115]. Others have demonstrated that CNT surfaces can be changed from a superhydrophobic state to a superhydrophilic state using UV and ozone treatment [116–119]. These groups have also shown that the process can be reversed to render non-infiltrated CNT surfaces superhydrophobic by heating CNTs in a vacuum (i.e. vacuum pyrolysis) [116–119]. This work demonstrates that CICNTs can also be rendered superhydrophobic using vacuum pyrolysis, eliminating the need for deposition of a non-wetting coating. We also quantify the surface wetting characteristics for patterned and unpatterned, two-tiered superhydrophobic CICNT surfaces. Further, we demonstrate that similar superhydrophobic CICNT surfaces can be grown directly on 316L stainless steel without the need for a catalyst. Finally, we explore the influence of the degree of carbon infiltration on CICNT diameter, static contact angle, sliding angle, and contact angle hysteresis.

3.4 Methods and Results

CICNT surfaces were grown in three different microscale patterns on alumina-coated silicon wafers. CNTs were grown to achieve: (1) a blanket forest of CNTs uniformly coating the surface (Figure 3.1a, b); (2) a microscale rib pattern (Figure 3.1c); and (3) an array of cylindrical posts (Figure 3.1d). Rib width and spacing in Figure 3.1c is 8 μm and 40 μm, respectively, resulting in 20% surface coverage by CICNT structures. Post diameter and pitch in Figure 3.1d is 7 μm and 16 μm, respectively, resulting in 15% surface coverage by CICNT structures in a square arrangement. Standard photolithographic and lift-off procedures were used to pattern a 7 nm layer of Fe as a catalyst for CNT growth. Diced, Fe-patterned samples were placed in a Lindberg/Blue M tube furnace for CNT growth by flowing H_2 gas (373.6 sccm) and C_2H_4 gas (204.0 sccm) at 750 °C for 15 s. After growth, the multi-walled CNTs achieved a height of approximately 20 μm. The CNTs were then coated (infiltrated) with amorphous carbon in the furnace by flowing H_2 (444.88 sccm) and C_2H_4 (204.0 sccm) at 900 °C for 0, 5, 10 or 15 min. Above 15 min, delamination of the porous carbon structure was observed from the Si substrate, likely due to internal stresses in the film. Infiltration times may vary for different furnace setups, but with similar decreasing porosity with increasing infiltration time.

CICNTs were also grown directly on the as-received 316L stainless steel substrates with a #8 mirror finish without an additional catalyst layer (hereafter referred to as direct growth), as opposed to indirect growth with CICNTs grown on stacked layers of Fe and alumina on Si. Samples were placed in a Lindberg/Blue M tube furnace and air annealed by ramping to 800 °C while flowing Ar gas, then held for 2 min while flowing air. CNT growth was achieved by flowing Ar (311.0 sccm) and C_2H_4 (338.0 sccm) at 800 °C for 20 min. The CNTs were then infiltrated with amorphous carbon in the furnace by flowing Ar (311.0 sccm) and C_2H_4 (338.0 sccm) at 900 °C for 10 min. The direct growth CICNTs were grown in a blanket forest with no microscale pattern.

Once the CICNTs were grown and infiltrated, the surfaces were vacuum annealed (i.e. vacuum pyrolysis) at approximately 17 kPa and 250 °C for 24 hours to remove the absorbed oxygen and achieve superhydrophobic behavior [118]. Prior to vacuum pyrolysis, the forest patterned surfaces displayed static contact angles of approximately 90°, as described by others [110, 113].

The diameter of the infiltrated nanotubes was measured from top-down imaging using scanning electron microscopy, similar to those shown in Figure 3.1a and b. Variation in diameter of the

coated nanotubes was observed and may be attributed to: (1) natural variation in size due to variations in the catalyst, (2) variation in diameter along the height of the nanotube, and (3) variable proximity of neighboring nanotubes. For this reason, a minimum of 20 measurements for diameter were averaged for characterization and the 95% confidence interval was reported.

Contact angle measurements were obtained using the sessile drop method [120, 121]. An approximately 2 mm diameter water drop was deposited on test surfaces, backlit with illumination from an LED light, and imaged with a high-resolution camera. A fifth-order polynomial fit was obtained for the droplet profile near the triple point contact line. The tangent line at the intersection of the polynomial fit and contact line was reported as the contact angle, with an accuracy of $\pm$ 2°. Contact angle from left and right sides were then averaged together. Advancing and receding contact angles were obtained by quasi-statically expanding and contracting the drop by adding and subtracting liquid volume with a needle while recording the drop with video [122, 123]. The advancing and receding contact angles were evaluated by post-processing video images in a similar manner to the static contact angle. MATLAB code used for obtaining the static, advancing, and receding contact angles can be found in Appendix A. The difference between the advancing and receding contact angle is the contact angle hysteresis. Sliding angle, or the angle at which a stationary, 2 mm diameter drop began to slide away from its original location, was measured using a micrometer angle gauge, accurate to within $\pm$ 0.5°.

The mean diameter of CICNTs for varying infiltration time is shown in Figure 3.2. For each infiltration time and pattern, measurements were taken at two locations on square samples: one near the center of the sample (location A) and the other near the corner (location B), as shown in the figure. As expected, more amorphous carbon was deposited during the longer infiltration times, leading to larger average diameters. The spatial location for diameter measurement of the CICNTs grown on Si had no significant effect on the average diameter. Samples that were infiltrated for 15 min had average nanotube diameters more than 400% larger than those with no infiltration for all surface patterns. The ability to tune the diameter of the structures by varying the infiltration time offers an additional element of surface feature control to CNT growth.

The microscale pattern influenced the rate of deposition of amorphous carbon and thus the average diameter of the structures. The forest pattern consistently exhibited the smallest diameters of the patterns tested for all infiltration times. CICNTs grown in the rib pattern generally had

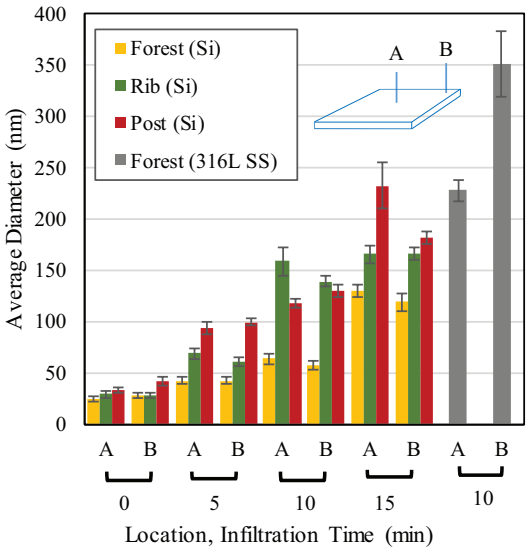

Figure 3.2: Average diameter of the CICNTs for different infiltration times. Each measurement is the average of at least 20 carbon nanotubes with error bars representing the 95% confidence interval. Measurements were taken at locations (A) near the center and (B) near the corner of square samples.

smaller diameters than those grown in the post pattern. This trend of increased infiltration may be due to the availability of more carbon atoms in the C_2H_4 gas or reduced obstruction of the gas for lower density microscale patterning. Jeong *et al.* observed a similar trend, where less-dense patterns grew taller CNT structures compared to their scaled, more-dense counterparts [124].

Diameters of CICNTs grown directly on stainless steel were significantly larger than the indirect growths; however, the size of the CICNTs as a function of infiltration time may not be directly compared between direct and indirect growth samples since the furnace conditions and substrates were different. The large variation in diameter size with spatial location reflects a general trend of large variation in diameter size for direct growth CICNTs.

Following vacuum pyrolysis treatment, all surfaces exhibited superhydrophobic behavior. The average static contact angle for each of the surfaces is shown in Figure 3.3, with values greater than 145°. The superhydrophobicity was stable, with insignificant changes in contact angle over time. Each measurement is the average of measurements taken at 3-4 different locations on the surface; the variation is represented by the error bars, which are one standard deviation above and below the average. The contact angle did not change significantly with CICNT diameter, microscale pattern type, or substrate. Though the average contact angle is slightly lower for the

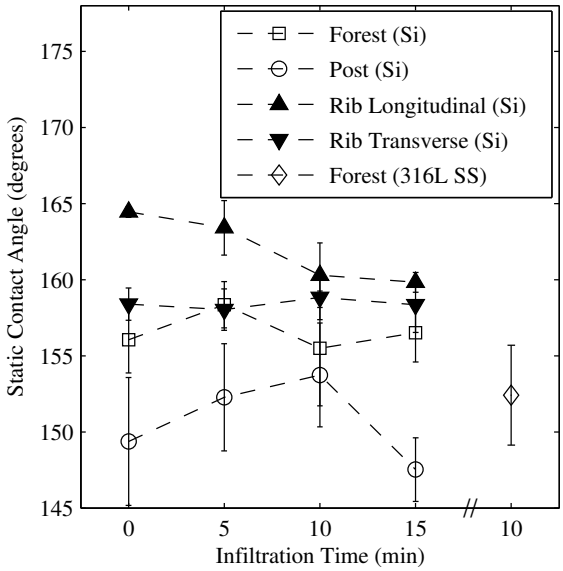

Figure 3.3: Static contact angle of water droplets on CICNT surfaces. Each measurement is the average contact angle taken at 3 or 4 different locations. The error bars are $\pm$ 1 standard deviation. Contact angle does not vary significantly with CICNT diameter, infiltration time, substrate, or microscale pattern.

surfaces with CNTs grown in a post pattern, the larger variation (reflected in the standard deviation) in static contact angle and larger contact angle hysteresis could be indicative of a larger number of defects on the surface. Indeed, the surfaces with CNTs grown in a post pattern were observably less robust than the other surfaces. Considering the extremely high aspect ratio of the carbon nanotubes (height approximately 20 μm, diameter 25-200 nm) it is not surprising that when the carbon nanotubes were grown in small islands they were not observed to be as strong since the network of interconnected CNTs was smaller. Regardless of infiltration time or microscale pattern, the average static contact angle for all surfaces resulted in superhydrophobic behavior.

In addition to having high static contact angles, each of the surfaces exhibited extremely low contact angle hysteresis, on the order of 1°. Each measurement in Table 1 is the average of hysteresis measurements taken at four different locations on the surface. Rib-patterned surfaces with four measurements included two measurements in each direction. All variation in contact angle hysteresis are within the measurement uncertainty, regardless of surface pattern or infiltration time. Sliding angle, another indicator of droplet mobility, was measured on surfaces of each pattern type and across a range of infiltration times. As expected from the low hysteresis, small sliding

angle values of less than 1-3° were observed, with no significant variation with infiltration time or pattern. All of the surfaces exhibited static contact angle and droplet mobility measurements that qualify them as superhydrophobic, and the degree of superhydrophobicity appeared to be largely independent of infiltration time or pattern over the range tested.

The foregoing results demonstrate that carbon infiltration can be used to tune the diameter of the carbon nanotubes, and that following a vacuum pyrolysis treatment, the carbon infiltrated carbon nanotubes are superhydrophobic, without the need for an additional hydrophobic coating. Even significant changes in the microscale arrangement, structure size, and substrate type (direct vs indirect) did not appear to influence the hydrophobicity of the resulting surface. CICNTs were also observed to be oleophilic; a drop of machine oil placed on the surface had a static contact angle of 35°.

The direct growth CICNTs on 316L stainless steel were observably more robust than the indirect growth surfaces on Si. To demonstrate their robustness, a diamond scribe was used to scratch a direct and indirect growth surface. SEM images of the scratches are shown in Figure 3.1e-h. On the indirect growth surface, a large section of the CICNT film delaminated and detached. However, on the direct growth surface, the scribe scratched the stainless steel surface, but CICNTs remain attached everywhere except where they came in direct contact with the diamond scribe. Direct growth CICNTs appeared to be less vertically aligned than the indirect growth sample on Si; the increase in random growth direction potentially resulted in an increase in the level of CNT interconnectedness, thus improving structural integrity.

3.5 Conclusions

The ability to tune nanoscale geometry without affecting hydrophobicity creates new possible applications for superhydrophobic CNTs. For example, superhydrophobic surfaces have shown great potential in the area of condensation heat transfer, where the droplet growth, coalescence, and departure is dependent on the nanostructure and feature sizes [29,43,44,91]. Mulroe *et al.* showed that the greater the nanoscale roughness (i.e. more tall, slender nanostructures as opposed to short, stout structures), the smaller the departure size of the drops, a parameter that is directly related to the rate of thermal transport [44]. The ability to tune the nanoscale geometry of superhydrophobic

surfaces used in condensation is a desirable trait with carbon infiltration affording the possibility to control CNT geometry.

Carbon nanotubes can be enhanced by infiltrating with amorphous carbon to improve mechanical durability [109], increase resistance to shear failure [102, 103, 106–109], and control nanoscale feature size. CICNT structures can be rendered superhydrophobic for a range of infiltration rates with negligible change in superhydrophobicity, as determined by the static contact angle, contact angle hysteresis, and sliding angle. In general, longer infiltration times result in carbon nanotubes with larger diameters, and the rate of infiltration is somewhat dependent on the patterning of carbon nanotubes, with sparser microscale patterning leading to higher rates of infiltration. Superhydrophobicity is invariant to infiltration rate/CICNT diameter within the range tested here. CICNTs grown directly on stainless steel surfaces, when subjected to vacuum pyrolysis, display the same superhydrophobic properties as those on Fe deposited on alumina. Surfaces created with direct growth of CICNTs on the stainless steel are even more robust than CICNTs grown on Fe deposited on alumina, as partially demonstrated by the scratch tests presented in this work. The ability to grow CICNTs directly on the stainless steel without the need for Fe deposition reduces fabrication complexity and increases potential scalability of these surfaces.

Table 3.1: Average of 2-4 hysteresis measurements on sample surfaces. The sliding angle was always less than 1-3 degrees regardless of surface geometry, infiltration time and location. Neither hysteresis nor sliding angle varies significantly with microscale pattern, CICNT diameter, infiltration time, or substrate.

Pattern	**Infiltration Time (min)**	**Hysteresis (degrees)**	**Sliding Angle (degrees)**
Forest (Si)	0	0.3	<1-3
	10	0.2	
	15	0.9	
Post (Si)	0	0.8	
	10	2.4	
Rib Longitudinal (Si)	0	<0.1	
	15	0.7	
Rib Transverse (Si)	0	0.5	
	15	1.8	
Forest (316L SS)	10	1.7	

CHAPTER 4. DROP-SIZE DISTRIBUTION DURING DROPWISE CONDENSATION FROM SIMULATION AND IMPLICATIONS FOR HEAT TRANSFER MODELING

4.1 Contributing Authors and Affiliations

Kimberly A. Stevens, Julie Crockett, Daniel Maynes, Brian D. Iverson

Department of Mechanical Engineering, Brigham Young University, Provo, Utah 84602

4.2 Abstract

Accurate models for condensation heat transfer are necessary to improve condenser design. Drop-size distribution is an important aspect of heat transfer modeling that is difficult to measure for small drop sizes. A number of theoretical models for the distribution function have been proposed, but not validated. The present work uses a numerical simulation of condensation to explore the influence of nucleation site distribution approach, nucleation site density, contact angle, maximum drop size, heat transfer modeling to individual drops, and minimum jumping size on the distribution function and overall heat transfer rate. The simulation incorporates the possibility of coalescence-induced jumping over a range of sizes. Results of the simulation are compared with previous theoretical models and the impact of the assumptions used in those models is explored. Assignment of the nucleation site spatial distribution and heat transfer model affect both the distribution function and predicted overall heat transfer rate. The influence of nucleation site density on drop-size distribution is similar to previously predicted trends. Results from the simulation suggest that when the contact angle is large, as on superhydrophobic surfaces, the heat transfer may not be as sensitive to the maximum drop-size as previously supposed. Furthermore, previous drop-size distribution models may under-predict the heat transfer rate at high contact angles.

4.3 Introduction

Condensation has application in a range of industries including water desalination and harvesting [63, 125, 126], energy conversion [1, 9, 127], electronics cooling [4], and environmental control [128]. Since it was discovered that heat transfer rates for dropwise condensation could be several times higher than film-wise condensation in the 1930s, much work has been done to model the heat transfer rate during dropwise condensation [6, 7]. The modeling approach typically consists of expressions for the heat transfer rate to an individual drop multiplied by the drop-size distribution. This product is then integrated over the range of drop sizes, as found on the condensing surface, to obtain the total heat transfer rate [7, 17, 56, 129].

$$q" = \int_{r_{\min}}^{r_{\max}} N(r) \cdot q_{\mathrm{d}}(r) \mathrm{dr} \tag{4.1}$$

Developing an accurate expression for the drop-size distribution is an integral part of modeling the overall heat transfer rate during condensation. One of the earliest and most adopted approaches to modeling the condensation heat transfer rate came from Le Fevre and Rose in 1966 [129, 130]. This work included both a semi-empirically derived expression for the drop-size distribution as well as a model for heat transfer to an individual drop. The drop-size distribution was of the form,

$$N(r) = \frac{1}{3\pi r^2 \hat{r}} \left(\frac{r}{\hat{r}}\right)^{-2/3}, \tag{4.2}$$

where $\hat{r}$ is the average maximum radius of the drops, or the average size to which drops grow before gravity-induced shedding. N is the drop-size distribution in drops/m^2/m. Other theoretical models agree well with the Le Fevre and Rose model [130–132]. The power-law expression in Le Fevre and Rose's model has been experimentally validated for distributions in the range $r > 5\times10^{-5}$ m, but drop-size distributions for smaller drop sizes have not been reported due to the difficulty of imaging these drops [7, 130, 133, 134]. Further, in reports that do include drop size measurements in the range 5×10^{-5} m $< r < 5\times10^{-4}$ m, the distribution function resolution is coarse.

In 1975 Tanaka observed, by means of population balance theory, that drop growth during condensation could be separated into two regimes: growth dominated by direct condensation and

growth dominated by coalescence with neighboring drops [132]. He observed that the distribution function for larger drops follows a power-law relationship, as predicted by Le Fevre and Rose [129, 130], but that the distribution function for smaller drops would be significantly different. In 2011, building on the work of Tanaka and others [135–137], Kim and Kim [56] used population balance modeling to develop a distribution function and heat transfer model for drops with contact angles greater than 90°. They showed that the distribution function was dependent on both the solid-liquid contact angle of the condensing drops and the nucleation site density on the surface. Miljkovic *et al.* [17] extended the work of Kim and Kim [56] to model drops on superhydrophobic surfaces. Superhydrophobic surfaces combine surface roughness with hydrophobic chemistry to achieve high solid-liquid contact angles ($>$145°) and high drop mobility (sliding angles $<$10°) [13, 14].

Condensing drops on superhydrophobic surfaces have been shown to adopt various wetting states, depending on the surface subcooling and properties (particularly the relationship between the nucleation site density and surface feature density) [29, 39]. Superhydrophobic surfaces can be designed such that surface adhesion forces are low enough that the energy released upon coalescence of condensing drops can propel the drops away from the surface [35, 41–43, 93]. When the surface is oriented vertically, coalescence-induced jumping can lead to permanent departure of the drops from the surface. The heat transfer model proposed by Miljkovic *et al.* [17] accounted for additional thermal resistance due to surface roughness, various possible wetting states of condensing drops, and the possibility for coalescence-induced jumping thereby providing a framework for modeling condensation heat transfer on superhydrophobic surfaces.

Previous models offer valuable insight regarding the distribution in the direct-condensation-dominated growth regime [17, 56, 132, 135–137], but the difficulty of obtaining experimental drop-size distribution information for smaller drops has precluded validation. Since smaller drops account for the majority of the heat transfer that occurs during condensation, it is essential to obtain accurate distribution functions in this range. Solution of the differential equation resulting from population balance modeling requires the assumption of an instantaneous, rather than gradual transition between direct-condensation-dominated growth and coalescence-dominated growth. Though small droplet growth may be dominated by direct condensation, coalescence can occur over a range of drop sizes and therefore can influence the distribution at smaller sizes than the in-

stantaneous transition point used by previous models. Another difficulty with population balance modeling occurs when coalescence-induced jumping is present. On realistic surfaces, jumping occurs for only a portion of the coalescence events that occur. However, when Miljkovic *et al.* [17] used population balance modeling to predict the distribution function on surfaces with jumping, of necessity they assumed all coalescence events result in jumping and that all coalescence events occur at a single size. In order to more accurately model condensation in the direct-condensation-dominated growth regime and validate earlier theoretical models, a computational simulation is proposed. The simulation incorporates coalescence for drops smaller than the transition between direct-condensation-dominated growth and coalescence-dominated growth regimes with coalescence events that may or may not result in departure based on user-specified criteria.

Other researchers have used computational modeling to gain insight into condensation behavior on superhydrophobic surfaces and to validate previously proposed theoretical models. Gose *et al.* [138] and Tanasawa and Tachibana [131] were among the first to attempt to use computer models, but due to limitations in computing power only investigated low distribution densities. Glicksman and Hunt [61] obtained distribution functions with a simulation that showed good agreement with the Le Fevre and Rose [129] distribution function at larger drop sizes and diverged at smaller sizes, based on the nucleation site density. However, their simulation was limited to drops with a contact angle of 90° and did not incorporate gravity-induced sweeping of drops. Mei *et al.* used a computer simulation to obtain the drop distribution also for a contact angle of 90°, but their results were intended for larger drop sizes where the distribution function was already well established [139]. Barati *et al.* used a numerical simulation of dropwise condensation to investigate condensation as a function of time for drops with a contact angle of 88°, though they did not report steady state drop distribution data [140]. Others have used numerical simulations to gain insight into various aspects of condensation and vapor deposition behavior but have not focused on the steady state distribution function and predicted overall heat transfer rate [64, 141–145].

The present work reports a computational approach to obtain the steady state drop-size distribution and associated time-averaged heat transfer rates for dropwise condensation over a range of contact angles from 90-180°, a larger range than previous simulations. It allows for coalescence at naturally occurring drop sizes in contrast to previous theoretical models, and it incorporates the departure of drops both by jumping and gravity-induced sweeping. The present work only con-

siders flat or nanostructured surfaces without a microscale feature size. The impact of maximum drop size, contact angle, nucleation site selection method, and coalescence-induced jumping on the distribution function and overall heat transfer rates is explored. The contribution of this work is two-fold. First, an approach for obtaining more detailed drop-size distributions than those considered previously is described and validated by comparison with other works. Second, results obtained using the approach described suggest that the simplifying assumptions used in previous models are more significant when the contact angle is large and coalescence-induced jumping occurs.

4.4 Methods

For the computer simulation, drops are distributed on a surface at nucleation sites, allowed to grow, coalesce, and depart either by sweeping or coalescence-induced jumping. At each time step, new drops are distributed. Expressions for time-averaged drop-size distribution and overall heat transfer rates are obtained from the results of the simulation. Simulations based on the modeling approach described for dropwise condensation on a vertical surface are performed in MATLAB as described in Figure 4.1. The following sections provide additional details about the modeling approach for each physical process.

4.4.1 Initial Nucleation

Prior to the start of the simulation, nucleation sites are randomly distributed across the surface with a specified nucleation site density (N_s). A drop with radius r_{min} is placed at each site. Unless otherwise noted, r_{min} is equivalent to the smallest thermodynamically viable drop, r_{thermo}, but for select cases described later in the text r_{min} can be larger than r_{thermo} [5].

$$r_{thermo} = \frac{2T_{sat}\sigma}{h_{fg}\rho\Delta T}. \tag{4.3}$$

4.4.2 Individual Droplet Growth

At each time step of the simulation, drops grow according to a specified model for the heat transfer rate to a single drop, q_d. The influence of using different models for the heat transfer

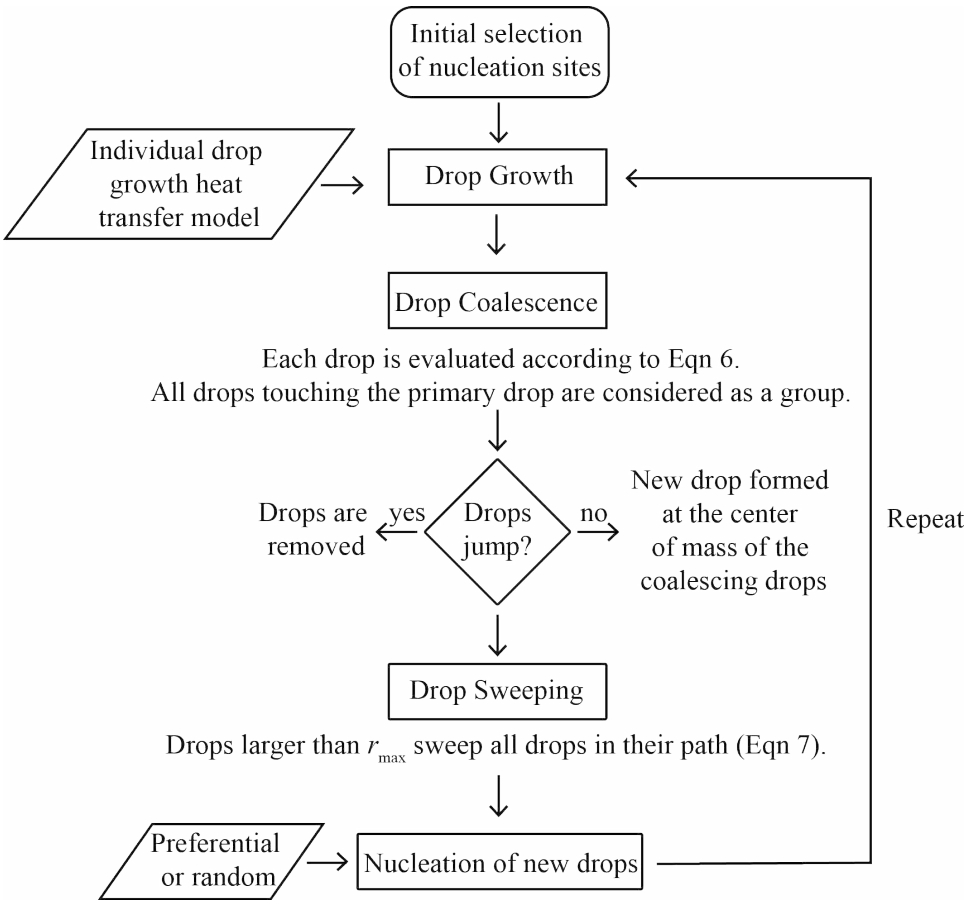

Figure 4.1: An overview of the steps in simulation of dropwise condensation on a vertical surface.

rate is compared in the present work. First, a thermal resistance model (implemented by Kim and Kim [56] and Miljkovic *et al.* [17]) is used for a flat or nanostructured surface where the microscale feature height may be approximated as zero. For the case of no jumping and with a microscale feature height of zero, the Kim and Kim [56] and Miljkovic *et al.* [17] expressions for heat transfer to a single drop are identical and will be referred to as the "thermal resistance model." Second, Chavan *et al.* [55] solved for the heat transfer rate to drops growing by condensation with a constant contact angle and found significant differences from the thermal resistance approach, which requires the assumption that the drop surface temperature be isothermal. They reported a piece-wise expression for the Nusselt number as a function of the Biot number and advancing contact angle for drops between 100 nm and 2 mm. Their model was will be referred to as the "Chavan model." Adhikari *et al.* recently proposed a finite element model covering a different range of Biot numbers than that covered by the Chavan model [146]. They provided tabulated data

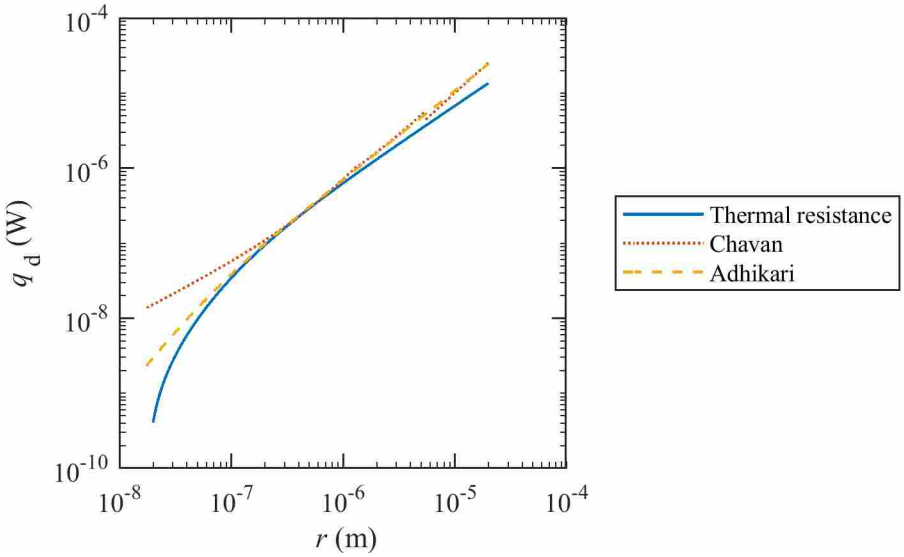

Figure 4.2: Comparison of models for the heat transfer rate to a single condensing drop, q_d, which are used in the simulation.

for the heat transfer rate to a single droplet as a function of Biot number and advancing contact angle. To avoid the computationally expensive task of referring to the tabulated data to calculate the heat transfer rate, a polynomial fit to the log of the heat transfer rate as a function of radius for a given contact angle was obtained. The difference between the tabulated data and the polynomial was always less than 2%. Their model will be referred to as the "Adhikari model." As seen in Figure 4.2, the Adhikari and Chavan models are similar everywhere except for small drop sizes. The heat transfer rate for the thermal resistance model approaches zero at the nucleation drop size and provides a lower prediction of the heat transfer rate at larger drop sizes relative to the computational models by Chavan and Adhikari.

For each heat transfer model, the amount of energy transferred to each drop over a given time step is approximated by multiplying the length of time step, δt, by the heat transfer rate to a single drop at the size corresponding to the previous time step. This transferred energy is then used to calculate the new volume of the drop,

$$V_{\text{new}} = V_{\text{old}} + \frac{q_d \delta t}{\rho h_{fg}}. \tag{4.4}$$

Assuming a spherical cap, the corresponding radius can then be calculated,

$$r_{\text{new}} = \left(\frac{3V_{\text{new}}}{\pi(2 - 3\cos\theta + \cos^3\theta)} \right)^{\frac{1}{3}}, \tag{4.5}$$

where θ is the solid-liquid contact angle. The spherical cap assumption is a good approximation for drops smaller than the capillary length, which is true for the largest drops considered in the present work (and all condensing drops that are not in a highly pinned state prior to flooding).

4.4.3 Drop Coalescence

The size and location of each drop is used to determine when drops on the surface touch in three-dimensional space. When the shortest distance (d) between a primary drop (p) and a neighboring drop (i) is less than zero, it is concluded that drops are touching according to the following relation,

$$d = \sqrt{(x_{\text{p}} - x_i)^2 + (y_{\text{p}} - y_i)^2 + (r_{\text{p}} - r_i)^2(\cos\theta)^2} - r_{\text{p}} - r_i, \tag{4.6}$$

where x, y, and r are the x and y locations and radii of each drop.

If the drops are touching, they either are replaced by a new drop located at the center of mass of the parent drops with the same total volume, representing coalescence, or are removed from the surface, representing coalescence-induced jumping resulting in departure from the surface. Three options for addressing a coalescence event can be selected in the simulation and are included to investigate the effects of coalescence-induced jumping. The three options that result from coalescence include drops that will (1) always depart, (2) never depart or (3) depart if at least two of the drops involved in the coalescence event are larger than a minimum threshold (specified by an input parameter to the simulation). Use of a minimum radius to determine whether coalescence results in jumping has physical rationale as researchers have observed that coalescence-induced jumping only occurs for drops larger than a minimum radius, and this radius is highly dependent on the surface structure [42–44, 147, 148]. For specially designed surfaces, drops as small as 500 nm have been shown to jump upon coalescence [42–44], but for more common superhydrophobic surfaces, such as copper oxide, the minimum radius for jumping is typically on

the order 10 μm. Recent research has shown that, in addition to minimum drop size, surface feature length scale, drop wetting state, relative size mismatch, and number of drops involved in a coalescence event all may influence whether or not a coalescence event will result in coalescence-induced jumping [42–44, 147, 148]. Though not considered here, these additional conditions could be incorporated into an energetic-based model for jumping.

It is possible for more than two drops to be overlapping at a given time. When checking for overlapping drops, the simulation iterates through each drop (primary drop) and determines which neighboring drops overlap with each primary drop. All neighboring secondary drops are included in the coalescence event and behave as specified by the selected approach for the resulting drop (remain/depart). It is also possible for secondary drops to be overlapping with other drops (tertiary drops). In this case, referred to as chain coalescence, all of the tertiary drops are also included in the coalescence event. Though it is possible for additional drops to be touching the tertiary drops, they are not included in the coalescence event since it is assumed that, when the time step is sufficiently small, their inclusion would have negligible impact on the distribution function and time-averaged heat transfer rate. It is also possible for a coalescence event to result in the creation of a new drop that is large enough to overlap with other drops, referred to as cascading coalescence. However, this possibility is not addressed until the next time step since waiting will not have a significant influence if the time step is sufficiently small. It is possible for both cascading and chain coalescence to occur within the same time step. However, as long as the time step is sufficiently small, the effect of waiting until the next time step to address the cascading part of the coalescence event is again assumed to be negligible. The assumption that coalescing drops will result in a drop at the center of mass of the parent drops has been validated experimentally [91, 149], and this approach has been used by Mei *et al.* [139], Barati *et al.* [140] and Khandekar and Muralidhar [145]. It includes the assumption that the coalescing drops have a similar morphology and adhesive force. For example, the center of mass assumption may not be true if one drop were highly pinned or in a wetted (Wenzel) state and the other drop in a non-wetting (Cassie) state.

4.4.4 Drop Sweeping

When a drop grows to a sufficiently large size ($r_{\max}$), the force of gravity will overcome the adhesive force and the drops will roll down along a vertical surface, sweeping and removing

all the drops in its path. For simplicity, the initial sweeping drop remains the same size throughout the sweeping event. However, in reality, as a drop travels downward from its center of mass, the sweeping behavior would increase the initial drop size as it coalesces with drops in its path. The influence of assuming a constant drop size during sweeping is expected to be negligibly small when the height of the domain is on the same order as the size of the sweeping drop, as is the case in the present work. An example of a sweeping event for drops with a contact angle of 165° is illustrated in Figure 4.3. The red and blue circles represent the projected area of all drops on the surface. The red circles indicate drops that interact and coalesce with a sweeping drop as it moves along the surface. The green circle outlines the base area in contact with the condensing surface of the initial sweeping drop. The contact path of the base area during the sweeping motion is demarcated with black dashed lines; clearly, all drops with bases overlapping the area traveled by the sweeping drop will be swept away. Additionally, drops located outside of the path may also interact with a sweeping drop, depending on size and location, as governed by the following equation for the minimum distance, d_s, between the sweeping drop, s, and another drop, i.

$$d_s = \sqrt{(x_s - x_i)^2 + (r_s - r_i)^2(\cos\theta)^2} - r_s - r_i \tag{4.7}$$

When the minimum distance below the half-height of the sweeping drop is negative, neighboring drops along the sweeping path will interact with the initial sweeping drop as it falls.

The maximum drop size, r_{max}, is specified for each simulation run. An expression to determine r_{max}, derived from a force balance between gravity and the adhesive force, has been used by other researchers to determine the maximum drop size [17, 56]. However, these expressions include both the advancing and receding contact angles, necessitating a specification of two variables rather than one. Additionally, it has recently been shown that the adhesive force can change depending on the degree of subcooling of the surface; this dependence has not yet been fully explored [42, 51, 58]. Therefore in this work, r_{max} remains as a specified input parameter so that the resulting distribution functions are independent of subcooling and surface properties other than the contact angle and r_{max}.

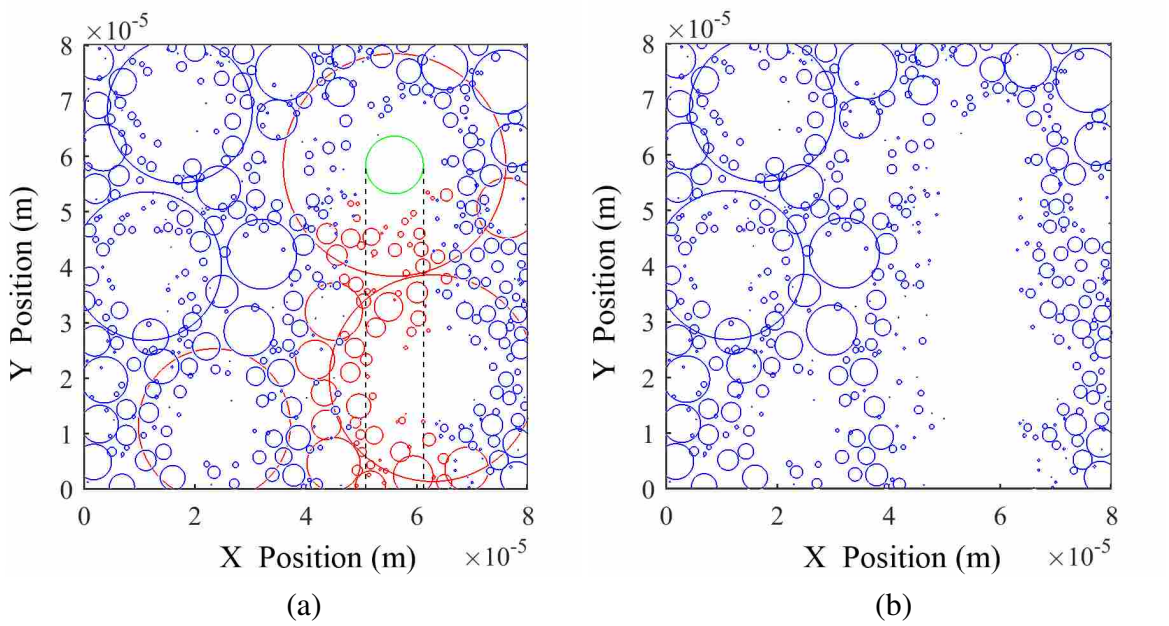

Figure 4.3: (a) Visualization of the drops in the simulation immediately prior to a sweeping event. Red and blue circles represent the projected area of all drops on the surface. As the large drop sweeps downward, it removes all the red drops with which it interacts in its path. The green circle outlines the base of the large sweeping drop. The area covered by the base of the sweeping droplet as it sweeps is demarcated with black dashed lines. (b) Visualization of the drops in the simulation immediately following a sweeping event.

4.4.5 Distribution of New Drops

At each time step, new drops are distributed either randomly or based on preferential nucleation sites coincident with the original nucleation locations. When drops are distributed randomly, the number of new drops is determined so the original nucleation site density, N_s, is maintained in the area of the surface not covered by drops, as follows:

$$n_{new} = \left(N_s - \frac{n}{A}\right)\left(A - A_b\right) \tag{4.8}$$

where A is the total area of the domain, A_b is the sum of the base area of all of the drops on the surface, n is the number of drops on the surface, and n_{new} is the number of new drops added in that time step. When new drops are distributed based on "preferential nucleation site" locations, the original nucleation sites from the first time step become the starting point of all future drops. When original nucleation sites are exposed, new drops begin to grow at these same locations. Preferential

nucleation sites can exist on real surfaces due to surface irregularities, nonhomogeneity in native surface chemistry, etc. Furthermore, evidence suggests that drops may leave behind a small amount of liquid from which subsequent drops may grow [30, 38, 52, 53, 91]. However, it is also possible for new nucleation sites to appear, particularly if all of the preferential sites are covered by drops. It is expected that realistic nucleation behavior is best described by a combination of these two approaches.

4.4.6 Steady State Condition

As the simulation progresses in time, drops continue to grow in size. Coalescence and sweeping events occur as outlined above with new drops distributed at each time step. Each simulation is run at least until the condensation has reached a quasi-steady state. As shown in Figure 4.4, the instantaneous heat transfer rate spikes following the departure of a drop, where the last complete sweeping cycle is highlighted in gray. Quasi-steady state is defined as the point where the time-averaged heat transfer rate (averaged from the start of the simulation to time t), $\overline{q''}_{0\to t}$, changes $<5\%$ relative to the final time-averaged heat transfer rate, $\overline{q''}_{0\to t_f}$, during the last sweeping cycle, as described in Equation 4.9 and shown in Figure 4.4.

$$\text{Percent Change} = 100 \times \frac{\overline{q''}_{0\to t} - \overline{q''}_{0\to t_f}}{\overline{q''}_{0\to t_f}} \tag{4.9}$$

For the case shown, the requirement of $<5\%$ change is met after the first complete sweeping cycle, around 1 second. Typically, simulations are run much longer than that required by $<5\%$ change over the course of the last sweeping cycle resulting in many sweeping cycles and $<1\%$ change in the time-averaged heat transfer rate. When θ is low and R_{max} is large, the instantaneous heat transfer rate changes more dramatically with each sweeping event. However, large R_{max} requires large domain sizes, and require long computational time; therefore, large simulations were run for the minimum amount of time required to meet the requirement for $<5\%$ change over the course of the last sweeping cycle.

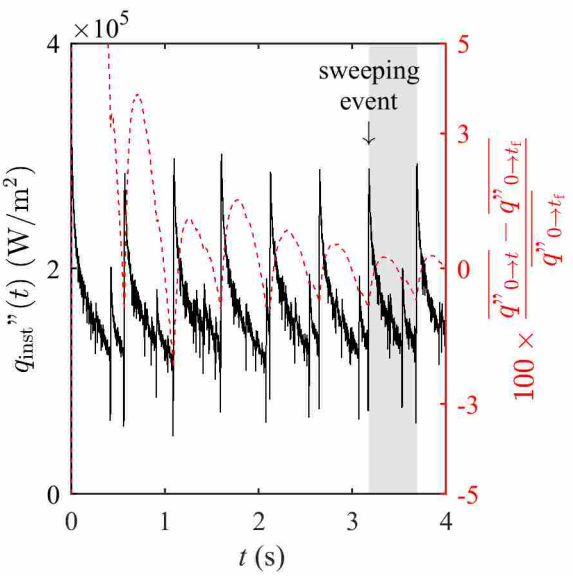

Figure 4.4: Instantaneous heat transfer rate for a simulation with a contact angle of 90° and r_{max} = 1×10^{-4} m. Large spikes occur immediately following a sweeping event. The area shaded in gray indicates the last complete sweeping cycle. The simulation is considered to have reached steady state when the time-averaged heat transfer rate (as shown on the right ordinate) changes by less than 5% over the course of the last sweeping cycle (typically $<1\%$).

4.4.7 Distribution Function

The purpose of the simulation is to obtain the steady state distribution for the size of the drops on a surface during condensation, $N(r)$, or the number of drops per unit area as a function of radius size. The time-averaged drop-size distribution is calculated in following manner. A histogram of drop sizes is generated from all of the drops in the simulation and averaged over many specific instances in time so that a minimum of 1×10^7 drops is used to construct each histogram. The histogram bin width is determined in a piece-wise manner. The bin width for smaller drops is defined by the amount that a drop grows in a single time step. For larger drops where the drop size changes by less than 1% in a single time step, the bin width is specified as 25 logarithmically spaced bins. The count is then normalized by the domain size, and the distribution is obtained by dividing the histogram by the bin width, so that the distribution function has units of drops$/$m$^2/$m, or drops$/$m^3. The distribution function is always shown with error bounds associated with bin width using light shading, and is often approximately the size of the line (e.g. Figure 4.5).

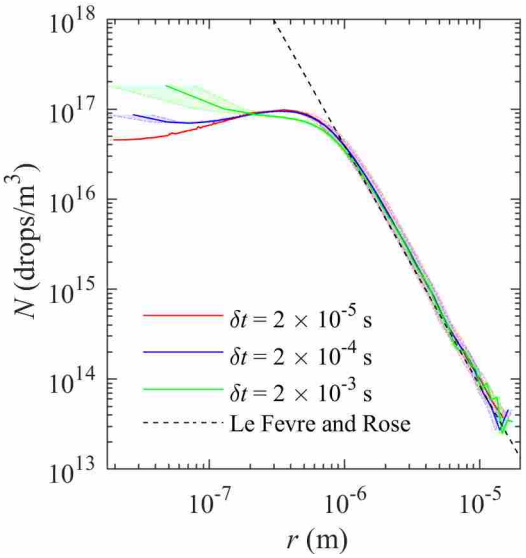

Figure 4.5: Distribution functions obtained from simulations run with time steps of varying size. In large drop range, the distribution functions converge, indicating that the simulation is time grid independent for that size. Distribution functions diverge with decreasing radii, where the distribution function is no longer time grid independent.

4.4.8 Time Grid Independence

Selection of the time step has important implications for the accuracy of the simulation, where smaller time steps produce more accurate results at the cost of increased computation time. Selection of the time step depends on the heat transfer rate to a single drop, which directly governs the rate of drop growth and is dependent on the degree of subcooling, contact angle, ambient pressure, etc. Therefore, each simulation was run at multiple time steps to establish time grid independence. The distribution function $N(r)$ is shown in Figure 4.5 for simulations run with decreasing time step. The distribution functions converge at larger radii and diverge at smaller radii, as shown for the selected time steps. The distribution is considered grid independent until divergence in the distribution functions with decreasing radius. In order to establish the time-averaged heat flux, q", at least three simulations of decreasing time step were run for each condition tested, and the grid-convergence index was calculated following the method described by Roache [150], using the generalized Richardson extrapolation. Uncertainty limits are reported with error bars for each time-averaged heat flux, though in some cases the error bars are too small to distinguish in the figures.

4.4.9 Domain Size Selection

The simulation consists of a square domain with side length L. The number of drops in the simulation and the corresponding computational time increases with the square of the domain area. Therefore it is desirable to limit the domain size as much as possible without sacrificing accuracy. The domain size was chosen so that $2r_{\max}/L < 0.8$, ensuring that the largest drop never covered the entire domain. Satisfying this criteria produced both distribution functions and time-averaged heat transfer rates that were largely independent of domain size (no discernible difference in distribution function and difference in heat transfer rates smaller than the time-grid convergence uncertainty), though smaller domain sizes (relative to the maximum drop size) were not tested and may also produce domain-size independent results.

4.4.10 Constant Contact Angle

Drop growth with constant contact angle is assumed in the simulation. Although it is well known that the contact angle changes as drops grow [17, 29, 38, 39, 151–154], for a smooth hydrophobic or nanostructured superhydrophobic surface the size range where drops are growing with a non-constant contact angle is relatively small in comparison to the total drop-size range [17, 29, 153]. At any given time, drops that would be growing with a non-constant contact angle account for a small fraction of the total area covered on the surface and therefore contribute only a small amount towards the total heat transfer. In order to ensure that using a constant contact angle would not significantly influence the accuracy of the results, simulations were conducted where the contact angle varied as proposed by Miljkovic *et al.* [17] for a partially-wetting drop on a surface with features of length scale 100 nm, intrinsic contact angle $\theta_a = 90°$, apparent contact angle when in the Cassie-Baxter state $\theta_a^{CB} = 165°$, and $r_{\max} = 2\times10^{-5}$ m. Selecting a small $r_{\max}$ results in a contact angle change over a larger percentage of the range of drops on the surface, making this test scenario an extreme example. The Chavan heat transfer model is used since the Adhikari model requires a separate curve fit for each contact angle. Nucleation sites were selected randomly, drops did not experience jumping, and the initial nucleation site density was $N_s = 1\times10^{11}$ drops/m^2. The radius where the contact angle becomes constant, r_{CCA}, is 3.86×10^{-7} m. In this extreme case, varying the contact angle resulted in $<$2.6% difference in the time-averaged heat transfer

rate. Given that drops smaller than r_{CCA} accounted for $<1\%$ of the surface area covered by drops, this is not a surprising result, and strengthens the argument that using a constant contact angle does not significantly influence the accuracy of the results. Furthermore, by maintaining a constant contact angle, the distribution functions obtained from the simulation are applicable for all smooth hydrophobic and nanostructured surfaces and are not tied to specific surface properties. Since r_{max} is specified in the simulation, the receding and static contact angles are never specified, and a single contact angle, θ (which may be thought of as the advancing contact angle) is used throughout the simulation.

Contact angle varies more appreciably on microstructured surfaces where inclusion of a non-constant contact angle may have a more significant impact on the distribution function and heat transfer rate. The impact of varying contact angle should be explored before using the constant contact angle assumption with microstructured surfaces [17, 29, 153].

4.4.11 Parameter Space and Operating Conditions

The present work explores the influence of heat transfer model (thermal resistance, Chavan, Adhikari), nucleation scheme (random or preferential), maximum drop size (r_{max}), contact angle (θ), initial nucleation site density (N_s), and jumping on the distribution function, N, and spatially and time-averaged heat transfer rate, q". These parameters (heat transfer model, nucleation scheme, maximum drop size, contact angle, initial nucleation density, and presence of jumping) are specified as input conditions for the simulation. In practice, maximum drop size, contact angle, initial nucleation density, and minimum jumping size depend on the condensing substrate physiochemical properties, surface texturing, and surface subcooling, and could be measured for a given surface and set of operating conditions [61, 145, 155]. All results presented are based on a saturation temperature, T_{sat} = 22 °C and $\Delta T = T_{sat}$ - T_s = 1 °C. Unless otherwise indicated, the simulations were run assuming $N_s = 1\times10^{11}$ drops/m^2, utilization of the Adhikari heat transfer model, no drop jumping, and a random nucleation scheme. The maximum drop size ranged from 2×10^{-5} m to 2×10^{-4} m and the contact angle varied from 90 to 165°.

4.5 Results

4.5.1 Model Validation and Comparison

The models proposed by Kim and Kim [56] and Miljkovic *et al.* [17] both divide the distribution function into two drop growth regimes: (1) growth mainly by direct condensation, and (2) growth primarily by coalescence. In these models, the region where drop growth is dominated by coalescence is modeled using the power law relation proposed by Le Fevre and Rose [129, 130] in Equation 4.2. Both works use population balance modeling to approximate the distribution function in the direct-condensation-dominated growth regime and solve the resulting differential equation with two boundary conditions at the transition between the two regimes (i.e. at the equilibrium radius, r). The first boundary condition stipulates that the distribution functions for the two regimes have the same value at r_e. The second boundary condition stipulates that the derivative of the natural log of the distribution functions also be equal,

$$\frac{\mathrm{d}}{\mathrm{d}(\ln r)}\ln n(r) = \frac{\mathrm{d}}{\mathrm{d}(\ln r)}\ln N(r) = -\frac{8}{3}, \tag{4.10}$$

where $n(r)$ and $N(r)$ are the distribution functions in the direct-condensation- and coalescence-dominated growth regimes. In the case where the feature height can be considered negligible and no jumping occurs, the only difference in the distribution functions proposed by Kim and Kim [56] and Miljkovic *et al.* [17] is the value of the equilibrium radius. Kim and Kim [56] calculate r_e as half of the average distance between drops, assuming the drops are arranged in a square lattice, or $r_e = 1/(2\sqrt{N_s})$. Miljkovic *et al.* [17] use half of the average distance between drops if the drops are distributed following a Poisson distribution, or $r_e = 1/(4\sqrt{N_s})$. A Poisson distribution has been shown to accurately reflect the distribution of drops during condensation on surfaces of nominally uniform wettability [29, 39, 154]. The separation of the distribution function into two separate regimes facilitates the use of population balance modeling and allows solution of the accompanying differential equation. However, in reality the onset of coalescence is not expected to occur at a single size; drops grow by direct condensation throughout their lifetime, and coalescence does not suddenly occur at a single size. If one were to plot a histogram of drop sizes at coalescence on a surface with nucleation sites following a Poisson distribution, coalescence would

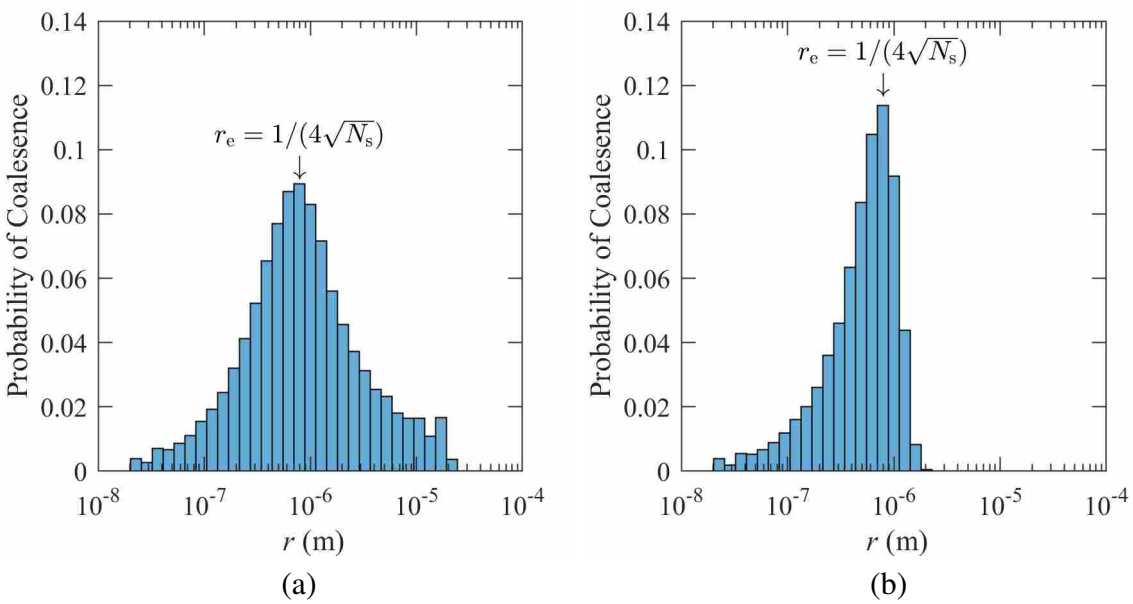

Figure 4.6: Probability coalescence will occur at a certain size where nucleation sites are distributed following a Poisson distribution, the Adhikari individual drop heat transfer model is used, θ = 165°, (a) assuming coalescence does not result in departure, and (b) coalescence always results in departure. The most common size for drop coalescence to occur is $r = 1/(4\sqrt{N_s})$, but coalescence occurs over a wide range of drop sizes. When drops remain on the surface following coalescence they continue to coalesce until r_{max}. However, when coalescence results in departure, drops do not grow large enough to reach r_{max}, and the coalescence-size distribution drops off sharply.

most frequently occur at $r = 1/(4\sqrt{N_s})$, but coalescence would occur over a range of drop sizes, as observed during condensation and illustrated in Figure 4.6.

In order to compare the results of the current simulation with the distribution functions proposed by Kim and Kim [56] and Miljkovic *et al.* [17], coalescence was suppressed until $r = r_e$. In this comparison case the thermal resistance heat transfer model was used, θ = 165°, r_{max} = 2×10^{-5} m, and $N_s = 1\times10^{11}$. Unsurprisingly, suppressing coalescence results in a function that has a discontinuous first derivative at $r = r_e$, as shown in blue in Figure 4.7a. At $r > r_e$, the simulation distribution matches the distribution predicted by Le Fevre and Rose [129, 130] and Miljkovic *et al.* [35], and satisfies the first boundary condition used to solve the population balance modeling differential equation. However, for $r < r_e$ the distribution is significantly lower than that predicted by Miljkovic *et al.* [17]. The models do not have a discontinuous slope at $r > r_e$ since the second boundary condition forces the slope at $r = r_e$ to match that of the Le Fevre and Rose [129]

distribution. If coalescence is not suppressed, but allowed to occur naturally (red distribution in Figure 4.7a), the distribution converges with the Le Fevre and Rose distribution for coalescence-dominated growth, and both boundary conditions are satisfied, as shown in Figure 4.7. The shape of the distribution function when coalescence is not suppressed is similar to those proposed by Kim and Kim [56] and Miljkovic *et al.* [35]. However, rather than converging at $r = 1/(4\sqrt{N_s})$ or $r = 1/(2\sqrt{N_s})$, in this particular test case the radius of convergence is observed to be somewhere in between, at approximately $r = 1\times10^{-6}$ m. The distribution function converges at a larger radius since coalescence occurs for drops with $r < 1/(4\sqrt{N_s})$. Coalescence of the drops causes the distribution function to decrease, thereby converging with the power-law function at a larger radius. The similarity in shape between the distribution from simulation and the previous models provides confidence in the current approach. The difference in the radii of convergence with the Le Fevre and Rose distribution function arises from allowing coalescence to occur naturally, rather than at a single radii as modeled in population balance theory. Results from the simulation suggest that the distribution function in the direct-condensation-dominated regime converges with the power-law function at a larger radius than $1/(4\sqrt{N_s})$, even though $r = 1/(4\sqrt{N_s})$ is the most common size for coalescence.

Miljkovic *et al.* [17] also modeled the distribution function for drops that depart via coalescence-induced jumping and assumed that drops would coalescence and depart when $r = r_e = 1/(4\sqrt{N_s})$, as shown in Figure 4.7b. For comparison, a distribution from simulation is shown where coalescence is suppressed and all drops are removed from the simulation at $r = 1/(4\sqrt{N_s})$. Agreement between the distribution proposed by Miljkovic *et al.* [17] and the simulated distribution is good (less than 8% difference in predicted heat transfer rate), providing confidence in the results from simulation. The distribution function is also shown for the case where coalescence is allowed to occur naturally and all drops depart upon coalescence. Drop coalescence causes a decrease in the distribution function relative to the case where coalescence is suppressed, and the distribution curve drops off gradually, rather than terminating immediately. The comparison of the two different distribution functions highlights the influence of suppressing coalescence on the distribution function.

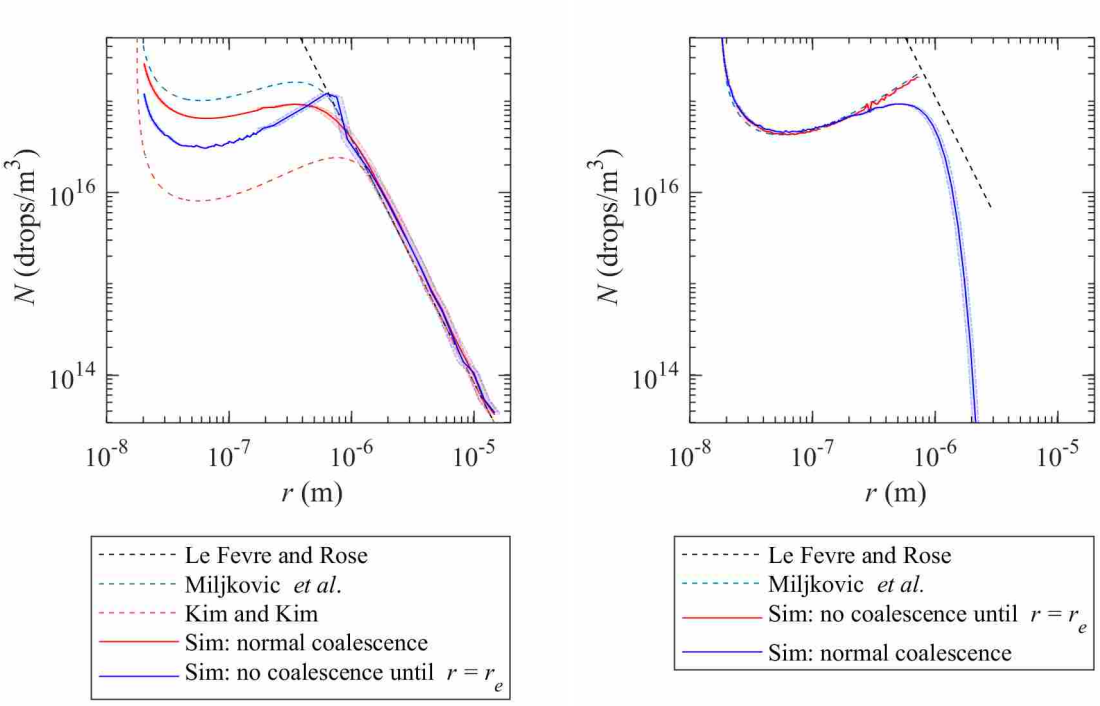

(a) (b)

Figure 4.7: (a) Comparison of the distribution functions obtained from simulation (red) with those proposed by Kim and Kim [56], Miljkovic *et al.* [17], and Le Fevre and Rose [129, 130]. When coalescence is not suppressed the distribution (red) converges with the Le Fevre and Rose distribution at a size larger than that proposed by Miljkovic *et al.* and smaller than that proposed by Kim and Kim. When coalescence is suppressed until $r = 1/(4\sqrt{N_s})$ the simulated distribution (blue) matches the distribution proposed by Miljkovic *et al.* at $r = r_e$, but the slope of the distribution function is discontinuous. (b) Drop-size distribution functions for which all coalescing drops either jump (red) or for which coalescence is suppressed and all drops depart at $r = 1/(4\sqrt{N_s})$ (blue). The non-coalescing case agrees well with the distribution proposed by Miljkovic *et al.* for suspended drops with $r_{max} = 1/(4\sqrt{N_s})$ (dashed blue). The difference between the simulated distributions demonstrates the influence of assuming coalescence occurs at a single drop size. The Le Fevre and Rose distribution for $r_{max} = 1/(4\sqrt{N_s})$ is also shown (dashed black). All other distributions shown in (a) and (b) correspond to the case where $\theta = 165°$, $r_{max} = 2\times10^{-5}$ m, and $N_s = 1\times10^{11}$.

4.5.2 Influence of Heat Transfer Model

The model selected for heat transfer to each individual drop influences the resulting distribution function. Distribution functions for three heat transfer models are compared in Figure 4.8a with that predicted by Le Fevre and Rose [129, 130]. The shape of the distribution function is similar for all three models, though there are significant differences observed as their behavior

departs from the power-law function. In the thermal resistance model for $r = r_{\text{thermo}}$, the heat transfer rate is zero and drops will never grow. Therefore, r_{min} is chosen to be larger than r_{thermo}. To demonstrate the influence of increasing r_{min}, the distribution function for two different r_{min} values are shown: $r_{\text{min}} \approx r_{\text{thermo}}$ (r_{min} is $1\times10^{-13}\%$ larger than r_{thermo}) and $r_{\text{min}} = 1.15 \cdot r_{\text{thermo}}$. The first r_{min} was selected based on the numerical accuracy of the simulation. The second r_{min} was chosen at a point where the distribution function was no longer changing significantly with r_{min}. The distribution produced with the second r_{min} is likely more accurate since it agrees better with distributions produced using the Chavan and Adhikari models which do not assume an isothermal surface. The Adhikari model was developed from simulations using Biot numbers in the range $0.0001 < \text{Bi} < 1000$, while the Chavan model was developed from simulations covering a larger range, $0.1 < \text{Bi} < 1 \times 10^5$. In the range of Biot numbers where the simulations overlap, the agreement between the simulations is good; however for smaller drop sizes, the heat transfer rate (Figure 4.2) and distribution functions (Figure 4.8a), diverge. The range of Biot numbers in the present work is $0.0064 < \text{Bi} < 284$. Therefore, it is assumed the Adhikari model is more appropriate. The time-averaged heat transfer rate for the Chavan and Adhikari models is presented in Figure 4.8b. The heat transfer model makes a larger difference on the overall heat transfer rate when the contact angle is low, but the difference is considerably smaller for large contact angles.

The difference in the distribution function and heat transfer rate between the various models highlights the fact that the accuracy of the distribution function is dependent on the accuracy of the model for heat transfer to a single drop. Recently Xu *et al.* proposed a detailed model which includes two dimensional conduction, convection in the drop, moving contact line, mass transfer into the droplet, and interface expansion [156]. The authors did not provide an expression for the heat transfer rate to an individual drop, which precludes its application in the present work, but did suggest that current models which only consider conduction within the drop severely underestimate the heat transfer rate in larger drops. If the output of their model were to be combined with a more detailed distribution function, presumably a more accurate model for the overall heat transfer rate during condensation could be obtained.

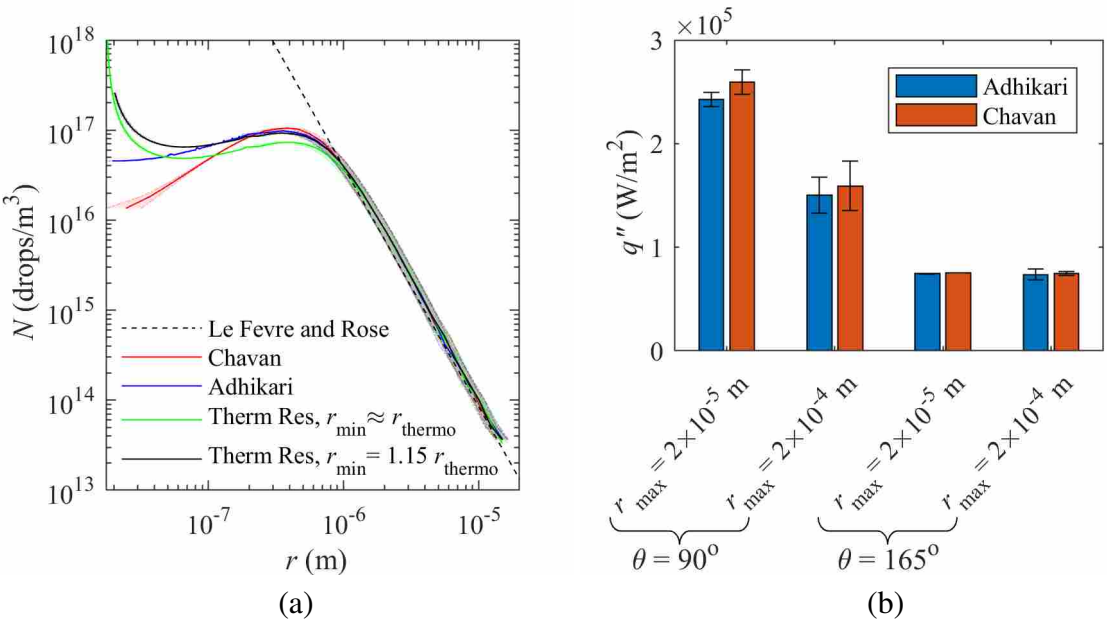

Figure 4.8: (a) Drop distribution functions obtained using three different models for heat transfer to a single drop. Two different r_{min} are used for the thermal resistance model. In the case labeled $r_{\text{min}} \approx r_{\text{thermo}}$, r_{min} is 1×10^{-13}% larger than r_{thermo}. The contact angle for the distributions shown was 165° with $r_{\text{max}} = 2\times10^{-5}$ m. The heat transfer model has a significant influence on the distribution functions at small radii. (b) Time-averaged rates of heat transfer for the two models derived from numerical simulations. The influence of heat transfer model on the overall heat transfer rate becomes less significant when the contact angle is large.

4.5.3 Influence of Nucleation Scheme

The influence of selecting randomly distributed or preferential nucleation sites to distribute new drops on a condensing surface can be seen in Figure 4.9. It is supposed that the random and preferential nucleation site approaches represent extremes which bracket realistic condensation behavior. For low contact angles, the distribution is consistently lower when the drops are distributed at preferential nucleation sites, as opposed to random sites. When the contact angle is low, drops have a large base area; drops that coalesce and remain on the surface cover the "preferential" nucleation sites, and the average drop density is much lower than N_s (average drop density of 3×10^{10} drops/m^2 for the case shown in Figure 4.9a). When the distribution is random, the number of new drops is governed by the exposed area not covered by drops, and the average drop density on the surface is much higher than in the preferential case, though still lower than N_s (average drop density of 9.5×10^{10} drops/m^2 for the case shown in Figure 4.9a). In contrast, when the

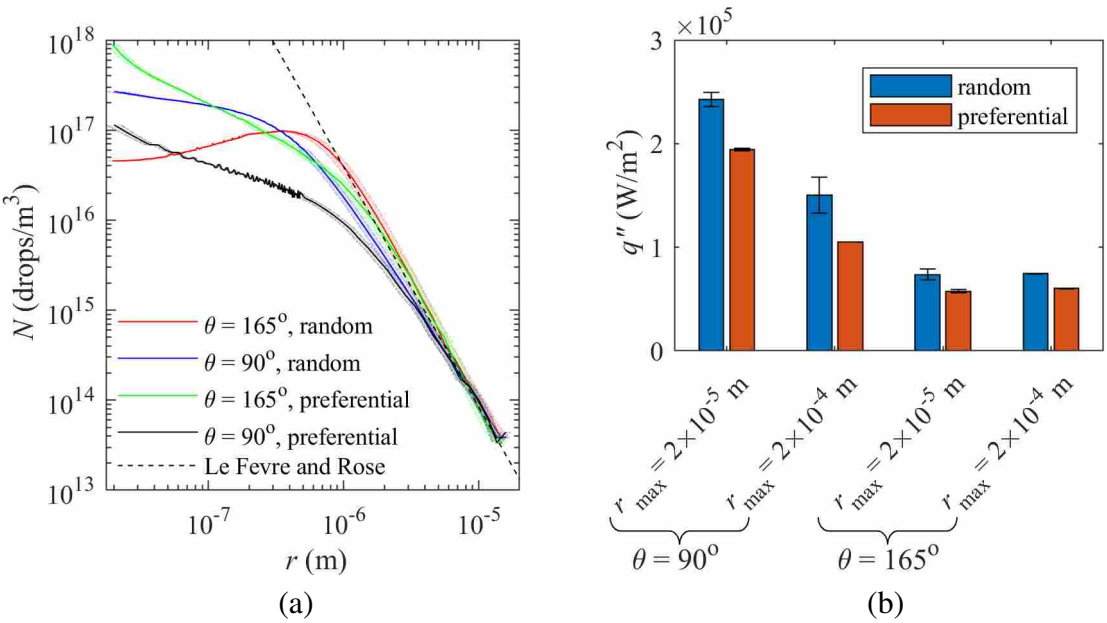

Figure 4.9: (a) Distribution functions for random and preferential nucleation schemes using the Adhikari heat transfer model for simulations with $N_s = 1 \times 10^{11}$ drops/m^2 and $r_{max} = 2 \times 10^{-5}$ m. (b) Time-averaged rates of heat transfer for the different nucleation schemes. A higher heat transfer rate is predicted when using the random nucleation scheme despite the fact that more small drops are predicted with the random nucleation scheme when the contact angle is large.

contact angle is high, the distribution for preferential nucleation sites is higher for smaller drops but lower for larger drops. The base area is smaller at higher contact angles, and when small drops coalesce, the resulting composite drop shifts just enough that the base no longer covers the "preferential" site, as described by Rykaczewski *et al.* [38]. This results in an average drop density slightly higher than N_s (1.07×10^{11} drops/m^2), in contrast to the random approach where the average drop density can never exceed N_s. Though the distribution functions are instructive, the time-averaged heat transfer rate is the most relevant outcome when considering the influence of the various approaches for distributing drops. As shown in Figure 4.9b, the random nucleation scheme consistently results in approximately 25% higher rates of heat transfer, regardless of the contact angle or maximum radius size. Notably, even in the case of large contact angles where the distribution function for preferential nucleation is much larger for smaller radii, the total heat transfer rate is still lower since the heat transfer rate for smaller drops is so much smaller. It is supposed that realistic condensation behavior would fall somewhere between these two new drop nucleation extremes, depending on the properties of the condensing surface.

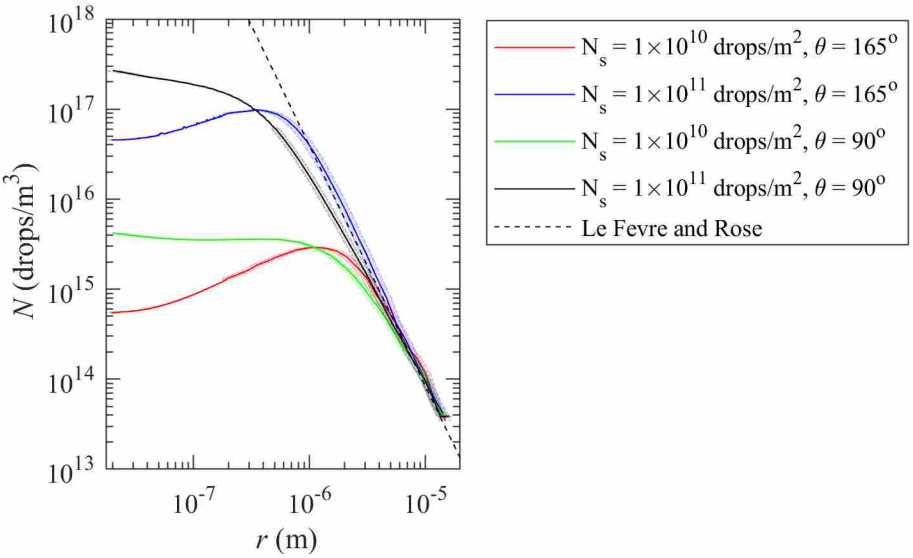

Figure 4.10: Influence of initial nucleation site density on the distribution function. The distributions shown were produced using the Adhikari heat transfer model, the random nucleation scheme, and $r_{max} = 2\times10^{-5}$. Drop-size distribution for small drops is highly dependent on the nucleation site density, as predicted by Kim and Kim [56]. Though only distribution functions produced with the random nucleation scheme are shown in the figure, the effect of nucleation site density is the same for the preferential nucleation scheme.

4.5.4 Influence of the Nucleation Site Density

The distribution function for two different nucleation densities is shown in Figure 4.10. The variation with nucleation site density generally follows the trend predicted by Kim and Kim [56], where the shape for different nucleation densities is generally similar with deviation observed where the distribution converges with the Le Fevre and Rose correlation [129]. The influence of varying the contact angle on the distribution function is also evident in Figure 4.10. For a contact angle of 165° the distribution generally slightly overshoots the power-law correlation. When the contact angle is 90°, the distribution generally undershoots the power-law correlation.

4.5.5 Influence of Maximum Drop Size and Contact Angle

The influence of r_{max} on the Le Fevre and Rose correlation [129, 130] is generally to shift the drop distribution to the left or the right. When the contact angle is 90°, the simulation predicts that increasing r_{max} will shift the distribution function to the left, as shown in Figure 4.11. However, when the contact angle is 165°, increasing r_{max} does not shift the distribution function, and

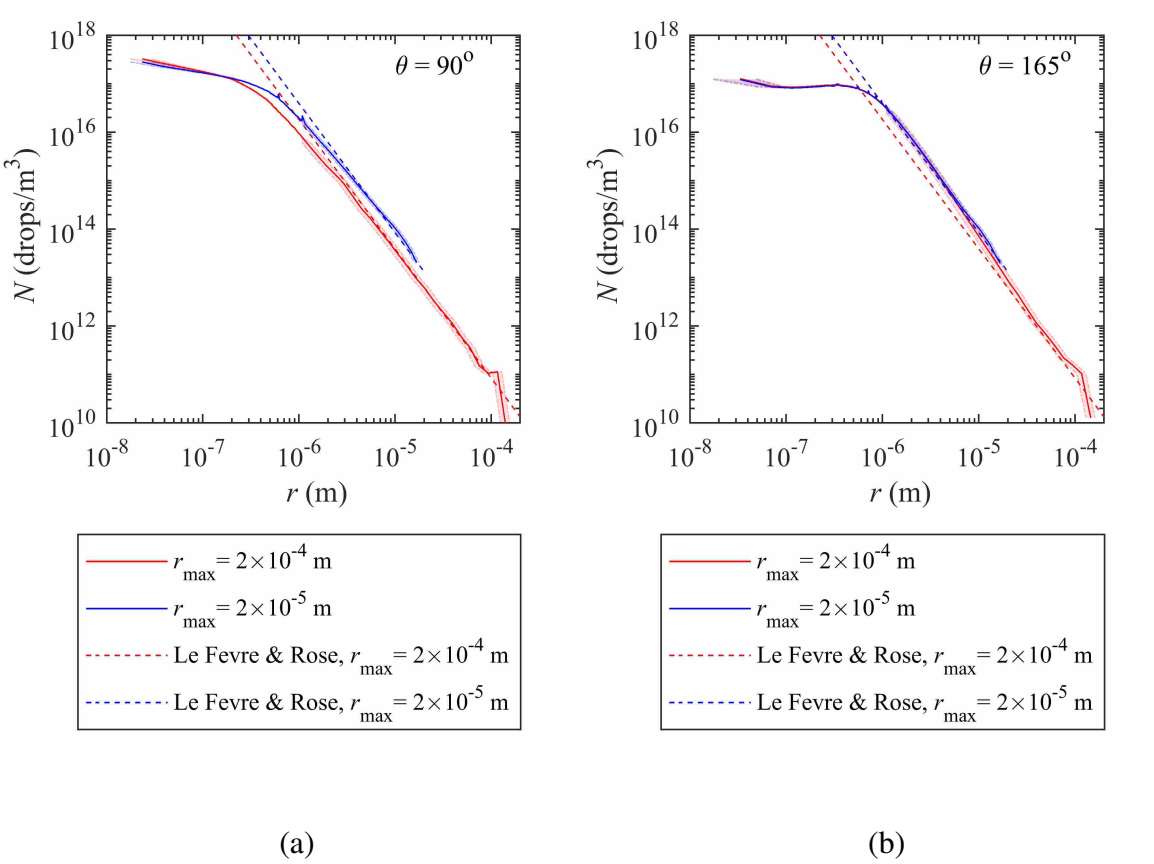

(a) (b)

Figure 4.11: Distribution functions created using the Adhikari model with a contact angle of (a) 90° and (b) 165°. When the contact angle is large, the distribution function is similar for large and small r_{max}.

the distribution with large r_{max} resembles that of small r_{max} until it diverges to the corresponding power-law curve. The cause for this can be understood by recognizing that as the contact angle increases, the area of the base decreases. In the extreme case where the contact angle approaches 180° and the base area approaches zero, it is clear that the maximum size of the drops would have much less influence on the distribution of smaller drops, which would easily fit in the shadow of the larger drops. In the case where drops have contact angles of 165°, the area of the base is still small, covering 5 and 10% of the total area for $r_{max} = 2\times10^{-5}$ and 2×10^{-4} m, respectively. Though the area of the substrate covered is twice as high for $r_{max} = 2\times10^{-4}$ m, the number of new drops only changes by 5% since the number of new drops is governed by equation 4.8.

The influence of r_{max} on heat transfer rate can be seen in Figure 4.12. When the contact angle is 90°, the heat transfer rate generally follows the trend predicted by the Kim and Kim [56]

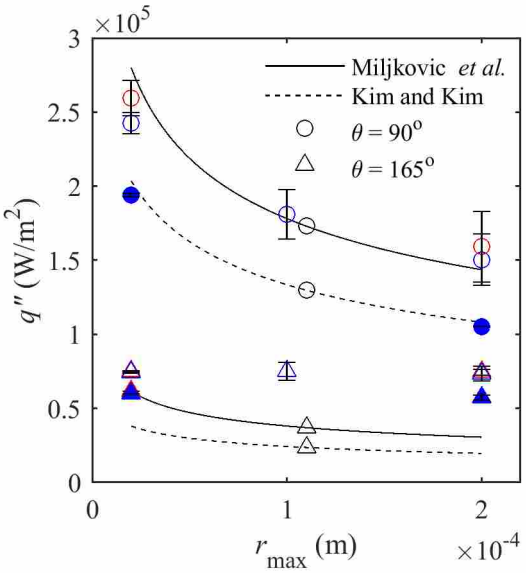

Figure 4.12: Time-averaged heat transfer rate predicted by the simulation compared with previous models as a function of the contact angle, θ. Results based on the Chavan heat transfer model are shown in red, while the results based on the Adhikari model are shown in blue. Filled markers indicate selection of the preferential nucleation approach to distribute nucleation sites; empty markers indicate the random nucleation approach. The simulation predicts that the heat transfer rates remains constant with increasing maximum drop size at high contact angles.

and Miljkovic *et al.* [17] models, with slight offsets for the difference in heat transfer model and nucleation scheme. However, when the contact angle is 165°, the simulation predicts that the heat transfer rate changes negligibly with r_{max}, in contrast to the trend predicted by previous models. In the simulation, the heat transfer rate changes little with r_{max} due to the extremely small base area when the contact angle is high. The simulation for $\theta = 165°$ predicts a heat transfer rate on the order of two times higher than the models when $r_{max} = 2 \times 10^{-4}$ m. At high contact angles it may be particularly hazardous to use previously proposed distribution models.

It should be noted that r_{max} is dependent on both the advancing contact angle and contact angle hysteresis. In order to simplify the parameter space and produce results independent of surface type, they have been considered independently in the present work. However, a surface with $\theta = 90°$ and $r_{max} = 2 \times 10^{-5}$ m is not physically realistic since surfaces with $\theta = 90°$ tend to have large contact angle hysteresis and maximum drop sizes on the order of 1-2 mm.

The influence of contact angle on heat transfer rate is indicated in Figure 4.13 (see also Figure 4.8). When the contact angle is 90°, the simulation predicts results similar to those of

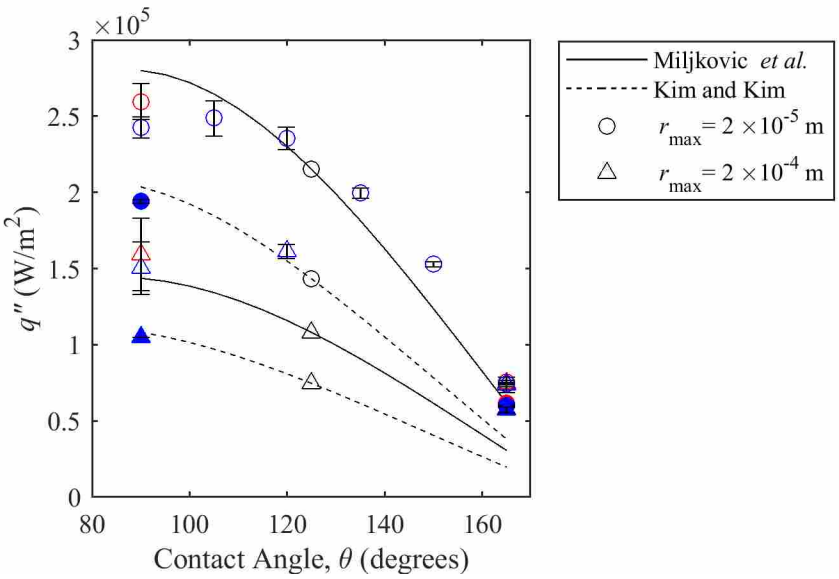

Figure 4.13: Time-averaged heat transfer rate predicted by the simulation compared with previous models as a function of the maximum drop size on the surface, r_{max}. Results based on the Chavan heat transfer model are shown in red, while the results based on the Adhikari model are shown in blue. Filled markers indicate selection of the preferential nucleation approach to distribute nucleation sites; empty markers indicate the random nucleation approach. The simulation predicts that the heat transfer rates converge to a single rate at large contact angles.

Miljkovic *et al.* [17], but as the contact angle increases the heat transfer rate converges regardless of the maximum drop size or heat transfer model. This has important implications for design of superhydrophobic condensing surfaces. Conventional wisdom supposed that the rate of condensation heat transfer is inversely proportional to the diameter of the condensate drops [7,61,155,157], which is true when the contact angle is low. However, at high contact angles the area of the base is so small that the presence of large drops does not significantly influence the surface area available for condensation, and the heat transfer rate is similar regardless of the maximum drop size, assuming the drops are still in a mobile, suspended or partially wetting state.

4.5.6 Coalescence Induced Jumping

The influence of droplet departure via coalescence-induced jumping on the distribution function and heat transfer rate is now considered. Since superhydrophobic surfaces with low adhesion are necessary for coalescence-induced jumping, all simulations which include jumping have a specified contact angle of 165°. The distribution functions for several simulations involving jump-

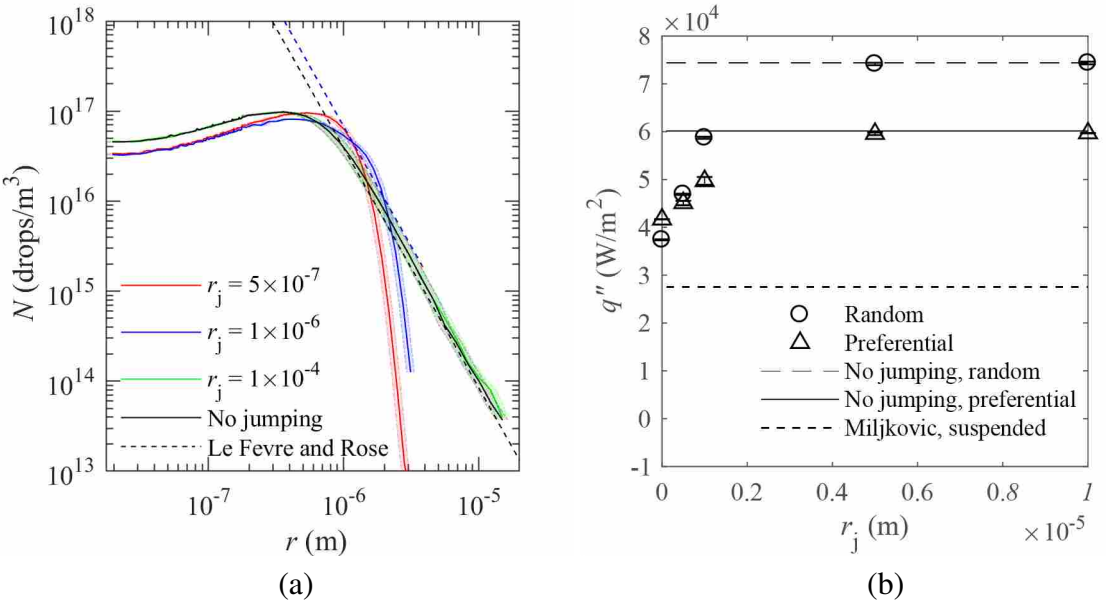

Figure 4.14: (a) Distribution function when drops larger than r_j depart via coalescence-induced jumping (b) Heat transfer as a function of r_j. When r_j is sufficiently small the preferential nucleation scheme the simulation predicts higher rates of heat transfer than the random nucleation scheme since the distribution is higher for drops in this size range (see Figure 4.9 and the accompanying discussion). The simulation predicts that the heat transfer rate decreases with decreasing drop departure size.

ing are shown in Figure 4.14a. At least two of the drops involved in the coalescence event must be larger than the minimum jumping radius, r_j. As r_j increases, the maximum size of drops on the surface increases since fewer coalescence events result in jumping and departure. For small drop radii where drops experience direct-condensation-dominated growth, larger r_j shifts the distribution up slightly since fewer drops are departing from the surface. At $r_j = 1\times10^{-5}$ m the distribution function becomes very similar to that for which no jumping occurs.

The heat transfer rate increases with increasing r_j until convergence with the no jumping case, as shown in Figure 4.14b. When r_j is sufficiently small, the simulation predicts higher rates of heat transfer when using the preferential nucleation scheme (as opposed to the random nucleation scheme) since the distribution with preferential nucleation is higher for $r < 8\times10^{-7}$ m (see Figure 4.9a and accompanying discussion). Interestingly, in this example case ($N_s = 1\times10^{11}$ drops/m^2), prohibiting jumping at smaller sizes increases the overall heat transfer rate since drops larger than 5×10^{-7} m comprise a significant portion of the total heat transfer rate when they do not depart,

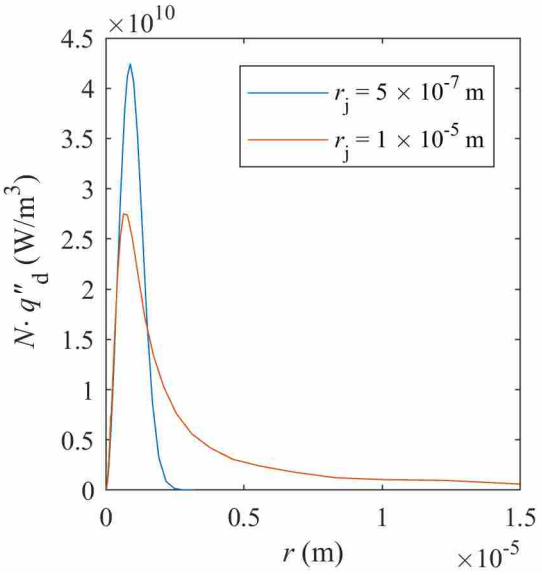

Figure 4.15: The product of the distribution function and heat transfer rate to a single drop, the integral of which is the overall heat transfer rate, q". The contribution of larger drops is significant and allowing them to depart at smaller sizes decreases the overall heat transfer rate. The contact angle in the case shown is $\theta = 165°$.

as illustrated in Figure 4.15. In this figure, the product of the $N(r)$ and $q_d(r)$, the integral of which is q", is shown as a function of r. When $r_j = 5\times10^{-7}$ m, the rate of heat transfer for drops smaller than 2×10^{-6} m is much higher than for $r_j = 1\times10^{-5}$ m, but the total heat transfer rate (for $r_j = 1\times10^{-5}$ m) is still higher (than for $r_j = 5\times10^{-7}$ m) since drops larger than 2×10^{-6} m contribute significantly to the overall heat transfer rate. When the contact angle is high, the presence of larger drops does not negatively influence the overall heat transfer rate due to the small base area. Furthermore, removing drops that are too small can decrease the overall rate of heat of heat transfer. Minimizing the maximum drop size may not always maximize the rate of heat transfer on a condensing surface.

The Miljkovic *et al.* [17] model for jumping is also shown in Figure 4.14b. In their model, all coalescence and departure occurs at $r = r_e = 1/(4N_s)$ (which corresponds to $r_e = 8\times10^{-7}$ m when $N_s = 1\times10^{11}$ drops/m^2), which eliminates the heat transfer that would be contributed by drops larger than this size. The immediate termination of the distribution curve at $r = 1/(4N_s)$ explains the significantly lower predicted rate of heat transfer.

4.6 Conclusion

A framework to obtain drop-size distribution functions during dropwise condensation on vertical surfaces was developed and used to explore the influence of the assumptions made in previous drop-size distribution models. The influence of individual drop heat transfer model, nucleation site distribution approach, nucleation site density, maximum drop size, and contact angle on the distribution function were also explored. Results of the simulation are valid for smooth hydrophobic or nanostructured superhydrophobic surfaces, where the assumptions of constant contact angle growth and negligible thermal resistance at the drop/surface interface are reasonable. The simulation includes the possibility for coalescence-induced jumping, where all drops above a specified threshold radius depart upon coalescence. Parameters dependent on surface structure and chemistry, including contact angle (θ), maximum drop size ($r_{\max}$), and minimum jumping radius (r_{j}), are specified to the simulation, so that each parameter may be independently determined for a given surface.

Results of the simulation suggest that population balance methods account for general trends in the drop-size distribution, but include certain assumptions that limit their accuracy. In particular, results of the current simulation suggest that setting the transition from direct-condensation-dominated growth to coalescence-dominated growth at $r_{\mathrm{e}} = 1/(4\sqrt{N_{\mathrm{s}}})$ may overestimate the drop-size distribution. With the lack of available experimental data for distributions in this size range, the present work represents the first attempt to evaluate the accuracy of the population balance modeling approach.

The heat transfer model used in the simulation influences both the distribution and the overall heat transfer rate, particularly for low contact angles. As more accurate models are developed (such as that of Xu *et al.* [156]) and combined with the results of the present work, the accuracy of the distribution function and prediction of the overall heat transfer rate may improve. The approach for distributing the nucleation sites influences both the distribution curve and the overall heat transfer rate. For the parameters explored in the present simulation, the random nucleation scheme resulted in heat transfer rates on the order of 25% larger than those predicted with the preferential nucleation scheme. Realistic nucleation behavior is likely a combination of the two nucleation approaches, and may be used to bracket realistic behavior.

As predicted by previous investigators [17, 56, 61, 136] and shown with the present simulation, nucleation site density N_s significantly influences the size at which drops begin to coalesce and size at which the distribution function approaches the empirical Le Fevre and Rose [129, 130] correlation. Nucleation site density can be difficult to measure and to predict, though it is influenced by the physiochemical properties of the substrate, surface subcooling, and atmospheric pressure [61, 145, 155]. While it would be desirable to be able to predict the heat transfer rate as a function of surface subcooling, the ability to predict $N_s(\Delta T)$ is a prerequisite.

Results of the simulation suggest that, when $N_s = 1\times10^{11}$ drops/m^2, removing drops at extremely small sizes via coalescence-induced jumping can lead to lower heat transfer rates due to the fact that the heat transfer rate to larger drops is significant. The model proposed by Miljkovic *et al.* [17] under-predicts the heat transfer rate for jumping drops since it does not consider heat transferred to drops that are larger than the equilibrium radius. In the present work, whether coalescence will result in drop departure or not is determined based on a specified minimum jumping size; however, the structure of the simulation allows for the use of more sophisticated models for drop jumping. For example, a model for jumping based on an energy balance between the adhesive force of the drops and energy released upon coalescence could be evaluated for each coalescence event, enabling the inclusion of factors such as surface feature length scale, drop wetting state, relative size mismatch, and number of drops involved in a coalescence event.

When the contact angle is large, the influence of increasing the maximum drop size on the distribution and overall heat transfer rate is minimized due to a smaller base area. Previous models deviate most from the current results at large contact angles, suggesting that previous models may be less accurate when the contact angle is large. Furthermore, these results suggest that removing large drops may not necessarily be the most advantageous for increasing overall heat transfer rates. Additionally, the recent work of Xu *et al.* [156] suggests that convection is a significant contributor to the heat transfer rate for larger drops (becoming significant for drops between 5 and 200 μm, depending on the rate of subcooling and contact angle). Since the models included in this analysis consider only conduction, the heat transfer rate for large drops where convection becomes significant may be under predicted. When convection is included in the model for heat transfer to an individual drop, it may be even more advantageous for large drops to remain on the surface.

The present work offers insight into factors which are important when modeling condensation heat transfer. The large parameter space precludes formulation of a closed-form distribution function. Furthermore, as understanding of condensation behavior improves, the current approach may be updated for improved accuracy, including improved models for coalescence-induced departure and individual drop heat transfer. Accordingly, the MATLAB code used to run the simulation can be found in Appendix B and will be provided upon request.

CHAPTER 5. INFLUENCE OF SUBCOOLING AND SURFACE FEATURE SIZE ON DROP WETTING BEHAVIOR AND DROP-SIZE DISTRIBUTION DURING CONDENSATION ON SUPERHYDROPHOBIC SURFACES

5.1 Contributing Authors and Affiliations

Kimberly A. Stevens, Clint Hubbard, Joseph Seamons, Julie Crockett, Daniel Maynes, Brian D. Iverson

Department of Mechanical Engineering, Brigham Young University, Provo, Utah 84602

5.2 Introduction

Condensation heat transfer is an essential process in applications such as water desalination and harvesting [63, 125, 126], energy conversion [1, 9, 127], electronics cooling [4], and environmental control [128]. However, condensate buildup at a surface adds thermal resistance which limits condensation rates. Dropwise condensation has been shown to have heat transfer rates 5-7 times higher than filmwise condensation, generating considerable interest in developing surfaces that can sustain dropwise condensation [6,7]. On surfaces undergoing dropwise condensation, thermal resistance is typically minimized by removing condensate via gravity or a vapor shear, but the minimum size of drop removal is typically on the order of the capillary length of the condensate, approximately 2.7 mm for water.

Properly designed superhydrophobic surfaces have been shown to promote the removal of condensate at sizes significantly below the capillary length due to low contact angle hysteresis and coalescence-induced jumping of condensate drops. With the removal of condensate drops due to coalescence-induced jumping, the maximum droplet diameter can be reduced by 1 to 3 orders of magnitude [41, 43]. The potential for superhydrophobic surfaces to significantly impact condensation heat transfer has promoted a great deal of exploratory research regarding the fundamental behavior of condensing droplets on superhydrophobic surfaces.

The wetting state of condensing drops determines whether coalescence-induced jumping can occur and the overall heat transfer rate. When drops form on top of a superhydrophobic surface structure with sufficiently low surface energy they will continue to grow above the structures in a non-wetting, suspended state. When condensing drops initiate and grow within a superhydrophobic surface structure, they can emerge either into a partially wetted or wetted state. Drops in a wetted state are highly pinned, leading to loss of mobility and flooding, and will not depart from the surface due to coalescence-induced jumping. Flooded surfaces have been shown to exhibit decreased rates of heat transfer relative to dropwise condensation on a smooth surface [35].

Condensing drop motion (coalesce-induced jumping and sweeping, gravity-driven shedding and sweeping) is dictated by all of the forces acting on a drop, including gravity, adhesion between the drop and the surface, and impingement of the liquid bridge formed during coalescence. The total adhesive force between the drop and the surface includes any adhesion felt by a drop placed on a dry, adiabatic surface and the additional adhesion which may occur during condensation. The magnitude of the adiabatic adhesive force is often approximated from the contact angle hysteresis [17, 56]. The additional adhesion which may occur during condensation on a structured surface can result from increased contact surface area due to partially wetting drop behavior, but relatively little is known regarding this force. The present work offers additional insight into factors which influence the additional adhesion that may occur with condensation. Regardless, coalescence-induced jumping and sweeping will occur when the force of the impinging liquid bridge is greater than the total adhesive force between the surface and the drop. Gravity-driven shedding occurs when the drop grows sufficiently large so that the weight of the drop is larger than the total adhesive force, and the drop falls.

Two criteria have been proposed which can conservatively approximate the wetting state of condensing drops [29]. First, it must be energetically favorable for drops to emerge into a suspended or partially wetting state, as determined by comparison of the surface energies associate with the Cassie-Baxter and Wenzel states.

$$E^* = \frac{\cos\theta_a^{CB}}{\cos\theta_a^{W}} = \frac{-1}{r_s \cos\theta_a} \tag{5.1}$$

where θ_a is the apparent contact angle on a smooth surface and r_s is the surface roughness. If $E^* > 1$, the Wenzel or wetting drop morphology is favored, whereas if $E^* < 1$ partially wetting or suspended drops can form. The second criteria for the formation of partially wetting and suspended drops is that the nucleation density must be less than the density of the structures, or $< L > / l >$ 2-5, where l is the average spacing between structures and $< L >$ is the average distance between nucleation sites. If the nucleation density is too high, nucleation mediated flooding will occur with highly pinned, immobile drops, not only preventing coalescence-induced jumping, but also decreasing the overall rate of heat transfer. Both criteria must be satisfied to prevent the formation of completely wetting drops. Based on these criteria, both the surface structure and nucleation density are known to influence the wetting state of condensing drops.

Surface structure influences other condensing drop dynamics in addition to wetting. In particular, it has been demonstrated that the microstructure influences condensing drop behavior [30, 34, 36, 49, 50, 158–161]. Rykaczewski *et al.* explored the impact of the microstructure topography on surfaces with pitches varying from zero (no microscale topography) to 120 μm and found that the pitch influences the micro-wetting state and post-coalescence adhesion and departure. Accordingly, the maximum diameter also changes with pitch [34]. They showed that the microstructure influences the fraction of coalescence events that result in departure and concluded that a pitch of 64 μm was ideal for promoting droplet departure. Chen *et al.* found that microscale feature pitch affects the drop jumping height following coalescence [36]. Though much remains to be understood regarding the influence microstructure has on condensing drop behavior, microstructure is clearly important.

Nanoscale features also influences drop dynamics. Feng *et al.* varied oxidation times on fluorinated copper surfaces to obtain a range of nanoscale feature sizes and found that the rougher the structure, the higher the drop mobility [162]. Cha *et al.* varied the thickness of polymer-coating carbon nanotubes (CNTs) to change the solid fraction and found that drops as small as 500 nm can experience coalescence-induced jumping [43]. They predicted the minimum jumping size as a function of surface solid fraction and apparent advancing contact angle. In a related work it was shown that changing the length scale (l = 100, 300, and 1000 nm) had no influence on the jumping drop speed since drops were able to jump for all length scales tested [91]. Mulroe *et al.* [44] and Mouterde *et al.* [42] also showed the the nanostructure influences the minimum drop

departure size. In particular, Mouterde *et al.* showed the shape of the nanostructure is important, since a surface with nanocones experienced jumping whereas a similar surface with nanopillars experienced almost none. Mouterde *et al.* also measured the total adhesive force for drops on a surface, differentiating between the "intrinsic" adhesive force present when no condensation occurs and a "condensation-induced" adhesive force, which results from pinning when condensate grows from within the surface structures. They showed that the condensation-induced adhesive force is sensitive to nanostructure spacing. All of the drop dynamics described (minimum jumping size, drop mobility, jumping speed and height, fraction of coalescence events that result in departure, maximum drop size) are related to the total adhesive force, and it can be concluded that both microstructure and nanostructure influence the adhesive force a drop experiences during condensation.

Less work has been done exploring the influence of surface subcooling on condensing drop adhesion. Mouterde *et al.* showed that what they termed "the condensation-induced adhesive force" is dependent on subcooling [42]. Wen *et al.* showed that as the transition to flooding can be delayed by spatially controlling nucleation using dense nanostructures [51, 57, 58]. The nanostructures were sufficiently dense to limit the amount of vapor between the structures, encouraging the formation of suspended drops. The prevalence of suspended drops enables the surface to reach higher supersaturations before flooding occurs and higher heat fluxes than reported in the past. For dense structures, they explain that the wetting transition occurs due to loss of control over nucleation site location. As the subcooling increases, nucleation size decreases and drops are able to nucleate within the nanostructures, leading to flooding. They describe that the transition from jumping to flooding includes an intermediate state they termed "sweeping" where jumping no longer occurs, but drops maintain high mobility. They also found that drop adhesion increases with subcooling [51].

Knowing the drop-size distribution is essential in order to predict condensation heat transfer. Models for condensation heat transfer typically integrate the product of heat transfer to an individual drop and the drop size distribution over the range of drop sizes found on a surface to obtain overall heat transfer rates. The drop-size distribution of drops that grow mainly by coalescence

with other drops is well established [7] as

$$N(r) = \frac{1}{3\pi r^2 \hat{r}} \left(\frac{r}{\hat{r}}\right)^{-2/3}, \tag{5.2}$$

where $\hat{r}$ is the average maximum radius of the drops. In contrast, various models of drops which grow mainly by direct condensation have been proposed, but no experimental drop-size distribution measurements exist due to the difficulty of observing drops sufficiently small that their growth is dominated by direct condensation. Furthermore, few works have modeled the drop-size distribution in the size range where drops begin to depart from the surface despite experimental measurements which clearly indicate divergence from the power-law distribution [130, 133]. Drops that depart due to gravity or vapor shear are believed to contribute minimally to the overall heat transfer rate; immediately terminating the distribution curve at the departure size may reasonably approximate the distribution without changing the predicted heat transfer rate. However, when drop departure occurs over a range of sizes, as with coalescence-induced jumping, the departure region can account for a larger portion of the heat transfer rate (see chapter 4). Prior to the work in chapter 4, only one theoretical drop-size distribution model for surfaces that experience coalescence-induced jumping had been proposed, and in that work none of the drops coalesced prior to the average departure size, at which point all drops departed at a single size [17]. Experimentally measured drop-size distributions with coalescence-induced departure have been limited to coarse histograms lacking sufficient resolution to create or validate a drop-size distribution model suitable for heat transfer modeling.

The first part of the present work describes subcooling-driven drop behavior transition which occurs on surfaces that do not spatially control nucleation site formation (in contrast to the work of Wen *et al.*). Increased subcooling leads to less coalescence-induced drop jumping and departure and the presence of larger drops on the surface. The gradual cessation of jumping and an accompanying increase in drop size suggests that the wetting transition occurs as a result of gradually increasing drop adhesion, which may result from increased nucleation density and pinning. The gradual change in drop adhesion and departure propensity is shown to change the drop-size distribution. The second part of the present work reports drop-size distributions on superhydrophobic surfaces with coalescence-induced jumping during condensation on a vertically

oriented surface with sufficient radial resolution to provide insight regarding how wetting state influences the departure region of the drop-size distribution.

5.3 Methods

5.3.1 Surface Fabrication and Characterization

In order to explore the influence of nanostructure size during condensation, surfaces are created which allow modification of the nanostructure while maintaining superhydrophobic behavior, following previous work [90]. Iron is vapor deposited on alumina-coated silicon wafers coated with iron, and carbon-infiltrated carbon nanotubes (CICNTs) are grown uniformly as described by Stevens *et al.* [90]. The surface is functionalized by vacuum baking at 250 °C for approximately 16 hours [90, 118]. By rendering the native carbon surface hydrophobic, no additional chemical coating is required, creating a surface that is relatively robust compared with many of the polymer or self-assembled monolayer coatings typically used. The diameter of the carbon-infiltrated carbon nanotubes is varied by depositing a layer of amorphous carbon on the carbon nanotubes [90, 163–165]. The CICNT diameter is measured with top-down scanning electron microscopy, where each reported measurement is the average of at least 20 different CICNTs. All surfaces had an advancing contact angle of approximately $157° \pm 3°$ and hysteresis $< 3°$, regardless of the CICNT diameter.

5.3.2 Condensation Chamber

In order to minimize the effects of noncondensable gases, experiments are performed inside a stainless-steel vacuum chamber with polycarbonate windows, as shown in Figure 5.1. Additional details regarding chamber construction can be found in Appendix E. Prior to running experiments, water in an Erlenmeyer flask is boiled rapidly for at least 10 minutes by lowering the pressure with a two-stage rotary vane pump (Edwards, E2M2). The valve to the vacuum pump is closed, and the flask remains at vapor pressure for 24 hours. The boiling/sitting procedure is repeated until all of the nucleation bubbles in the flask have been eliminated so that all phase change occurs at the free surface of the water. The procedure is repeated every time the water inside the flask is

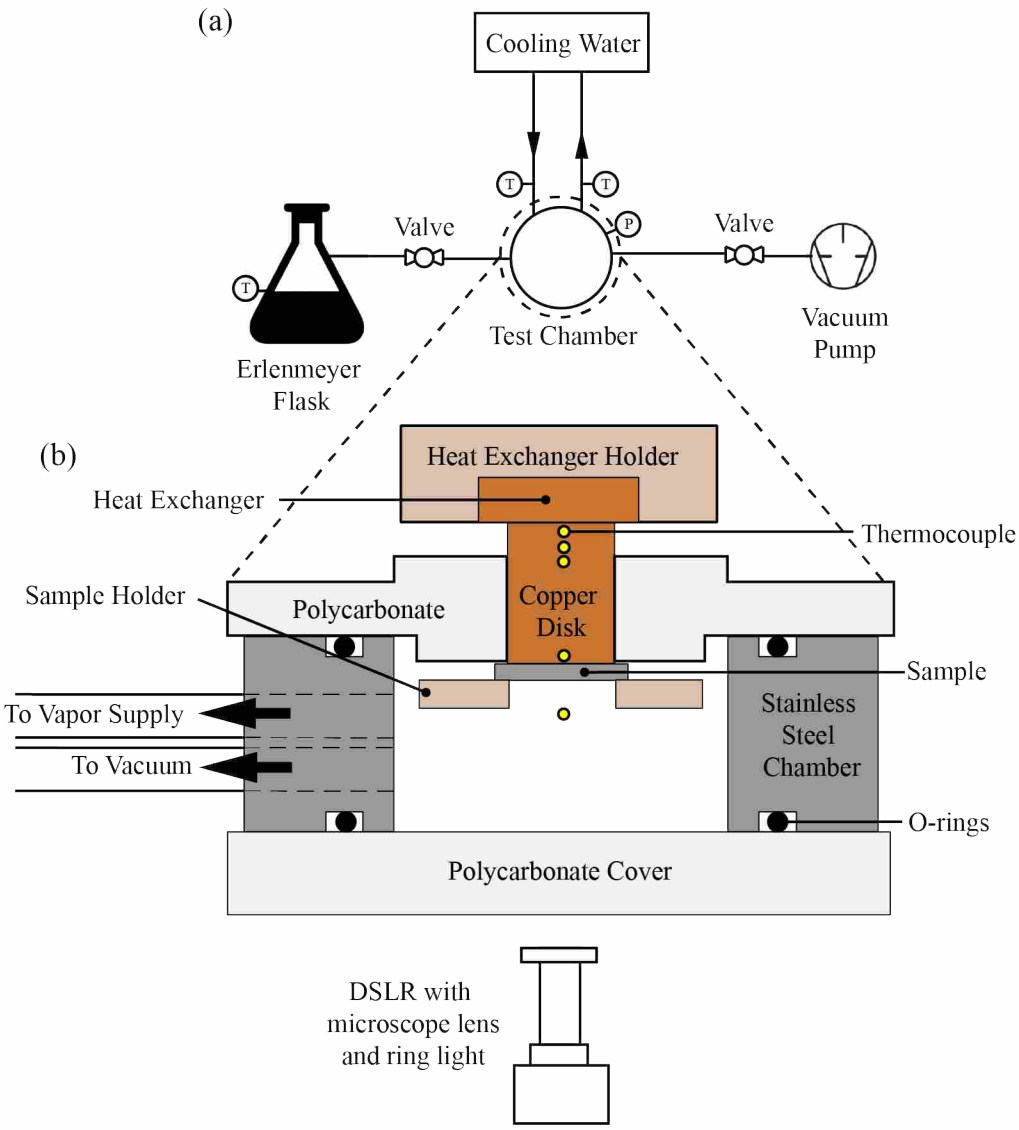

Figure 5.1: (a) Schematic of the condensation setup. In order to minimize in the influence of noncondensable gases, the valve to the water supply is closed and the rest of the loop is kept under vacuum overnight prior to performing each experiment. (b) Top-down view of the vacuum chamber with polycarbonate walls to enable visualization of condensing surface.

exposed to air. Prior to each condensation experiment, the valve between the flask and the vacuum chamber is closed, and the chamber is evacuated to a pressure less than 3 Pa (Kurt J Lesker AA01A01TGAS3B00000, FS 1 Torr, $+/-$ 0.25% accuracy) and held overnight, so that the rate of pressure rise (due to outgassing from the chamber walls) is less than 0.5 Pa/min. The rate of pressure rise is measured prior to each experiment to ensure that the concentration of noncondensable gases remains below 0.6%.

A constant temperature bath supplies coolant water to a heat exchanger used to cool the condensing surface in the chamber, as shown in Figure 5.1. A second pressure gauge (Omega PX409-005A10V) measures the vapor pressure to obtain the saturation temperature (T_{sat}) and a thermocouple monitors the vapor temperature inside the chamber to ensure saturated conditions. The superhydrophobic surface is attached to the copper block (thermally connecting the heat exchanger and the surface) with a thin layer of Dow Corning high vacuum grease to minimize contact resistance. The surface is then bolted to the copper block, and a torque wrench is used to apply consistent clamping force (0.225 N-m) for each test. The surface temperature is approximated using a thermocouple embedded in the copper block (T_c), approximately 2 mm from the surface. Though it is difficult to know the exact surface temperature due to the contact resistance between the surface and the copper block, the contact resistance remains the same throughout the duration of a test, and efforts are made to ensure consistent contact resistance between tests. The thermal resistance through copper and silicon wafer (0.5 mm) is negligible. Therefore, the real subcooling will scale with the measured subcooling, ($T_{sat} - T_c$).

The condensation tests proceed as follows. After measuring the outgassing rate, the chamber is vacuumed down to a pressure less than 3.25 Pa. The valve to the vapor supply is then opened and water vapor floods the chamber. The vacuum pump continues to run for 5 minutes to ensure removal of any additional noncondensable gases, and then the valve to the vacuum is closed. Coolant water from the constant temperature bath is then circulated through the heat exchanger and condensation begins on the surface. The degree of subcooling is controlled by setting the temperature of chiller bath. After the chiller bath reaches the set temperature, condensation occurs for at least 10 minutes and video is recorded. In some cases, the surface is exposed to multiple subcooling temperatures during a single test run. For these multiple subcooling test cases, after 10 minutes, the subcooling is increased and video is recorded after reaching steady state for the new subcooling. Temperature and pressure are recorded throughout the test run using an NI-DAQ at 4 hz. The degree of subcooling is determined by averaging over the steady state portion where the subcooling changes by less than 0.2 °C (at least 8 min). All thermocouples in the system are calibrated with an uncertainty of $\pm$ 0.05 °C.

During condensation the surface is observed using an optical microscope (Keyence VH-Z50L/W) attached to an SLR camera (Nikon D5200), and videos of the condensation were recorded

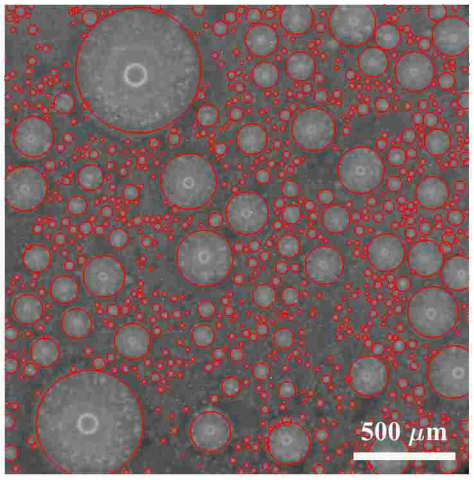

Figure 5.2: A single video frame showing condensed drops. The red outline indicates the size and location of the drop found in the drop tracking algorithm.

at 30 frames per second. The surface is illuminated using a fiber-optic ring light (light from Hayashi LA-150UE lamp) attached to the microscope lens. Once condensation reaches steady state at each level of subcooling, video of the condensing drops is recorded. The size and location of drops in each video frame are tracked in MATLAB using an approach inspired by active contour modeling [166], as shown in Figure 5.2. A "seed point" is found for each drop based on the contrast in light intensity, and the seed expands until it is constrained by boundaries formed from the absence of drops. Drop size is tracked throughout the video. The time-averaged drop-size distribution is obtained as follows. The number of drops whose size falls within $\pm$ 10-20% of 100 logarithmically spaced points are counted. The default size range is 10% unless there are fewer than 1000 drops in the range, in which case the range is increased to be as high as 20%. The count is then divided by the area of the field of view, the size range width, and the number of video frames to obtain the time-averaged drop-size distribution, N, with units of drops/m^3. The distribution function is always shown with error bounds associated with the selected size range width using light shading. The drop-size tracking code and analysis package are provided in Appendix C.

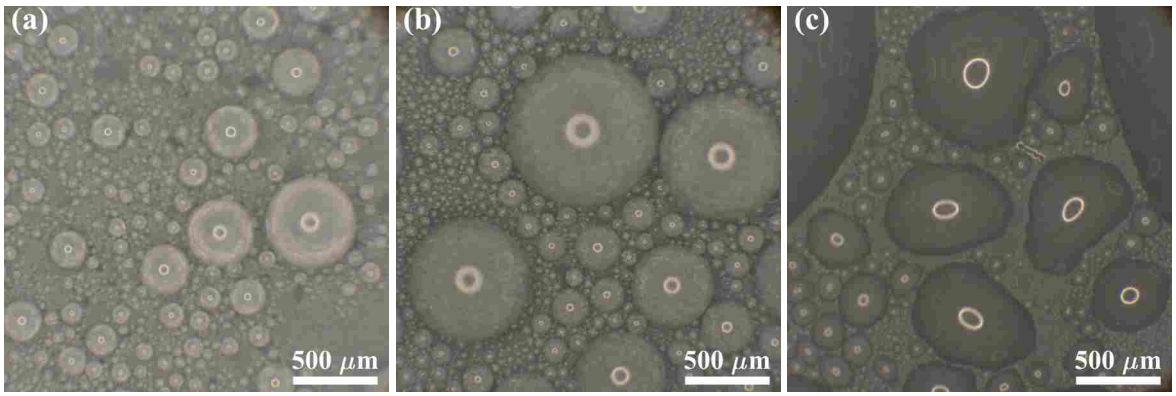

Figure 5.3: (a) Surface images with (a) jumping, (b) non-jumping, and (c) flooding drops.

5.4 Results

With time and variation in surface subcooling and CICNT diameter, variation in condensing drop behavior was observed. Drop behavior can be classified into three distinct categories or regimes, which reflect a change in drop adhesion. Surfaces are classified to be in a "jumping" state if any coalescence events result in jumping and departure. As drop adhesion to the surface increases, fewer coalescence events result in departure, leading to larger drops on the surface. For jumping to occur, drops must be in a suspended or partially wetted state. Jumping occurs when the liquid bridge formed between coalescing drops impinges on the surface, providing a force opposing the adhesive force and pushing the drop away from the surface. A surface is classified as "non-jumping" when no coalescence events result in jumping, but drops maintain a spherical-cap shape and high mobility (drops move as a result of coalescence and shed due to gravity when they grow sufficiently large). Cessation of jumping occurs as the total adhesive force becomes larger than the force of the impinging liquid bridge formed during coalescence. Wen *et al.* described a sweeping behavior where large coalescence events result in a drop with insufficient kinetic energy for drops to completely depart the surface via jumping, but sufficient energy to sweep across the surface, including in directions other than that in which gravity acts [51]. Surfaces exhibiting sweeping behavior fall into the non-jumping category. However, not all "non-jumping" surfaces exhibit sweeping. As the drop adhesion continues to increase, drops become less mobile and the the sweeping behavior also ceases. A "flooding" surface is classified by highly pinned drops which are no longer spherical. Over time, the condensate merges to form a film. The drop behavior regimes described are shown in Figure 5.3.

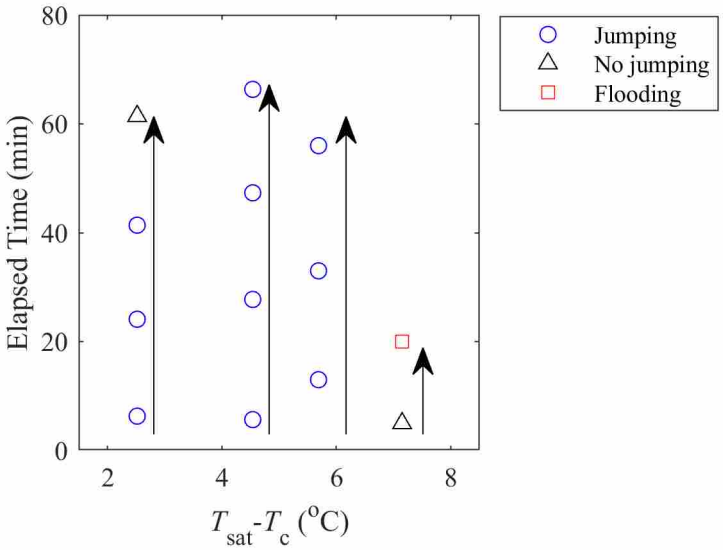

Figure 5.4: Drop behavior for surfaces as a function of the length of time water had been condensing and surface subcooling. The drop behavior is weakly dependent on time. CICNT diameter = 57 nm. Tests were completed on four different surfaces (indicated by arrows) where the subcooling was held constant for 70 minutes to observe the change in drop behavior with time.

5.4.1 Time Dependence

As water condenses on a surface at a constant degree of subcooling, the size of drops increased slightly with time, but classification of drop behavior was relatively independent of time, as shown in Figure 5.4. Drop-size distributions from videos taken at various elapsed times since condensation commenced on the surface are shown in Figure 5.5. The distribution function generally shifts to the right with increasing time, indicating an increase in the number of large drops. To show the trend more clearly, the average radii of the 10 largest drops in each frame is calculated, and then averaged through time over approximately 3 minute periods and shown in Figure 5.6. The size of the largest 10 drops is increases slightly with time (approximately 20–50% over the course of 60 minutes), indicating an increase in drop adhesion.

There are several possible explanations for the temporal variation in drop behavior and size-distribution. For instance, a transition may occur as vapor diffuses into the CICNT forest. When vapor is first introduced into the chamber, the pressure in the space between the CICNT structures is approximately 3 Pa and the pressure immediately above the structures is the water vapor saturation pressure, approximately 2 kPa in these experiments. With time, the higher pressure water vapor

diffuses into the structures, which are approximately 15 μm high. As the water vapor penetrates the CICNT forest, it is expected that nucleation sites will occur further down into the forest. Drops which originate from nucleation sites deeper in the forest may be have a higher total adhesion than drops which originate from nucleation sites located closer to the top of the surface, thereby causing a transition in drop size and behavior. Alternatively, the transition may result from an increase in the number of locally wetted pockets in the forest. As drops nucleate and grown within the nanostucture, they can grow up and out of the nanostructure, resulting in a partially wetting state, where the drop resembles a balloon with a pinned neck extending into the structure. It is well known that partially wetted drops can depart via coalescence-induced jumping, but it is unclear whether the entire drop volume, including the pinned neck also departs or whether the volume fragments upon coalescence and departure, leaving behind a portion of the pinned neck and making a locally wetted spot within the nanostructure. If coalescence-induced jumping events can result in locally wetted areas in the nanostructure, over time the density of these locally wetted areas would increase and could explain the transition in drop-size distribution and behavior. A third explanation for the transition may be the growing flooding front that originates from the edge of the CICNT surface. Tested surfaces were attached to a cooled copper block by bolting a plastic clamp which held the surface to a polycarbonate block in which the copper block was epoxied (see Figure 5.1b). The holder interfaced with the superhydrophobic surface around edges, crushing the nanostructures directly beneath the clamp. As a result, during condensation the area adjacent to the holder would flood, and the flooding front progressed inward during the test. The flooding front did not cover the majority of the surface, but it is possible that its presence caused the weak temporal variation in drop size observed. Further work is required to determine the exact cause of the transition in drop behavior and distribution with time.

5.4.2 Subcooling Degree and Nanostructure Size Dependence

Drop behavior classification on surfaces with varying CICNT diameters and levels of subcooling is shown in Figure 5.7. Some of the data shown in this figure were taken up to 2 hours following the initiation of condensation on the surface. Since the drop behavior classification is weakly dependent on time, onset of non-jumping and flooding may be shifted slightly to toward smaller degrees of subcooling relative to that expected for short times. For a given feature size of

CICNT surfaces, as subcooling increases, drop behavior transitions from jumping to non-jumping to flooding, and this transition is the same regardless of the elapsed time since condensation commencement. The change in drop behavior results from a change in drop adhesion. Since the intrinsic adhesive force on the surface remains the same with increased subcooling, the change in drop behavior is likely result from a change in the condensation-induced adhesive force. This agrees with observations by Wen *et al.* and Mouterde *et al.*, who measured increasing drop adhesion with increasing subcooling [42, 51].

The diameter of the CICNTs also influences the drop behavior. No jumping occurs on surfaces with average CICNT diameter larger than 60 nm. The contact angle hysteresis, which is frequently used as a measure of adhesion for a drop on a dry surface, does not change with CICNT diameter over the range of diameters tested in the present work [90]. Therefore, the change in drop behavior indicates a change in total drop adhesion. The increased adhesion may result from increased pinning, since the spaces between the CICNTs with larger diameter are smaller and drops that form within the structure likely have a more difficult time transitioning to a partial wetting state. Regardless of the cause, the change in drop adhesion with CICNT diameter and subcooling highlights an important but overlooked principle regarding adhesion of drops on structured surfaces. Contact angle hysteresis only considers solid-liquid interactions at the three-phase contact line [16]. Pinning near the drop center has no influence on the hysteresis but a large influence on the total adhesion. The surface structure and subcooling both influence the total adhesion, which governs drop behavior.

The drop-size distribution for various levels of subcooling are shown in Figure 5.8 for surfaces with CICNT diameter = 57 nm. The distributions shown correspond to conditions within 15 minutes of condensation commencement. The degree of subcooling significantly affects the drop-size distribution. With increasing subcooling, drops are able to grow to larger sizes as fewer coalescence events result in departure, which is a result of increased adhesion. Coalescence-induced departure of drops occurs at all of the conditions shown in Figure 5.8 and begins to significantly influence the drop-size distribution at the point where the distribution curve departs from the power-law function predicted by Le Fevre and Rose [129, 130]. When drops depart the surface via gravity-driven shedding, departure occurs when a drop grows to a size sufficient for gravity to overcome the adhesion and the drop falls. Therefore, though the shedding drop size may vary with

the local adhesion (dependent on surface defects, non-homogeneity in native surface chemistry, etc.), the size variation is generally relatively small and departure from a power-law distribution is relatively sudden, as shown by Wanatanabe *et al.* [133]. In contrast, since coalescence-induced departure occurs over a relatively larger range of drop sizes, the departure from the Le Fevre and Rose distribution is more gradual, as shown in Figure 5.8 and predicted in chapter 4. The larger departure region for coalescence-induced departure contributes more significantly to the overall heat transfer rate than the departure region for gravity-driven departure. The slope and radius at which the experimentally measured distribution function diverges from the Le Fevre and Rose prediction appears to be dependent on the degree of subcooling.

One potential explanation for the increase in adhesion with subcooling may stem from increased nucleation density. Increased nucleation density has been suggested as the cause of flooding at increased subcooling, as described by the criteria that the nucleation density must lower than the structure density. As the distance between nucleating droplets decreases to less than 2–5 times the spacing of the nanostructures, multiple drops can nucleate and grow to coalescence within the surface structure, forming a film within the structures so that all drops are wetted, leading to flooding [8,29]. However, as demonstrated here, the transition from jumping to flooding is gradual. Partially wetted drops locally wet the cavities between nanostructures with a characteristic "pinned neck". As coalescence-induced jumping occurs and drops depart the surface, the locally wetted cavity can remain, becoming a nucleation site for the formation of subsequent drops. As the nucleation density increases prior to the point of nucleation-mediated flooding, it is reasonable to suppose that the density of the locally wetted areas also increases, so that a partially wetted drop may be in contact with multiple pinned necks, thus gradually increasing the adhesion.

5.5 Conclusions

Condensate drop behavior (jumping, non-jumping, and flooding) and size distribution are dependent on the degree of subcooling and nanostructure size, and weakly dependent on the elapsed time condensation occurs on the surface. Increased subcooling causes a gradual increase in drop-size distribution and transition in drop behavior from jumping to non-jumping to eventual flooding. Increasing the surface feature size leads to transition in drop behavior for smaller de-

grees of subcooling. The change in behavior and drop-size distribution result can be explained by an increase in total drop adhesion.

The adhesion of a drop in the absence of condensation, represented by the contact angle hysteresis, is constant on all surfaces tested, and does not change with time or subcoooling. A change in total adhesion, indicated by the change in drop propensity to jump, must result from a change in adhesion caused by condensation and adds further evidence to the idea of an adhesive force separate from the intrinsic adhesive force, as described by Mouterde *et al.* [42]. The observation of additional adhesion which changes with subcooling and nanostructure independently of the contact angle hysteresis indicates that the adhesion a condensing drop experiences cannot be characterized by hysteresis measurements made on dry surfaces in the absence of condensation. In order to predict total drop adhesion, the additional adhesion which occurs with condensation and changes both with subcooling and structure, must be included. The total drop adhesion is relevant when considering whether coalescing drops will depart via jumping as well as the influence of vapor shear on drop departure in flow condensing environments.

Drop-size distributions for surfaces experiencing coalescence-induced jumping were obtained experimentally for the first time. The gradual departure from the Le Fevre and Rose distribution function is similar in shape to that predicted in chapter 4, serving as initial experimental validation of the results predicted from the simulation. Understanding the drop-size distribution in the departure region is important since drops in this size are expected to contribute significantly to the overall heat transfer rate.

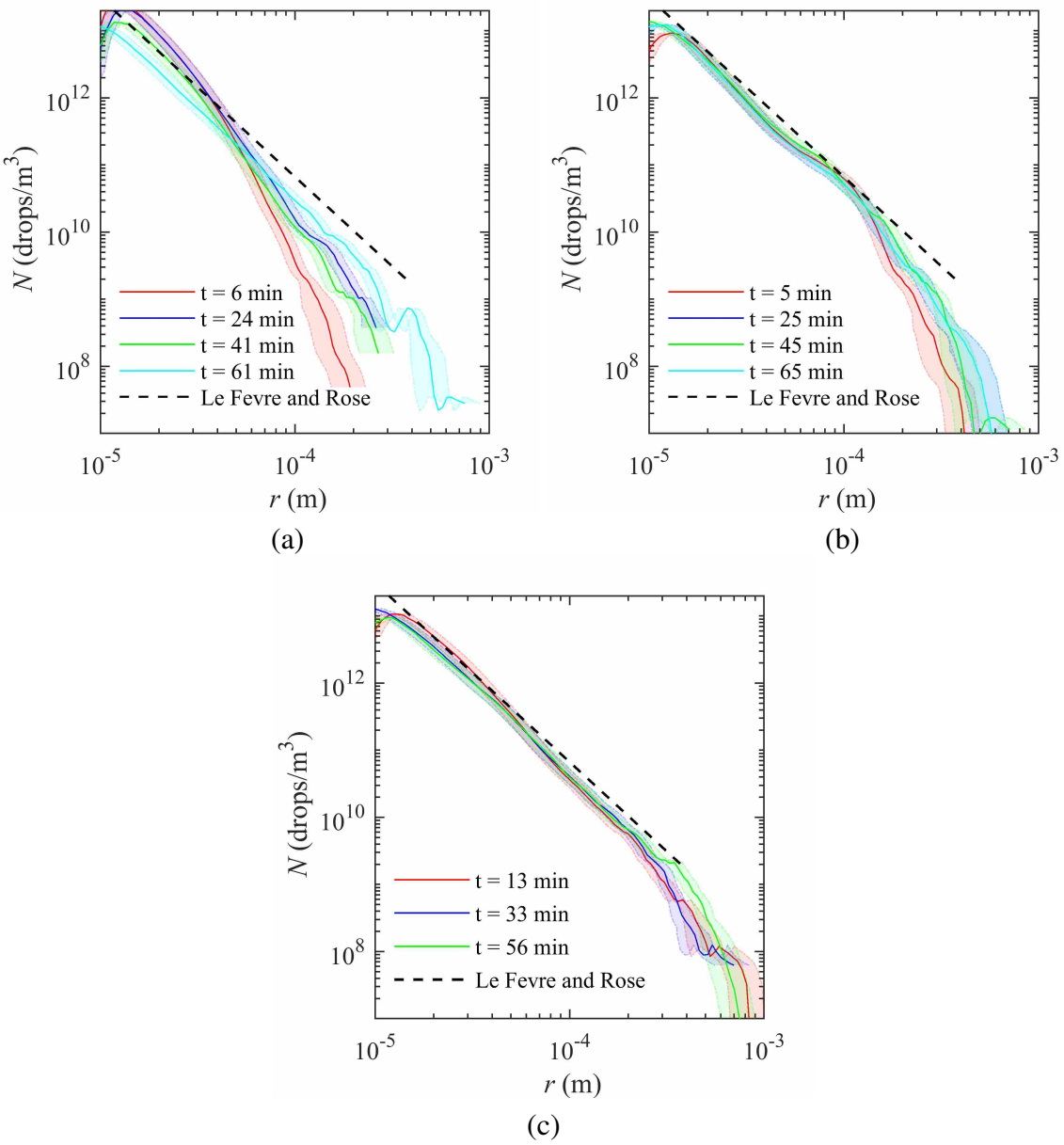

Figure 5.5: Time-averaged drop-size distributions shown at various elapsed times since condensation commences for $T_{sat} - T_c = 2.52$ (a), 4.54 (b), and 5.69 (c) °C. The drop size distribution appears to be weakly dependent on time. The distribution predicted by Le Fevre and Rose is shown for $\hat{r} = 4\times10^{-4}$ m. CICNT diameter = 57 nm. The distribution function is always shown with error bounds associated with the selected size range width using light shading. The drop behavior corresponding to each curve is shown in Figure 5.4. Jumping occurs during condensation for all of the distributions shown with the exception of the distribution corresponding to condensation after 61 minutes when the subcooling was 2.52 °C (in panel a).

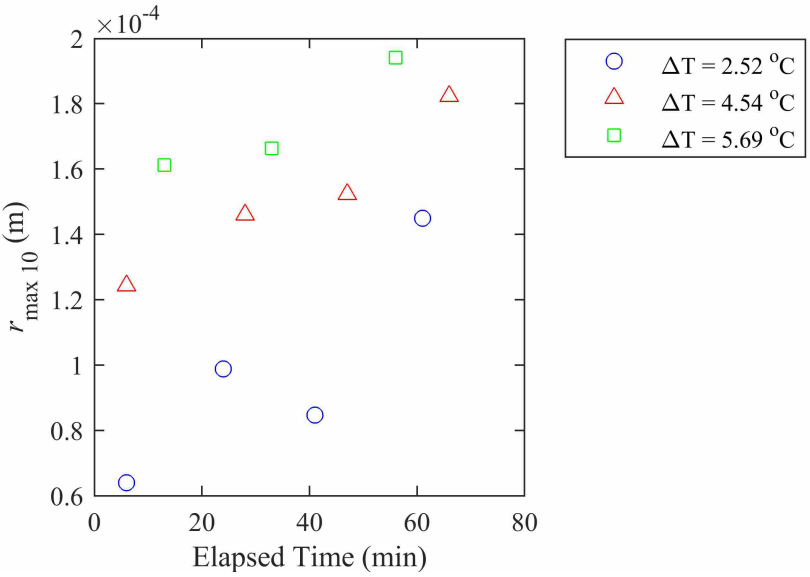

Figure 5.6: Average of the 10 largest drops in each frame of the video, averaged over 3 minutes sections, at different points since condensation commencement for various degrees of subcooling.

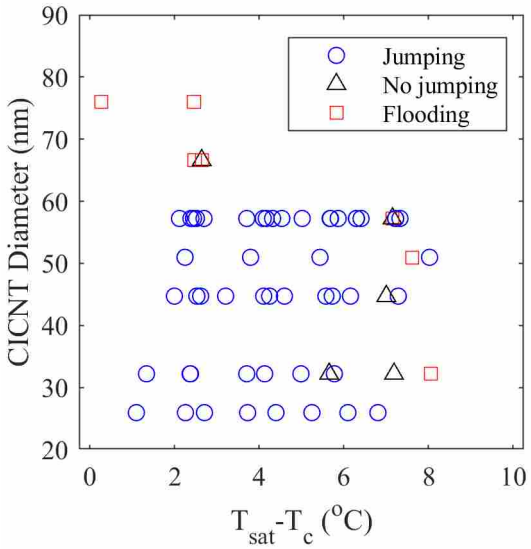

Figure 5.7: Regime map of drop behavior for surfaces as a function of CICNT diameter and surface subcooling. As the subcooling increases, the adhesive force on the drops increases and drop behavior transitions.

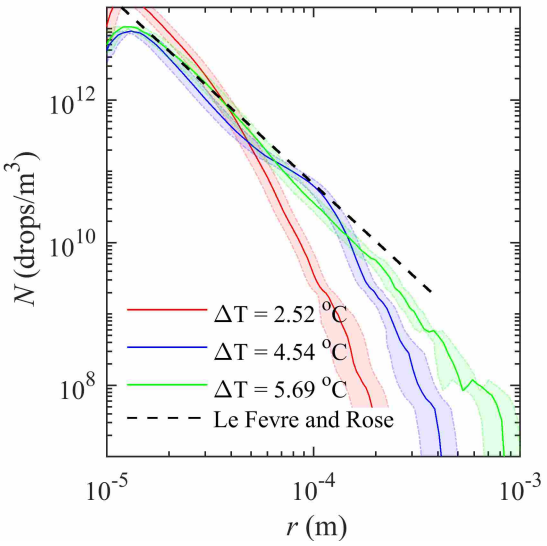

Figure 5.8: Drop-size distributions with different levels of subcooling on a surface with CICNT diameter = 57 nm. As the subcooling increases the drops depart at larger sizes, as illustrated by the radius where the distribution curve diverges away from the Le Fevre and Rose distribution.

CHAPTER 6. MEASURING CONDENSATION HEAT TRANSFER

6.1 Preface

The path to discovering new knowledge, i.e, performing research, is inevitably tortuous, involving idea iteration, abrupt changes in direction, and spectacular failures. The sentiment that trial and error is a prerequisite to the discovery of something new is expressed in a statement often attributed to Thomas Edison about finding 10,000 ways not to make a light bulb. However, in the end, usually only the "successful" outcomes of research are published, despite the fact that knowing 10,000 ways to not make a light bulb may be useful to subsequent researchers. Chapters 2-5 describe successful outcomes. This chapter describes progress made towards the eventual goal of obtaining experimental condensation heat transfer measurements, with dual motivations of providing helpful context to subsequent researchers and describing contributions towards future work.

Upon entering the world of condensation heat transfer I observed a widespread excitement regarding the potential for superhydrophobic surfaces to improve heat transfer rates, but a glaring dearth of experimentally measured heat transfer rates. In retrospect, it seems the lack of heat transfer data stems from the difficulty of the task. The challenge of obtaining experimental heat transfer measurements became apparent after repeated iteration through different experimental set-ups, trying to build a chamber that is suitably impervious to noncondensable gases (NCG) and would permit sufficiently accurate measurement of the saturation and wall temperatures. Though discouraging, I remained doggedly committed to the idea of contributing research that is not only novel or interesting, but that would progress the field of condensation heat transfer. I by-passed further study of several interesting phenomena upon which I stumbled, which would have been significantly easier and likely yielded more conclusive results than those eventually attained. As a result, the research presented in this chapter is far from complete, but represents considerable effort towards an ambitious and relevant goal.

6.2 Introduction

Properly designed superhydrophobic surfaces have been shown to promote the removal of condensate at drop sizes significantly below the capillary length due to the low contact angle hysteresis (indicating high drop mobility) and coalescence-induced jumping of condensate drops. With the removal of condensate drops due to coalescence-induced jumping, the maximum droplet diameter can be reduced by 1 to 3 orders of magnitude [41,43]. The potential for superhydrophobic surfaces to significantly impact condensation heat transfer has prompted a great deal of exploratory research regarding the fundamental behavior of condensing droplets on superhydrophobic surfaces. Several works have quantified metrics which indirectly indicate the relative rate of heat transfer on a surface, such as maximum droplet diameter, coarse drop-size distribution, and individual droplet growth rates [34, 39, 49–55]. Additionally, several models for condensation on superhydrophobic surfaces have been developed [39, 55, 56]. However, only a few works have experimentally measured the heat transfer directly in the absence of NCG [35, 51, 57, 58], and the influence of the micro- and nanostructure geometry on condensation heat transfer is not clear. This chapter presents preliminary efforts to measure the influence of nano- and microstucture geometry on heat transfer performance.

6.3 Methods

The condensation flow loop and experimental procedures, including the precautions regarding NCGs described in chapter 5, apply for the following heat transfer experiments described here.

6.3.1 Two-Tiered Surfaces

In order to study the influence of a microstructure on condensation heat transfer, two-tiered CICNT surfaces are manufactured. Silicon wafers are etched to create micro ribs or pillars using standard photolithographic procedures [87]. Layers of alumina and iron are deposited and CICNTs are grown uniformly on the surface, both on top of the microscale features and in the cavities between the features. The surfaces are then coated with a layer of PTFE to render them superhydrophobic (but vacuum baking, as described in chapter 3 is expected to produce similar

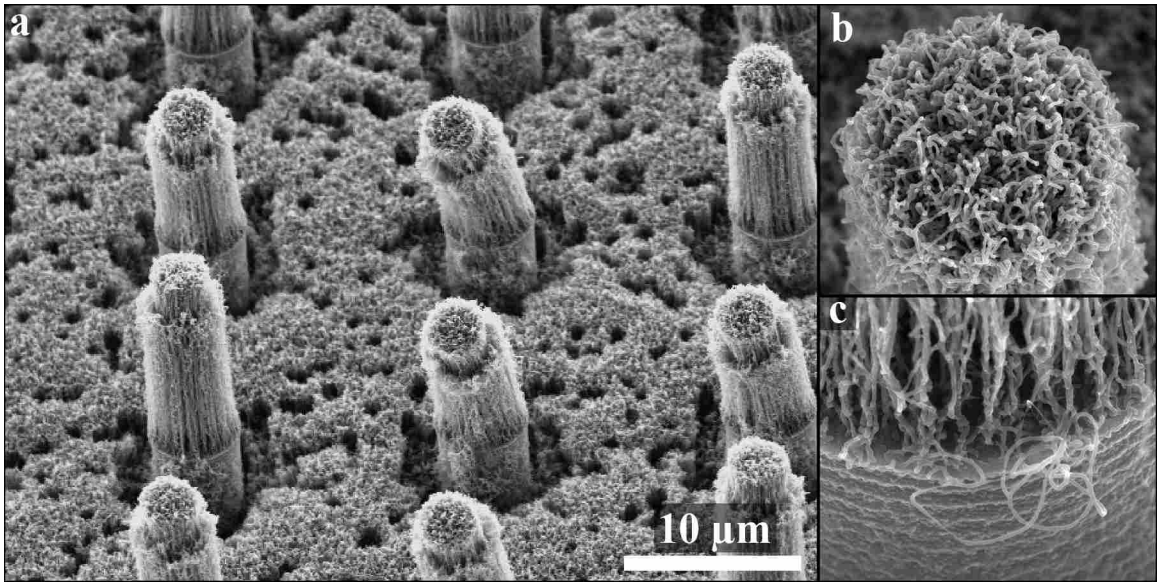

Figure 6.1: CICNTs grown on top of silicon micropillars. The CICNTs grow on top of the silicon microposts and in the cavities between the posts so that surfaces are covered with the nanostructured CICNTs, creating a two-tiered surface. (b) The top of one of the CICNT clusters (c) The top of the etched silicon post on which a cluster of CICNTs grew.

results). SEM images of micropillared surfaces are shown in Figure 6.1. Condensation on the resulting two-tiered surfaces results in coalescence-induced jumping. The surfaces described in chapter 3, where microfeatures are created by growing CICNTs in a pattern, lacked nanostructures in the space between the features, rendering them ineffective for promoting dropwise condensation.

6.3.2 Copper Oxide Surfaces

In addition to the CICNT surfaces described in chapter 3, superhydrophobic copper oxide surfaces are manufactured following the procedures similar to that described in the literature, but with a different functionalization process [32,91,154]. A complete description of the procedure can be found in Appendix D. Briefly, copper surfaces are polished following the procedure described by Nam and Ju [167], then double-soaked in an ultrasonic acetone bath for 20 minutes, rinsed with ethanol, isopropyl alcohol, and deionized (DI) water 5 times, dried with N_2, and immersed in a 2.0 M solution of HCl for 20 minutes to remove the native oxide film on the surface. The surfaces are then triple-rinsed with DI water and dried with N_2. The nanostructure is created by immersing the substrate in a solution of $NaClO_2$, NaOH, $Na_3PO_4{\cdot}12H_2O$, and DI water (3.75:5:10:100 wt.

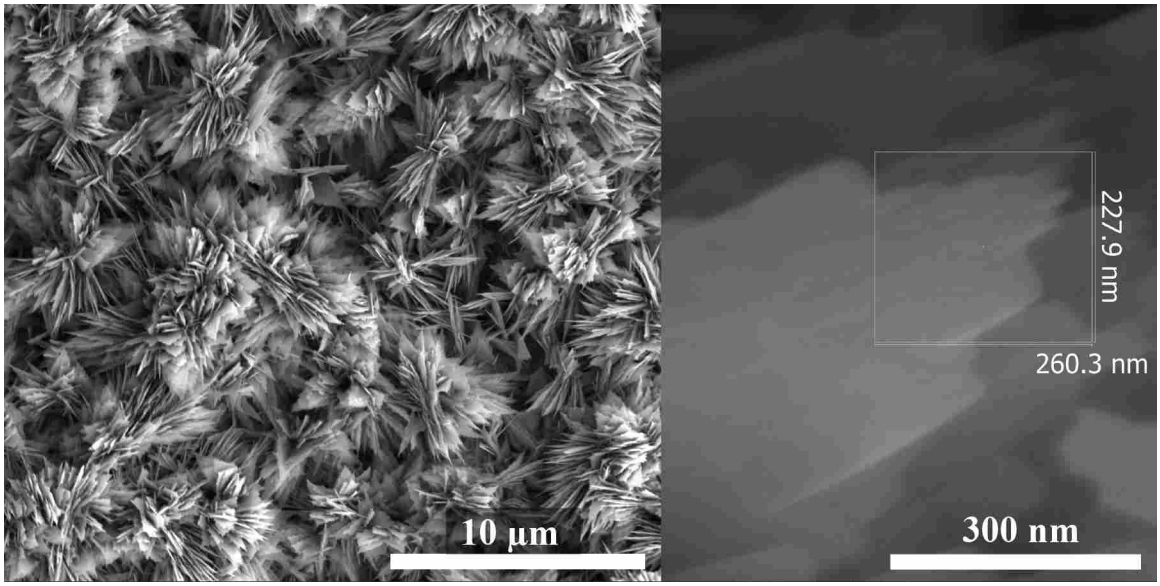

Figure 6.2: SEM images of the knife-like copper oxide structures.

%) held at 96 $\pm$ 3 °C, forming a knife-like copper oxide film as shown in Figure 6.2. The surface is rinsed 5 times in DI water and dried with N_2. The surface is functionalized by adding two layers of PTFE, applied via spin coating [87]. The resulting surfaces had an advancing contact angle of 157° and hysteresis of 2°. Surfaces are also functionalized using an immersion coating of Glaco [168], which also resulted in superhydrophobic surfaces. Condensation on the copper oxide surfaces resulted in coalescence-induced jumping.

6.3.3 Heat Flux Measurements

Four independent methods are used to measure the heat flux, motivated by concern that initial heat transfer rates measured on hydrophilic control copper surfaces are lower than that in the literature [7].

- The volume of condensate collected at the bottom of the vacuum chamber is measured. Following a test, the condensate is accessed through the port leading to the Erlenmeyer flask between the needle valve and the chamber with syringe attached to a piece of flexible PVC tubing with a copper wire in the center. The heat transfer rate is calculated from the amount

of energy required to condense the amount of liquid collected,

$$q" = \frac{\rho V h_{fg}}{t A_{\mathrm{c}}}, \tag{6.1}$$

where t is the length of time of the test, A_{c} is the condensing area, and V is the volume of collected condensate.

- A heat flux sensor (FluxTeq) is placed between the heat exchanger and copper disk that interfaced with the condensation chamber.

- The temperature gradient in the copper disk interfacing with the chamber is measured. Four thermocouples are embedded in small (#55 drill) holes. The copper disk is the same size as the condensing surface so that the heat transfer is predominantly one-dimensional. The heat flux through the copper block is calculated as

$$q_{\mathrm{g}}" = -\mathrm{k} A_{\mathrm{c}} \frac{\mathrm{d}T}{\mathrm{d}x}. \tag{6.2}$$

  The temperature gradient is obtained by fitting a line to the temperature measured by the four thermocouples.

- The change in the heat exchanger coolant temperature is measured. Thermocouples measure the water temperature immediately before entering and after exiting the heat exchanger, and a flow meter (Omega FLR1009-D) measures the volumetic coolant flow rate. The heat flux is calculated as

$$q_{\Delta \mathrm{T}}" = \frac{\dot{m} c_p (T_{\mathrm{HXout}} - T_{\mathrm{HXin}})}{A_{\mathrm{c}}}, \tag{6.3}$$

  where T_{HXin} and T_{HXout} is the temperature entering and exiting the heat exchanger.

Agreement between all four methods is generally obtained (within approximately 50%). Uncertainty associated with the condensate collection and heat flux sensor measurements are large so only the heat transfer rate measured from the copper block temperature gradient (q_{g}") and change in coolant temperature ($q_{\Delta \mathrm{T}}$" methods are used for each test. The agreement between these two methods is generally within ± 30 % when the heat flux is larger than 10,000 W/m^2, as shown in Figure 6.3a. However, the measurements rapidly diverged for low heat fluxes. The poor agreement

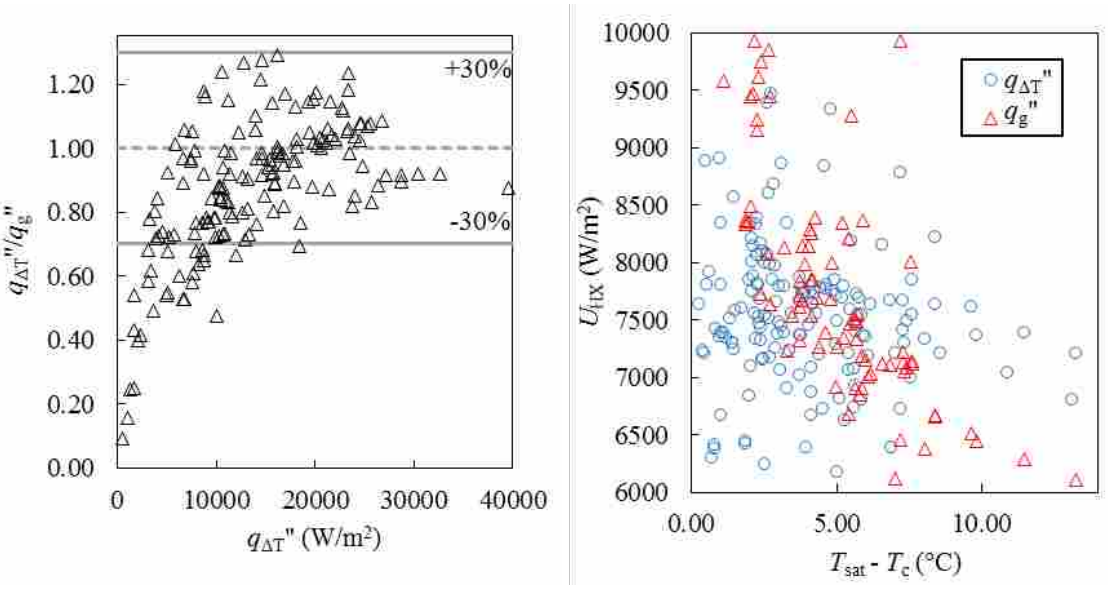

Figure 6.3: (a) Ratio between heat transfer measurements made using the change in coolant temperature and the temperature gradient in the copper block. (b) Heat transfer coefficient between the heat exchanger and copper block obtained using the change in coolant temperature and copper block temperature gradient approaches for measuring the heat transfer rate.

is assumed to stem from the uncertainty associated with the thermocouple position and temperature measurement.

The heat transfer coefficient between the heat exchanger and copper block, U_{HX} is calculated using both approaches and is shown in Figure 6.3b.

$$U_{\mathrm{HX}} = \frac{q"}{T_{\mathrm{HXin}} - T_{\mathrm{c}}}, \tag{6.4}$$

The heat transfer coefficient is not expected to change with subcooling. The fact that the heat transfer coefficient changes significantly with subcooling when calculated using the copper block temperature gradient suggests that the change in coolant approach for measuring heat transfer is more accurate at low heat fluxes.

6.3.4 Saturation Temperature Measurement

Heterogeneous condensation is driven by the temperature difference between the saturated vapor temperature and the surface temperature; it is this temperature difference that is used

to calculate a heat transfer coefficient, h, describing the rate of condensation. One reason condensation heat transfer measurements are so challenging is the small temperature difference between the surface and vapor, requiring high precision for accurate results. Experiments are performed with saturation temperatures close to ambient temperature to avoid the need to heat every part of the setup where condensation is undesirable, such as the window through which the condensing surface is observed. However, even with nominally ambient conditions, the vapor temperature is always slightly lower than the surrounding temperature, and a thermocouple placed in the vapor is subject to radiation from the surrounding chamber walls, the cooled condensing surface, and the ring light used to illuminate the surface. A UV filter (Thorlabs FGS600) placed between the ring light and the chamber attenuated the majority of the radiative energy from the light, but error introduced from radiation from other sources is still significant, as evidenced by the disagreement between the saturation pressure measured by the measured vapor pressure and the corresponding saturation temperature measured by the thermocouple. However, after allowing the vapor to equilibrate with the chamber, the agreement between the saturation temperature corresponding to the measured saturation pressure is within 0.05 °C. Accordingly, the saturation temperature is obtained from the measured saturation pressure and the thermocouple in the vapor is used to ensure saturated conditions.

6.3.5 Surface Temperature Measurement

An original objective of this research is to explore how varying the nano- and microstuctures influenced heat transfer performance. Microstructures are created by etching silicon wafers, while the nanostructures are created by growing CICNTs on Fe coated silion wafers. However, the wafer thickness ($\sim$0.5 mm) precludes thermocouple placement inside the wafer, making it difficult to measure the surface temperature. For high heat fluxes which occur during condensation and low temperature difference between the vapor and surface, even small contact resistance between the copper block and the wafer is significant. Additionally, since most thermal greases and pastes have vapor pressures higher than 3 Pa, they could not be used to minimize the contact resistance, necessitating the use of vacuum grease as a substitute thermal interface material.

It is also difficult to accurately quantify the contact resistance. The condensing surface temperature could not be measured using an IR camera during condensation since the conden-

sate obscured the view of the surface. Surface temperature measured by a thermocouple adhered to the condensing surface is also affected by the temperature of the condensate and introduced another contact resistance between the surface and thermocouple. If the contact resistance were measured by heating one side of the interface and cooling the other with forced convection, the chamber would be required to be at atmospheric pressure; in this case, the contact resistance may not behave the same when the junction is exposed to ambient temperature saturation pressure (approximately 2.7 kPa). As described in chapter 3, CICNTs can be grown on stainless steel surfaces, and a thermocouple could be embedded in a stainless steel surface. This was attempted, but the uncertainty introduced by the size of a hole (#55 drill) for the thermocouple is unviably large, since the thermal conductivity of stainless steel is small relative to copper. Accordingly, superhydrophobic copper oxide surfaces are manufactured which allow surface temperature measurement by placing a thermocouple in a hole drilled through the side. Unfortunately, a method to control the micro- and nanostructure of copper oxide surfaces was not obtained.

6.3.6 Use of Computer Vision

Minimizing the uncertainty associated with traditional heat flux measurement methods (heat flux sensors, thermocouple arrays, change in coolant temperature, condensate collection etc.) to an acceptably low level can be challenging, and generally provide little to no spatial information and may have significant time delays. In contrast, optical microscopes provide extremely detailed spatial information with relatively little time delay. Accordingly, computer vision analysis of optical microscope videos to obtain heat transfer measurements offers a promising alternative and was successfully used by Ölçeroğlu *et al.* [52]. A MATLAB code was written, capable of autonomously tracking thousands of individual drops. The code successfully tracks drops when the nucleation density is extremely low and the space between drops is large, as occurs during condensation in ambient conditions with large concentrations of NCG. The computer vision code estimated the heat transfer rate during condensation on a two-tiered superhydrophobic surface experiencing coalescence-induced jumping by tracking the size of all departing drops [169]. During steady state condensation, the rate of condensate production can be estimated from the rate of condensate departure, and the heat transfer rate is calculated using Equation 6.1. The code used a combination of the contrast in intensity between drops and surroundings and the Hough transform

to distinguish the drops. On the first frame of the video, the location and radius of each of the drops of condensate is detected. The code then tracks the growth of each droplet in the first frame through time until the drop coalesces with a neighboring drop or the video ends. Additional drops that nucleate in subsequent frames are detected and similarly tracked through time. This approach for measuring condensation heat transfer works well in the presence of NCG, but as described in chapter 1, heat transfer measurements obtained in the presence on NCG are not useful for comparison accross experimental setups since the heat transfer rate is limited by the vapor diffusion rate to the surface.

In the absence of NCG and with a reasonable degree of subcooling, the nucleation density is so high that a significant number of small drops are hidden in the shadow of large drops when the contact angle is high, rendering the task of tracking every drop impossible. However, on a surface where all drops eventually depart via coalescence-induced jumping, if it were possible to track every departure event one could still obtain an estimate of the heat transfer rate; this could be accomplished by measuring the condensate departure rate, equivalent to the condensate production rate during steady state condensation. Unfortunately, the high nucleation density renders the task of tracking every departure difficult. The code uses the contrast between the substrate and drops to track individual drops; when drops cover every part of the condensing surface they are difficult to distinguish. Due to these challenge of measuring drop departure with high nucleation density, computer vision was not used to obtain heat transfer measurements. However, a different approach to drop tracking, described in chapter 5, allows for drop tracking when the contrast between drops and the background is low, and could potentially be modified to detect drop departure, enabling the estimation of the heat transfer rate from video.

6.4 Preliminary Results

The heat flux measured during condensation on nanostructured CICNT surfaces using the change in coolant temperature is shown in Figure 6.4. The heat transfer rate increases with increasing subcooling, as expected. The overall heat transfer coefficient, U, is calculated from the measured heat transfer rate and the difference between the vapor temperature and the surface temperature (represented by the thermocouple closest to the surface of copper block). Therefore, the overall heat transfer coefficient includes the condensation heat transfer coefficient and the follow-

ing thermal resistances: (1) the CICNT nanostructure, (2) Fe and alumina coated-silicon wafer, (3) copper between the thermocouple placement and the surface, and (4) the contact resistance. However, of these thermal resistances, all are estimated to have a negligible impact on U except the contact resistance. The experimentally observed overall heat transfer coefficient generally decreases with increasing subcooling. Since the contact resistance should remain constant with increased subcooling, the decrease in overall heat transfer coefficient indicates that the condensation heat transfer coefficient is decreasing, as observed by other investigators [51, 57, 58], but in contrast to that predicted by classic dropwise condensation heat transfer predictions [7].

As described in chapter 5, the change in vacuum chamber pressure is measured after allowing the chamber to pump down for at least 24 hours, but before introducing water vapor. However, the longer the chamber is under vacuum, the lower the rate of pressure rise, indicating that the increase in pressure is likely due to outgassing. The influence of the initial rate of pressure rise on heat transfer performance is shown in Figures 6.4a and b. Despite careful efforts to minimize the influence of NCG, it appears that performance may be slightly decreased when initial rate of pressure rise is greater than 0.15 Pa/min. The concentration of NCG is conservatively estimated by multiplying the outgassing rate by length of time since the introductino of water vapor, and adding it to the initial vacuum pressure (3 Pa) and dividing by the water vapor pressure ($\sim$2.7 kPa). The estimate is conservative because the pressure rise is non-linear and the rate of pressure rise decreases over time. Furthermore, it is expected that the introduction of water vapor would significantly reduce the rate of pressure rise. For an hour long test with an initial rate of pressure rise 0.15 Pa/min, the NCG concentration would be 0.4%, less than the standard of 0.6% met by all test presented in this chapter. Therefore, it is recommended that future tests be conducted with a lower NCG concentration standard than 0.6%. Ideally, the NCG concentration would be less than 0.25%, as described in the Supporting Information of Miljkovic *et al.* [35].

The length of time since condensation commencement on the heat transfer rate (Figure 6.4c and d) appears to have little influence. The condensation rate appears slightly higher with increased condensation time, contrary to what might be expected if the NCG concentration were increasing with time. The apparent increase in heat transfer performance with time may be a result of larger drops on the surface, or more water within the nanostructure, leading to a higher

percentage of partially wetting drops, which are expected to have a higher heat transfer rate than suspended drops [39].

The CICNT diameter ranged from 25 to 125 nm; surfaces with CICNT diameter larger than 60 nm appeared to have diminished heat transfer performance relative to those with smaller diameters. However, given the fact that these surfaces all flooded the decrease in performance is expected.

6.5 Conclusions and Future Work

Heat transfer measurements on plain CICNT surfaces are obtained, with diminished heat transfer performance for surfaces which experienced flooding. The heat transfer measurements included the contact resistance between the surface and cooled copper block, confounding isolatio of the condensation heat transfer coefficient. A process for manufacturing copper oxide superhydrophobic surfaces, which allows the measurement of the surface temperature, is described. However, heat transfer measurements have not yet been obtained on these surfaces. Since the copper oxide surfaces do not offer control over the micro- and nanostructure, the objective of exploring micro- and nanostructured surfaces cannot be realized. However, heat transfer measurements could be compared with the drop behavior statistics obtained from video/computer vision analysis (drop-size distribution, drop-departure-size distribution, percent of coalescence events resulting in departure, maximum drop size, etc.). A process for manufacturing two-tiered superhydrophobic surfaces is described offering control of the nanostructure and microstructure. Since the surface is created using Si wafers, measurement of the surface temperature is not possible; however, comparative heat transfer measurements (as in this chapter), could be obtained, providing information regarding the relative influence of two-tiered geometry (e.g. microstructure height, pitch, and shape; nanostructure diameter and height) on heat transfer performance.

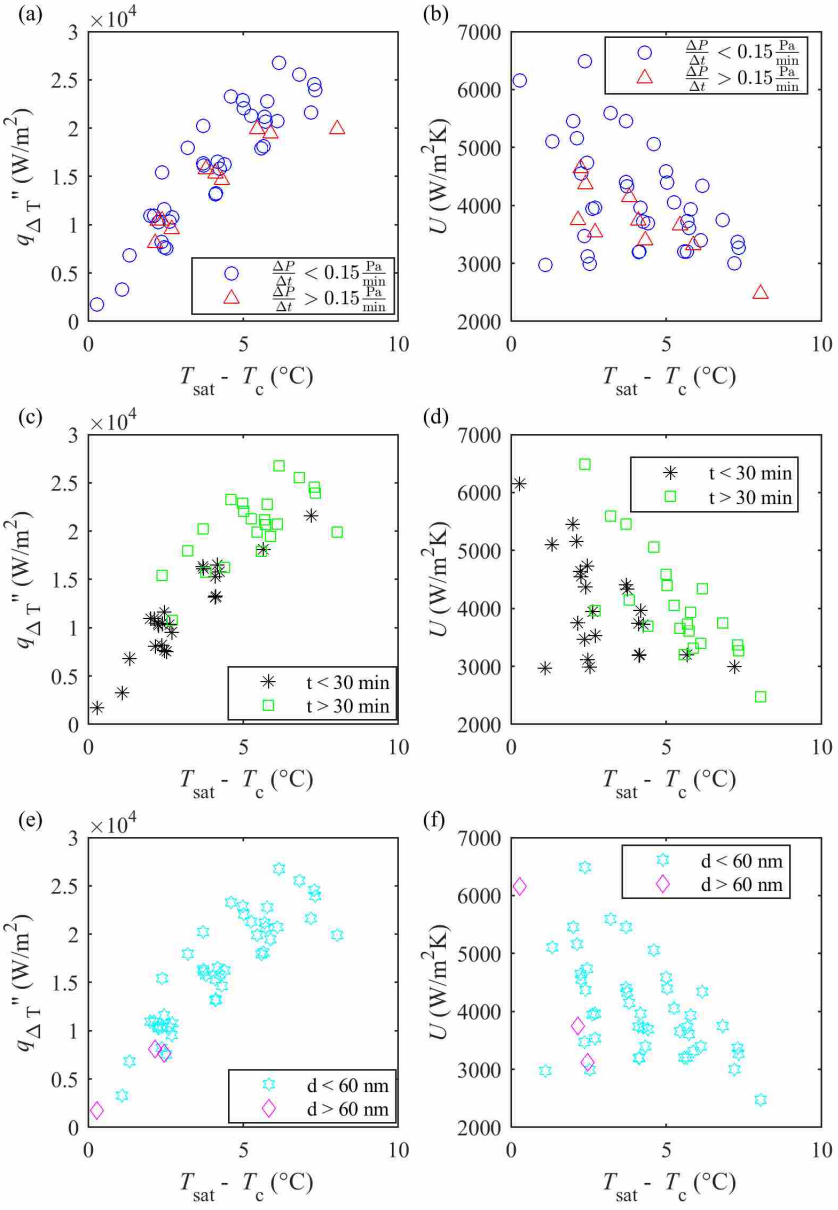

Figure 6.4: (a,c,e) Condensation heat flux, q", measured using the change in heat exchanger coolant temperature on CICNT coated surfaces and (b,d,f) the total heat transfer coefficient, U as a function of subcooling temperature. This overall heat transfer coefficient includes the condensation heat transfer coefficient and contact resistance. The markers in (a,b) indicate tests where the rate of pressure rise (likely due to outgassing) is less than 0.15 Pa/min (blue circles) or greater than 0.15 Pa/min (red triangles). The markers in (c,d) indicate data taken less than (blue circles) or more than (red triangles) 30 minutes since the beginning of condensation. The markers in (e,f) indicate surfaces with CICNT diameter less than (blue circles) or greater than (red triangles) 60 nm.

CHAPTER 7. CONCLUSIONS

The present work explores various aspects related to the influence of a superhydrophobic surface on two-phase heat and mass transport. Each chapter offers insights relevant to the objective of using superhyrdophobic surfaces to achieve increased condensation heat transfer. Chapter 2 reports experimentally measured drag reduction caused by the presence of a superhydrophobic surface in adiabatic two-phase microchannel flow. Chapter 3 describes a new approach for manufacturing configurable superhydrophobic surfaces suitable for condensation. Chapter 4 presents a numerical approach to obtain detailed condensate drop-size distributions and reports how various parameters influence this distribution and overall heat transfer rate. Chapter 5 details experimental results suggesting that increased subcooling leads to increased adhesive force during condensation and describes how increased subcooling influences the drop-size distribution. Chapter 6 describes preliminary efforts to measure the rate of condensation heat transfer. Key conclusions from each chapter are summarized in the following sections and are accompanied by a description of future work. The dissertation concludes with a discussion of conclusions based on the work as a whole.

7.1 Two-Phase Flow Pressure Drop in Superhydrophobic Channels (chapter 2)

The presence of a superhydrophobic surface can alter the mass transport in two-phase flows, such as commonly occur in industrial boiling and condensation systems. The change in mass transport should be considered in concert with the thermal transport. For a parallel-plate channel with a single superhydrophobic wall, an average reduction of about 10% in the square root of the two-phase multiplier (ϕ) relative to a classical channel was measured. This corresponds to a reduction in drag of 10% in addition to that observed for single-phase liquid flow in a channel with a superhydrophobic boundary for the same conditions. The ratio of the reduction in drag for a superhydrophobic surface relative to a hydrophilic surface decreases with increasing vapor qualities, indicating that the effect of the superhydrophobicity is greater with increasing vapor

fraction. When conducting and reporting experiments involving two-phase flows in micro- and mini-channels, the wettability of the surfaces should be considered and reported. Recognition of the influence of wettability on mass transport is crucial since wettability engineering is considered as a means to increase thermal transport rates.

7.2 Superhydrophobic, Carbon-Infiltrated Carbon Nanotubes on Si and 316L Stainless Steel with Tunable Geometry (chapter 3)

A nanostructure is necessary for the formation of condensation in a wetting state that may lead to increased heat transfer rates; however the influence of nanostructure geometry (cavity fraction, height, pitch, etc.) on drop behavior and heat transfer rates are not well understood. A method for creating superhydrophobic surfaces offering control over the nanostructure is described. Carbon nanotube surfaces can be enhanced by infiltrating with amorphous carbon to improve mechanical durability, increase resistance to shear failure, and control nanoscale feature size. CICNT structures can be rendered superhydrophobic for a range of infiltration amounts with negligible change in superhydrophobicity, as determined by the static contact angle, contact angle hysteresis, and sliding angle. In general, longer infiltration times result in carbon nanotubes with larger diameters. The rate of infiltration is somewhat dependent on the patterning of carbon nanotubes, with sparser microscale patterning leading to higher rates of infiltration. Superhydrophobicity is invariant to CICNT diameter within the range tested in the present work.

Furthermore, scalability and durability are both significant impediments to practical use of superhydrophobic surfaces. Chapter 3 demonstrates that CICNTs grown directly on stainless steel surfaces, when subjected to vacuum pyrolysis, display the same superhydrophobic properties as CICNT surfaces grown from Fe deposited on alumina. Surfaces created with direct growth of CICNTs on stainless steel are even more robust than CICNTs grown on Fe deposited on alumina, as indicated by the scratch tests presented in this work. The ability to grow CICNTs directly on the stainless steel without the need for Fe deposition reduces fabrication complexity and increases potential scalability of these surfaces.

7.3 Drop-Size Distribution During Dropwise Condensation from Simulation and Implications for Heat Transfer Modeling (chapter 4)

Knowledge of condensate drop-size distribution is required to model overall condensation heat transfer rates. A framework to obtain drop-size distribution functions during dropwise condensation on vertical surfaces was developed and used to explore the influence of the assumptions made in previous drop-size distribution models. With the lack of available experimental data for distributions in this size range, the present work represents the first attempt to evaluate the accuracy of the population balance modeling approach and describes when and why population balance modeling is not a suitable method for obtaining drop-size distributions. The simulation includes the possibility for coalescence-induced jumping, where all drops above a specified threshold radius depart upon coalescence. Parameters dependent on surface structure and chemistry, including contact angle (θ), maximum drop size ($r_{\max}$), and minimum jumping radius (r_{j}), are specified in the simulation, so that each parameter may be independently varied and the appropriate combination selected to model heat transfer on a given surface.

The influence of nucleation site distribution approach, nucleation site density, maximum drop size, and contact angle on the distribution function are explored. The approach for distributing the nucleation sites influences both the distribution curve and the overall heat transfer rate. For the parameters explored in the present simulation, the random nucleation scheme resulted in heat transfer rates on the order of 25% larger than those predicted with the preferential nucleation scheme. Realistic nucleation behavior is likely a combination of the two nucleation approaches, and may be used to bracket realistic behavior. Nucleation site density N_{s} significantly influences the size at which drops begin to coalesce and size at which the distribution function approaches the empirical Le Fevre and Rose correlation [129, 130]. In addition to presentation of an approach for modeling drop-size distributions, the present work offers insight into factors which are important when modeling condensation heat transfer.

The results from the simulation suggest that removing large drops may not necessarily lead to increased overall heat transfer rates since large drops do not cover a significant portion of the surface when the contact angle is large. Birbarah and Miljkovic also showed that minimizing drop departure size is not always beneficial for heat transfer since smaller departed drops may return to the surface due to the vapor flux [86]. An individual drop heat transfer model from Xu *et al.*

suggests that larger drops may have higher heat transfer rates than originally anticipated when internal drop convection is considered [156]. Mendoza *et al.* demonstrated that non-continuum and interface curvature become increasingly important with decreasing drop-size. They suggest the achievable heat transfer rate reaches a peak beyond which decreasing the mean drop size will decrease heat transfer. The results from the present simulation, Birbarah and Miljkovic, Xu *et al.*, and Mendoza *et al.* suggest four completely different reasons that minimizing drop size does not always lead to increased heat transfer rates. An ideal size for drop departure may exist which is significantly larger than the minimum drop-departure size achievable, in contrast to conventional wisdom.

7.4 Drop-Behavior Transition and Drop-Size Distribution During Dropwise Condensation on Superhydrophobic Surfaces (chapter 5)

Increasing the degree of subcooling causes a transition in drop behavior from coalescence-induced jumping to dropwise non-jumping to flooding. As the degree of subcooling increases, the size of drops on the surface increases since fewer coalescence events result in departure. The resulting shift in the distribution function is measured experimentally, and is important to understand for heat transfer modeling. The gradual departure from the Le Fevre and Rose distribution function is similar in shape to that predicted in chapter 4. Understanding the drop-size distribution in the departure region is important since drops in this size range are expected to contribute significantly to the overall heat transfer rate. Length of time condensation occurs on a surface and nanostructure size are also shown to affect the transition in drop behavior and drop-size distribution. The change in behavior and drop-size distribution result can be explained by an increase in adhesive force.

7.5 Measuring Condensation Heat Transfer (chapter 6)

An experimental setup capable of measuring and visualizing condensation heat transfer at low concentrations of non-condensable gases was built. Two types of superhydrophobic surfaces capable of promoting coalescence-induced jumping were fabricated: one which offered control over both the micro and nanostructure geometry and another which allowed for the measurement of the surface temperature with an embedded thermocouple. Challenges obtaining the surface

temperature prevented measurement of the condensation heat transfer coefficient, but comparative heat transfer measurements indicate that nanostucture influences the overall heat transfer rate when the flooding occurs.

7.6 Future Work

The present work addresses several facets of improving condensation heat transfer. Future work in areas related specifically to the present work is now discussed. The work presented in chapter 4 elucidated the change in drag reduction caused by a single superhydrophobic surface in a parallel-plate configuration for a specific range of operating conditions (superficial gas and liquid Reynolds numbers ranging from 22-215 and 55-220). Future work should include investigation of additional relevant channel geometries where all the surfaces are superhydrophobic.

Durability is one practical impediment to the widespread use of superhydrophobic surfaces. Chapter 3 described creation of stainless steel superhydrophobic surfaces that performed promisingly in initial durability testing. Additional investigation of the durability of the stainless steel surfaces should be undertaken to determine whether they could be used in practical applications.

7.6.1 Drop-Size Distribution During Dropwise Condensation from Simulation and Implications for Heat Transfer Modeling (chapter 4)

The work presented in chapter 4 included an approach for drop-size distribution modeling, and indicated the importance of using a model which incorporates variable drop departure size and coalescence at sizes where direct-condensation dominates growth. The work demonstrated that several factors influence drop-size distribution and overall heat transfer rate. Future work can be divided into four categories: improvements to the current computational approach, further exploration of the influence of significant factors, experimental validation, and additional understanding required for the development of a comprehensive condensation heat transfer model.

Computational Approach Improvements

- Implementation of periodic boundary conditions — the simulation presently only considers drops which are within the computational domain. However, in reality, drops located near

the edge would coalesce with drops growing outside of the domain. In the present work, the size of the largest drop was less than half the size of the computational domain so that the number of drops which were unaffected by boundary condition (those located towards the middle of the domain) was large relative to the number of drops which were affected by the boundary condition (those located towards the edge of the domain). Variation in results with domain size was shown to be within uncertainty limits. However, the simulation could be adjusted by implementing periodic boundary conditions, where drops overlapping with the boundary would be considered at the opposite boundary. Drops located near the edge of the domain would grow by coalescence with drops located on the opposite edge of the domain. For example, drops near the left edge could be allowed to coalesce with imaginary drops whose location mirrored drops located near the right edge. The resulting simulation would be more accurate and could allow the use of smaller domain sizes relative to the maximum drop size.

- Improve computational speed — the computational cost to run the simulation increases with domain size and nucleation density. The simulation is written in MATLAB, which is an interpreted language; use of a compiled language such as C++ may result in significant improvement in computational cost. Similarly, restructuring the simulation to allow for parallel processing would allow the use of supercomputers, which could significantly decrease the real-time cost.

- Determine the period for drop sweeping — when r_{max} is large, drops must grow several orders of magnitude from nucleation to departure, which is computationally expensive. However, since the distribution function is well established for large drop sizes, the simulation could be used to determine the distribution function for drops smaller than r_e. Drops larger than r_e influence the distribution of smaller drops when they shed and sweep, removing all drops in their path. If the sweeping period, τ, could be determined, the simulation would only need to consider the growth and coalescence of drops smaller than r_e, permitting use of a smaller domain size and significantly reducing the required computational time. The work done by Weisensee *et al.* could guide efforts to determine τ [170].

- Incorporate improved individual drop heat transfer models — the heat transfer model used in the simulation influences both the distribution and the overall heat transfer rate, particularly for low contact angles. As more accurate models are developed (such as that of Xu *et al.* [156]) and combined with the results of the present work, the accuracy of the distribution function and prediction of the overall heat transfer rate may improve.

- Consider cascading and chain coalescence — the present simulation does not address cascading coalescence in a single time step and only considers secondary and tertiary drops in chain coalescence. Addressing cascading coalescence during a single time step and considering more drops during chain coalescence could improve the accuracy of the simulation when using larger time steps.

Additional Exploration of Significant Parameters

- Nucleation density — the present work described how the individual drop heat transfer model, contact angle, maximum drop size, and nucleation site distribution approach influenced the drop-size distribution and overall heat transfer rates at a single nucleation density, $N_s = 1 \times 10^{11}$ drops/m^2. Different nucleation densities, which would result in a different average coalescence size, could result in different trends.

- Coalescence-induced departure models — in the present work, whether or not coalescence will result in drop departure is determined based on a specified minimum jumping size; however, the structure of the simulation allows for the use of more sophisticated models for drop jumping. For example, a model for jumping based on an energy balance between the adhesive force of the drops and energy released upon coalescence could be evaluated for each coalescence event, enabling the inclusion of factors such as surface feature length scale, drop wetting state, relative size mismatch, and number of drops involved in a coalescence event. The model could be based on work by previous investigators, some of whom have used an adhesive force and surface energy balance to determine when coalescing drops will jump [36, 42, 91, 91, 93, 171–173]. As demonstrated in Figures 4.14 and 5.8, when coalescence-induced jumping results in drop removal, the drop-size distribution

departs from the Le Fevre and Rose function. The region from the point which the distribution begins to diverge to the maximum drop size may be termed the departure region. The drop-size distribution predicted by the simulation (Figure 4.14) is much steeper (diverges more over a smaller radius range) than the measured drop-size distribution (Figure 5.8) in the departure region. This difference likely arises from the fact that in the simulation all coalescence events involving drops larger than r_j depart via coalescence-induced jumping. In reality, not all coalescence events with drops larger than the minimum jumping size result in departure, which produces a more gradual divergence from the Le Fevre and Rose drop-size distribution. Therefore, it is expected that using a more refined model to predict coalescence-induced jumping in the simulation would result in a drop-size distribution which diverges from the Le Fevre and Rose distribution more gradually in the departure region, as measured experimentally. An estimate of the expected improvement in accuracy could be obtained by perturbing the drop-size distribution in the departure region until it matched the experimentally measured drop-size distribution.

- Vapor flux — drops which have departed by coalescence-induced jumping are not influenced by vapor flux and do not return to the surface in the present simulation. However, modeling by Birbarah and Miljkovic suggests the vapor flux toward the condensing surface can cause departed drops to return to the surface even when the surface is oriented vertically [86]. Considering coalescence-induced departed droplet return to the surface would influence the drop-size distribution, could be included in the simulation, and would be instructive when considering the drop departure size which maximizes heat transfer.

- Non-constant contact angle growth — the present work is valid for smooth hydrophobic or nanostructured superhydrophobic surfaces, where the assumption of constant contact angle growth is reasonable. However, the influence of non-constant contact angle growth with a two-tiered micro- and nanostructured surface could be explored following an approach similar to [17].

- Surface microstructure — in addition to the use of a non-constant contact angle model, incorporation of a microstructure will require consideration of different wetting states (suspended and partially wetting) and a mechanism to treat the thermal resistance in the microstructure.

Variable contact angle, wetting state, and structure thermal resistance influence individual drop growth rate [17].

- Transient response to coalescence — the present work treats coalescence as an instantaneous rather than finite event. However, following coalescence, a drop that remains on the surface experiences a decaying oscillation and takes time to recover a quasi-steady temperature profile. Incorporation of the the drop's transient response, using the modeling of Adhikari *et al.* [174], may influence the steady state drop-size distribution function and heat transfer rate.

- Saturation pressure — the condensation interfacial heat transfer coefficient, h_i, is sensitive to atmospheric pressure, and reports in the literature vary whether it is significant.

- Non-uniform substrate temperature — the present simulation assumes a uniform substrate surface temperature, regardless of the size and spatial location of all drops. For a copper surface, this is a reasonable assumption, since the constriction resistance due to the presence of a drop on the surface will be nearly negligible. However, many superhydrophobic surfaces have a polymer or silane coating that may have non-negligible constriction resistance, and investigation of the influence of the coating could be instructive. Consideration of the coating influence could be as simple as the addition of a thermal resistance in the individual drop heat transfer model [17, 56], or as involved as considering a non-uniform substrate surface temperature which varies with the presence of drops.

- Non-uniform vapor temperature — in the present simulation, drops grow independently of their spatial location to their neighbors, i.e. the vapor temperature is considered to be uniform throughout the simulation, and the vapor is always saturated. However, if even a small concentration of non-condensable gases were present, a temperature and concentration gradient would develop in the vapor, influencing the rate of vapor absorption by the condensing drops.

Experimental Validation

Experimental drop-size distribution measurements have been limited to drop sizes where the Le Fevere and Rose distribution is appropriate, but light microscopes (such as Keyence VH-Z100R, VH-Z500T, VH-ZST) currently exit that could potentially allow the measurement of smaller drop-sizes, validating the present work [52]. For superhydrophobic surfaces with large contact angles and high nucleation densities, measuring accurate drop-size distributions may be difficult since larger drops obscure smaller drops that grow in their shadow. However, the current computation model could still be validated by measuring drop-size distributions on surfaces that have low contact angles and/or low nucleation densities.

Development of a Comprehensive Heat Transfer Model

The results of the simulation are dependent on the nucleation density, which is a function of the surface subcooling. Furthermore, the results in chapter 5 suggest that the subcooling may also influence the pinned area of a condensing drop, which also influences the maximum drop size and which is used in some models for variable contact angle. In order to create a comprehensive model that could predict condensation heat transfer rate as a function of surface subcooling and obtain the heat transfer coefficient, it is essential to understand the relationship between surface subcooling, nucleation density, maximum drop size, and total adhesive force.

7.6.2 Drop-Behavior Transition and Drop-Size Distribution During Dropwise Condensation on Superhydrophobic Surfaces (chapter 5)

Future work in this section can be divided into work that will be completed to make the work in this chapter suitable for publication and additional work related to the content of chapter 5.

For Publication

1. The surfaces tested in this chapter were attached by bolting a plastic clamp to the polycarbonate block in which the copper block was epoxied (see Figure 5.1b). The holder interfaced with the superhydrophobic surface around edges, crushing the nanostructures directly

beneath the clamp. As a result, during condensation the area adjacent to the holder would flood, and the flooding front progressed inward during the test. The flooding front did not cover the majority of the surface, but it is possible that its presence caused the weak temporal variation in drop size observed in chapter 5. Experiments will be conducted using a holder which only interfaces with the CICNT surface at certain points, rather than all around the edge in order to determine whether the temporal influence is caused by the progression of the flooding front from the surface edge, making it a problem specific to the surface macro-geometry, or whether the temporal variation is caused by something occurring at the nanoscale, such as the cavities slowly becoming saturated with condensate.

2. The following additional data will be added to Figure 5.7.

   (a) Additional data where flooding occurs

   (b) Additional data for CICNT surfaces with diameters in between 60 and 80 nm

   (c) Potentially re-take data for cases where the test lasted for more than 1 hour. If this is done, surfaces on which condensation has occurred once should be investigated to determine whether they can be re-used after vacuum baking to avoid the need to fabricate additional surfaces.

Additional Future Work

The dependence of the drop behavior and size on subcooling and nanostructure size is likely caused by an increase in adhesive force, as discussed in chapter 5. However, the underlying cause of the increase in adhesive force is unknown. Understanding the cause of the increase in adhesion force with surface subcooling is important when designing superhydrophobic surfaces to be used in practical applications, and will be especially important when investigating drop behavior and heat transfer rates in a flow-condensing environment.

7.6.3 Measuring Condensation Heat Transfer (chapter 6)

With the preparatory work described in chapter 6 further research could answer several important questions. Since the copper oxide SH surfaces allow accurate measurement of the sur-

face temperature, accurate condensation heat transfer coefficients can be obtained. A connection between measured heat transfer rate and drop statistics obtained using the various drop tracking algorithms could be established. Understanding the connection is important for heat transfer modeling and could guide development of surfaces designed to maximize condensation heat transfer rates. For example, the idea that minimizing the maximum drop size has motivated development of surfaces capable of coalescence-induced jumping, and even the optimization of surfaces for smaller minimum departure sizes [42–44]. However, recent modeling efforts suggest that minimizing the maximum drop size may not be optimal, but experimental measurements could answer the question more definitively.

The influence of two-tiered geometry on the overall heat transfer coefficient could be explored. As described in chapter 5, the microstructure geometry influences drop behavior, but it is unclear how that translates into heat transfer performance. Exploring the relative rate of heat transfer could provide insight into whether the presence of a microstructure can improve heat transfer rates, as suggested by Rykaczewski *et al.* [34] or inhibit heat transfer, as suggested by Zhang *et al.* [50]. Furthermore, the contact resistance between a condensing surface and the copper block can be obtained once the surface temperature is known, and if the contact resistance is relatively repeatable, could be used to estimate the condensation heat transfer coefficient from the overall heat transfer coefficient which is measured in chapter 6.

One remaining challenge which has not yet been addressed with the work in chapter 6 is how to obtain a constant subcooling. During some condensation tests the subcooling changes slowly. In some cases, the saturation temperature decreases due to the high rate of evaporation at the Erlenmeyer flask. The temperature decrease is slowed by continuously mixing the water during condensation; however, even with vigorous mixing the bulk temperature of the water in the flask still decreases with time. In other cases, dependent on the rate of heat transfer, the temperature gradually increases due to the heat generated by the stir plate. The vapor temperature could be maintained by the use of a bellows valve as described in the supplementary information of the work by Miljkovic *et al.* [35]. The copper temperature, T_c also sometimes changes with constant chiller temperature as the heat flux changes. The coolant temperature is precisely controlled with the constant temperature bath, but the temperature in the copper is dependent on the rate of heat transfer ($T_c = q"/R + T_{coolant}$), where R is the total thermal resistance between the coolant water

and the copper block and T_{coolant} is the temperature of the coolant leaving when it enters the heat exchanger).

7.7 Impact

Though the challenge of improved condensation heat transfer is complex, the need is compelling. The introduction mentioned that nearly one billion people world-wide lack access to clean drinking water. When one considers that contaminated water transmits diseases such as diarrhea, cholera, dysentery, typhoid, and polio, the statistic becomes sobering. Contaminated drinking water is estimated to cause 500,000 preventable deaths each year [3]. Can superhydrophobic surfaces be used to improve the efficiency of condensation devices to the point that boiling and re-condensing water are viable options for obtaining clean water? Neither this dissertation nor the available research can answer the question, but the present research does contribute towards the understanding required to evaluate the potential of superhydrophobic surfaces in this arena. Fundamental condensation research leads to greater understanding of the complex interactions involved, potentially allowing the development of engineering solutions that will change the world.

REFERENCES

[1] Beér, J. M., 2007. "High efficiency electric power generation: The environmental role." *Progress in Energy and Combustion Science,* **33**(2), pp. 107–134. 1, 37, 68

[2] Kehlhofer, R., Hannemann, F., Rukes, B., and Stirnimann, F., 2009. *Combined-Cycle Gas and Steam Turbine Power Plants*. PennWell. 1

[3] World Health Organization, 2018. Drinking water. <http://www.who.int/news-room/fact-sheets/detail/drinking-water>. 1, 110

[4] Vasiliev, L. L., 2005. "Heat pipes in modern heat exchangers." *Applied Thermal Engineering,* **25**(1), pp. 1–19. 1, 37, 68

[5] Carey, V. P., 2008. *Liquid-vapor phase-change phenomena: An introduction to the thermophysics of vaporization and condensation processes in heat transfer equipment*. Taylor and Francis, New York. 1, 40

[6] Schmidt, E., Schurig, W., and Sellschopp, W., 1930. "Versuche ber die kondensation von wasserdampf in film- und tropfenform." *Technische Mechanik und Thermodynamik,* **1**(2), pp. 53–63. 3, 37, 68

[7] Rose, J. W., 2002. "Dropwise condensation theory and experiment: A review." *Proceedings of the Institution of Mechanical Engineers Part A: Journal of Power and Energy,* **216**(A2), pp. 115–128. 3, 6, 9, 37, 62, 68, 72, 89, 95

[8] Cho, H. J., Preston, D. J., Zhu, Y., and Wang, E. N., 2016. "Nanoengineered materials for liquidvapour phase-change heat transfer." *Nature Reviews Materials,* **2**, p. 16092. 3, 5, 81

[9] Attinger, D., Frankiewicz, C., Betz, A. R., Schutzius, T. M., Ganguly, R., Das, A., Kim, C.-J., and Megaridis, C. M., 2014. "Surface engineering for phase change heat transfer: A review." *MRS Energy and Sustainability,* **1**, pp. 1–40. 3, 37, 68

[10] Enright, R., Miljkovic, N., Alvarado, J. L., Kim, K., and Rose, J. W., 2014. "Dropwise condensation on micro- and nanostructured surfaces." *Nanoscale and Microscale Thermophysical Engineering,* **18**(3), pp. 223–250. 3

[11] Ma, X.-H., Zhou, X.-D., Lan, Z., Li, Y.-M., and Zhang, Y., 2008. "Condensation heat transfer enhancement in the presence of non-condensable gas using the interfacial effect of dropwise condensation." *International Journal of Heat and Mass Transfer,* **51**(7), pp. 1728–1737. 3

[12] Minkowycz, W. J., and Sparrow, E. M., 1966. "Condensation heat transfer in the presence of noncondensables, interfacial resistance, superheating, variable properties, and diffusion." *International Journal of Heat and Mass Transfer,* **9**(10), pp. 1125–1144. 3

[13] Law, K.-Y., 2014. "Definitions for hydrophilicity, hydrophobicity, and superhydrophobicity: Getting the basics right." *Journal of Physical Chemistry Letters,* **5**, pp. 686–688. 4, 9, 27, 38

[14] Chen, W., Fadeev, A. Y., Hsieh, M. C., Oner, D., Youngblood, J., and McCarthy, T. J., 1999. "Ultrahydrophobic and ultralyophobic surfaces: Some comments and examples." *Langmuir,* **15**(10), pp. 3395–3399. 4, 27, 38

[15] Quere, D., 2008. "Wetting and roughness." *Annual Review of Materials Research,* **38**, pp. 71–99. 4

[16] Gao, L., and McCarthy, T. J., 2009. "Wetting 101." *Langmuir,* **25**(24), pp. 14105–14115. 4, 80

[17] Miljkovic, N., Enright, R., and Wang, E. N., 2013. "Modeling and optimization of superhydrophobic condensation." *Journal of Heat Transfer,* **135**(11), p. 111004. 5, 7, 37, 38, 39, 41, 45, 50, 51, 52, 53, 54, 55, 61, 62, 64, 66, 69, 72, 105, 106

[18] Lafuma, A., and Quere, D., 2003. "Superhydrophobic states." *Nature Materials,* **2**(7), pp. 457–460. 5

[19] Narhe, R., and Beysens, D., 2006. "Water condensation on a super-hydrophobic spike surface." *EPL (Europhysics Letters),* **75**(1), p. 98. 5

[20] Wier, K. A., and McCarthy, T. J., 2006. "Condensation on ultrahydrophobic surfaces and its effect on droplet mobility: ultrahydrophobic surfaces are not always water repellant." *Langmuir,* **22**(6), pp. 2433–2436. 5

[21] Narhe, R. D., and Beysens, D. A., 2007. "Growth dynamics of water drops on a square-pattern rough hydrophobic surface." *Langmuir,* **23**(12), pp. 6486–6489. 5

[22] Cheng, Y. T., and Rodak, D. E., 2005. "Is the lotus leaf superhydrophobic?." *Applied Physics Letters,* **86**(14). 5

[23] Cheng, Y. T., Rodak, D. E., Angelopoulos, A., and Gacek, T., 2005. "Microscopic observations of condensation of water on lotus leaves." *Applied Physics Letters,* **87**(19). 5

[24] Jung, Y. C., and Bhushan, B., 2008. "Wetting behaviour during evaporation and condensation of water microdroplets on superhydrophobic patterned surfaces." *Journal of Microscopy,* **229**(1), pp. 127–140. 5

[25] Dorrer, C., and Rhe, J., 2007. "Condensation and wetting transitions on microstructured ultrahydrophobic surfaces." *Langmuir,* **23**(7), pp. 3820–3824. 5

[26] Chen, C. H., Cai, Q. J., Tsai, C. L., Chen, C. L., Xiong, G. Y., Yu, Y., and Ren, Z. F., 2007. "Dropwise condensation on superhydrophobic surfaces with two-tier roughness." *Applied Physics Letters,* **90**(17). 5, 27

[27] Dorrer, C., and Rhe, J., 2008. "Wetting of silicon nanograss: From superhydrophilic to superhydrophobic surfaces." *Advanced Materials,* **20**(1), pp. 159–163. 5

[28] Wang, F. C., Yang, F. Q., and Zhao, Y. P., 2011. "Size effect on the coalescence-induced self-propelled droplet." *Applied Physics Letters,* **98**(5). 5

[29] Enright, R., Miljkovic, N., Al-Obeidi, A., Thompson, C. V., and Wang, E. N., 2012. "Condensation on superhydrophobic surfaces: The role of local energy barriers and structure length scale." *Langmuir,* **28**(40), pp. 14424–14432. 5, 33, 38, 50, 51, 52, 69, 81

[30] Rykaczewski, K., Osborn, W. A., Chinn, J., Walker, M. L., Scott, J. H. J., Jones, W., Hao, C. L., Yao, S. H., and Wang, Z. K., 2012. "How nanorough is rough enough to make a surface superhydrophobic during water condensation?." *Soft Matter,* **8**(33), pp. 8786–8794. 5, 47, 70

[31] Ko, T. J., Her, E. K., Shin, B., Kim, H. Y., Lee, K. R., Hong, B. K., Kim, S. H., Oh, K. H., and Moon, M. W., 2012. "Water condensation behavior on the surface of a network of superhydrophobic carbon fibers with high-aspect-ratio nanostructures." *Carbon,* **50**(14), pp. 5085–5092. 5

[32] Miljkovic, N., and Wang, E. N., 2013. "Condensation heat transfer on superhydrophobic surfaces." *MRS Bulletin,* **38**, pp. 397–406. 5, 88

[33] Lo, C. W., Wang, C. C., and Lu, M. C., 2014. "Scale effect on dropwise condensation on superhydrophobic surfaces." *ACS Applied Materials and Interfaces,* **6**(16), pp. 14353–14359. 5

[34] Rykaczewski, K., Paxson, A. T., Anand, S., Chen, X., Wang, Z., and Varanasi, K. K., 2013. "Multimode multidrop serial coalescence effects during condensation on hierarchical superhydrophobic surfaces." *Langmuir,* **29**(3), pp. 881–891. 5, 7, 70, 87, 109

[35] Miljkovic, N., Enright, R., Nam, Y., Lopez, K., Dou, N., Sack, J., and Wang, E. N., 2013. "Jumping-droplet-enhanced condensation on scalable superhydrophobic nanostructured surfaces." *Nano Letters,* **13**(1), pp. 179–187. 5, 7, 9, 38, 53, 54, 69, 87, 95, 109, 186

[36] Chen, X., Weibel, J. A., and Garimella, S. V., 2017. "Characterization of coalescence-induced droplet jumping height on hierarchical superhydrophobic surfaces." *ACS Omega,* **2**(6), pp. 2883–2890. 5, 70, 104

[37] Dietz, C., Rykaczewski, K., Fedorov, A. G., and Joshi, Y., 2010. "Visualization of droplet departure on a superhydrophobic surface and implications to heat transfer enhancement during dropwise condensation." *Applied Physics Letters,* **97**(3). 5

[38] Rykaczewski, K., Scott, J. H. J., Rajauria, S., Chinn, J., Chinn, A. M., and Jones, W., 2011. "Three dimensional aspects of droplet coalescence during dropwise condensation on superhydrophobic surfaces." *Soft Matter,* **7**(19), pp. 8749–8752. 5, 47, 50, 58

[39] Miljkovic, N., Enright, R., and Wang, E. N., 2012. "Effect of droplet morphology on growth dynamics and heat transfer during condensation on superhydrophobic nanostructured surfaces." *ACS Nano,* **6**(2), pp. 1776–1785. 5, 7, 9, 38, 50, 52, 87, 96

[40] Kollera, M., and Grigull, U., 1969. "Über das abspringen von tropfen bei der kondensation von quecksilber." *Wärme-und Stoffübertragung,* **2**(1), pp. 31–35. 6

[41] Boreyko, J. B., and Chen, C.-H., 2009. "Self-propelled dropwise condensate on superhydrophobic surfaces." *Physical Review Letters,* **103**(18), p. 184501. 6, 9, 38, 68, 87

[42] Mouterde, T., Lehoucq, G., Xavier, S., Checco, A., Black, C. T., Rahman, A., Midavaine, T., Clanet, C., and Qur, D., 2017. "Antifogging abilities of model nanotextures." *Nature Materials,* **16**, pp. 658–663. 6, 38, 43, 44, 45, 70, 71, 80, 82, 104, 109

[43] Cha, H., Xu, C., Sotelo, J., Chun, J. M., Yokoyama, Y., Enright, R., and Miljkovic, N., 2016. "Coalescence-induced nanodroplet jumping." *Physical Review Fluids,* **1**(6), p. 064102. 6, 27, 33, 38, 43, 44, 68, 70, 87, 109

[44] Mulroe, M. D., Srijanto, B. R., Ahmadi, S. F., Collier, C. P., and Boreyko, J. B., 2017. "Tuning superhydrophobic nanostructures to enhance jumping-droplet condensation." *ACS Nano,* **11**(8), pp. 8499–8510. 6, 33, 43, 44, 70, 109

[45] Boreyko, J. B., and Collier, C. P., 2013. "Delayed frost growth on jumping-drop superhydrophobic surfaces." *ACS Nano,* **7**(2), pp. 1618–1627. 6

[46] Boreyko, J. B., and Chen, C.-H., 2013. "Vapor chambers with jumping-drop liquid return from superhydrophobic condensers." *International Journal of Heat and Mass Transfer,* **61**, pp. 409–418. 6

[47] Shahriari, A., Birbarah, P., Oh, J., Miljkovic, N., and Bahadur, V., 2017. "Electric field-based control and enhancement of boiling and condensation." *Nanoscale and Microscale Thermophysical Engineering,* **21**(2), pp. 102–121. 6

[48] Wang, K., Liang, Q., Jiang, R., Zheng, Y., Lan, Z., and Ma, X., 2016. "Self-enhancement of droplet jumping velocity: the interaction of liquid bridge and surface texture." *RSC Advances,* **6**(101), pp. 99314–99321. 7

[49] Chen, X., Wu, J., Ma, R., Hua, M., Koratkar, N., Yao, S., and Wang, Z., 2011. "Nanograssed micropyramidal architectures for continuous dropwise condensation." *Advanced Functional Materials,* **21**(24), pp. 4617–4623. 7, 70, 87

[50] Zhang, P., Maeda, Y., Lv, F., Takata, Y., and Orejon, D., 2017. "Enhanced coalescence-induced droplet-jumping on nanostructured superhydrophobic surfaces in the absence of microstructures." *ACS Applied Materials and Interfaces,* **9**(40), pp. 35391–35403. 7, 70, 87, 109

[51] Wen, R., Xu, S., Zhao, D., Lee, Y.-C., Ma, X., and Yang, R., 2017. "Hierarchical superhydrophobic surfaces with micropatterned nanowire arrays for high-efficiency jumping droplet condensation." *ACS Applied Materials and Interfaces,* **9**(51), pp. 44911–44921. 7, 45, 71, 77, 80, 87, 95

[52] Ölçeroğlu, E., Hsieh, C.-Y., Rahman, M. M., Lau, K. K. S., and McCarthy, M., 2014. "Full-field dynamic characterization of superhydrophobic condensation on biotemplated nanostructured surfaces." *Langmuir,* **30**(25), pp. 7556–7566. 7, 47, 87, 93, 107

[53] Sharma, C. S., Combe, J., Giger, M., Emmerich, T., and Poulikakos, D., 2017. "Growth rates and spontaneous navigation of condensate droplets through randomly structured textures." *ACS Nano*. 7, 47, 87

[54] Aili, A., Ge, Q., and Zhang, T., 2017. "How nanostructures affect water droplet nucleation on superhydrophobic surfaces." *Journal of Heat Transfer,* **139**(11), pp. 112401–112401–10. 7, 87

[55] Chavan, S., Cha, H., Orejon, D., Nawaz, K., Singla, N., Yeung, Y. F., Park, D., Kang, D. H., Chang, Y., Takata, Y., and Miljkovic, N., 2016. "Heat transfer through a condensate droplet on hydrophobic and nanostructured superhydrophobic surfaces." *Langmuir,* **32**(31), pp. 7774–7787. 7, 41, 87

[56] Kim, S., and Kim, K. J., 2011. "Dropwise condensation modeling suitable for superhydrophobic surfaces." *Journal of Heat Transfer,* **133**(8), p. 081502. 7, 37, 38, 41, 45, 52, 53, 54, 55, 59, 60, 66, 69, 87, 106

[57] Wen, R., Li, Q., Wu, J., Wu, G., Wang, W., Chen, Y., Ma, X., Zhao, D., and Yang, R., 2017. "Hydrophobic copper nanowires for enhancing condensation heat transfer." *Nano Energy,* **33**, pp. 177–183. 7, 71, 87, 95

[58] Wen, R., Xu, S., Ma, X., Lee, Y.-C., and Yang, R., 2018. "Three-dimensional superhydrophobic nanowire networks for enhancing condensation heat transfer." *Joule,* **2**(2), pp. 269–279. 7, 45, 71, 87, 95

[59] Stevens, K. A., Crockett, J., Maynes, D. R., and Iverson, B. D., 2017. "Two-phase flow pressure drop in superhydrophobic channels." *International Journal of Heat and Mass Transfer,* **110**, pp. 515–522. 8

[60] Lienhard IV, J., and Lienhard V, J., 2003. *A Heat Transfer Textbook*., 3rd ed. Phlogiston Press, Cambridge. 9

[61] Glicksman, L. R., and Hunt, A. W., 1972. "Numerical simulation of dropwise condensation." *International Journal of Heat and Mass Transfer,* **15**(11), pp. 2251–2269. 9, 39, 51, 62, 66

[62] Love, J. C., Estroff, L. A., Kriebel, J. K., Nuzzo, R. G., and Whitesides, G. M., 2005. "Self-assembled monolayers of thiolates on metals as a form of nanotechnology." *Chemical Reviews,* **105**(4), pp. 1103–1169. 9

[63] Andrews, H. G., Eccles, E. A., Schofield, W. C., and Badyal, J. P., 2011. "Three-dimensional hierarchical structures for fog harvesting." *Langmuir,* **27**(7), pp. 3798–3802. 9, 37, 68

[64] Leach, R. N., Stevens, F., Langford, S. C., and Dickinson, J. T., 2006. "Dropwise condensation: experiments and simulations of nucleation and growth of water drops in a cooling system." *Langmuir,* **22**(21), pp. 8864–8872. 9, 39

[65] Lockhart, R., and Martinelli, R., 1949. "Proposed correlation of data for isothermal two-phase, two-component flow in pipes." *Chemical Engineering Progress,* **45**(1), pp. 39–48. 11

[66] Chisholm, D., and Laird, A., 1958. "Two-phase flow in rough tubes." *Trans. ASME,* **80**(2), pp. 276–286. 11

[67] Chisholm, D., 1967. "A theoretical basis for lockhart-martinelli correlation for 2-phase flow." *International Journal of Heat and Mass Transfer,* **10**(12), pp. 1767–1778. 11

[68] Sun, L., and Mishima, K., 2009. "Evaluation analysis of prediction methods for two-phase flow pressure drop in mini-channels." *International Journal of Multiphase Flow,* **35**(1), pp. 47–54. 12

[69] Asadi, M., Xie, G., and Sunden, B., 2014. "A review of heat transfer and pressure drop characteristics of single and two-phase microchannels." *International Journal of Heat and Mass Transfer,* **79**, pp. 34–53. 12

[70] Kim, S. M., and Mudawar, I., 2012. "Universal approach to predicting two-phase frictional pressure drop for adiabatic and condensing mini/micro-channel flows." *International Journal of Heat and Mass Transfer,* **55**(11-12), pp. 3246–3261. 12, 20, 22

[71] Kim, S.-M., and Mudawar, I., 2014. "Review of databases and predictive methods for pressure drop in adiabatic, condensing and boiling mini/micro-channel flows." *International Journal of Heat and Mass Transfer,* **77**, pp. 74–97. 12

[72] Cho, S. C., and Wang, Y., 2014. "Two-phase flow dynamics in a micro channel with heterogeneous surfaces." *International Journal of Heat and Mass Transfer,* **71**, pp. 349–360. 12, 25

[73] Cubaud, T., Ulmanella, U., and Ho, C.-M., 2006. "Two-phase flow in microchannels with surface modifications." *Fluid Dynamics Research,* **38**(11), pp. 772–786. 12

[74] Huh, D., Kuo, C. H., Grotberg, J. B., and Takayama, S., 2009. "Gasliquid two-phase flow patterns in rectangular polymeric microchannels: effect of surface wetting properties." *New Journal of Physics,* **11**, p. 75034. 12

[75] Barajas, A. M., and Panton, R. L., 1993. "The effects of contact-angle on 2-phase flow in capillary tubes." *International Journal of Multiphase Flow,* **19**(2), pp. 337–346. 12

[76] Takamasa, T., Hazuku, T., and Hibiki, T., 2008. "Experimental study of gasliquid two-phase flow affected by wall surface wettability." *International Journal of Heat and Fluid Flow,* **29**(6), pp. 1593–1602. 12, 25

[77] Phan, H. T., Caney, N., Marty, P., Colasson, S., and Gavillet, J., 2011. "Flow boiling of water in a minichannel: The effects of surface wettability on two-phase pressure drop." *Applied Thermal Engineering,* **31**(11-12), pp. 1894–1905. 12, 25

[78] Choi, C., Yu, D. I., and Kim, M., 2011. "Surface wettability effect on flow pattern and pressure drop in adiabatic two-phase flows in rectangular microchannels with t-junction mixer." *Experimental Thermal and Fluid Science,* **35**(6), pp. 1086–1096. 12, 25

[79] Wang, Y., Al Shakhshir, S., Li, X., and Chen, P., 2014. "Superhydrophobic flow channel surface and its impact on pem fuel cell performance." *International Journal of Low-Carbon Technologies,* **9**(3), pp. 225–236. 13, 14, 23, 25

[80] Philip, J. R., 1972. "Flows satisfying mixed no-slip and no-shear conditions." *Zeitschrift Fur Angewandte Mathematik Und Physik,* **23**(3), pp. 353–372. 13, 17, 19

[81] Lauga, E., and Stone, H. A., 2003. "Effective slip in pressure-driven stokes flow." *Journal of Fluid Mechanics,* **489**, pp. 55–77. 13

[82] Maynes, D., Jeffs, K., Woolford, B., and Webb, B. W., 2007. "Laminar flow in a microchannel with hydrophobic surface patterned microribs oriented parallel to the flow direction." *Physics of Fluids,* **19**(9), pp. 093603–1–12. 13

[83] Woolford, B., Maynes, D., and Webb, B. W., 2009. "Liquid flow through microchannels with grooved walls under wetting and superhydrophobic conditions." *Microfluidics and Nanofluidics,* **7**(1), pp. 121–135. 13

[84] Enright, R., Hodes, M., Salamon, T., and Muzychka, Y., 2014. "Isoflux nusselt number and slip length formulae for superhydrophobic microchannels." *Journal of Heat Transfer,* **136**(1), p. 012402. 13, 18, 19

[85] Torresin, D., Tiwari, M. K., Del Col, D., and Poulikakos, D., 2013. "Flow condensation on copper-based nanotextured superhydrophobic surfaces." *Langmuir,* **29**(2), pp. 840–848. 13

[86] Birbarah, P., and Miljkovic, N., 2017. "External convective jumping-droplet condensation on a flat plate." *International Journal of Heat and Mass Transfer,* **107**, pp. 74–88. 13, 100, 105

[87] Prince, J., 2013. "The influence of superhydrophobicity on laminar jet impingement and turbulent flow in a channel with walls exhibiting riblets." Thesis, Brigham Young University. 16, 87, 89

[88] Shah, R. K., and London, A. L., 1978. *Laminar Flow Forced Convection in Ducts*. Academic Press, New York, New York, book section 7, pp. 196–219. 17

[89] Wambsganss, M. W., Jendrzejczyk, J. A., and France, D. M., 1991. "2-phase flow patterns and transitions in a small, horizontal, rectangular channel." *International Journal of Multiphase Flow,* **17**(3), pp. 327–342. 19

[90] Stevens, K. A., Esplin, C. D., Davis, T. M., Butterfield, D. J., Ng, P. S., Bowden, A. E., Jensen, B. D., and Iverson, B. D., 2018. "Superhydrophobic, carbon-infiltrated carbon nanotubes on si and 316l stainless steel with tunable geometry." *Applied Physics Letters,* **112**(21), p. 211602. 26, 73, 80

[91] Cha, H., Chun, J. M., Sotelo, J., and Miljkovic, N., 2016. "Focal plane shift imaging for the analysis of dynamic wetting processes." *ACS Nano,* **10**(9), pp. 8223–8232. 27, 33, 44, 47, 70, 88, 104

[92] Cheng, J. T., Vandadi, A., and Chen, C. L., 2012. "Condensation heat transfer on two-tier superhydrophobic surfaces." *Applied Physics Letters,* **101**(13). 27

[93] Enright, R., Miljkovic, N., Sprittles, J., Nolan, K., Mitchell, R., and Wang, E. N., 2014. "How coalescing droplets jump." *ACS Nano,* **8**(10), pp. 10352–10362. 27, 38, 104

[94] Huang, T. C., Li, P., Yao, H. Q., Sue, H. J., Kotaki, M., and Tsai, M. H., 2016. "Highly efficient oil-water separators based on dual superhydrophobic and superoleophilic properties of multiwall-carbon nanotube filtration films." *RSC Advances,* **6**(15), pp. 12422–12425. 27

[95] Lee, C. H., Johnson, N., Drelich, J., and Yap, Y. K., 2011. "The performance of superhydrophobic and superoleophilic carbon nanotube meshes in water-oil filtration." *Carbon,* **49**(2), pp. 669–676. 27

[96] Gui, X., Wei, J., Wang, K., Cao, A., Zhu, H., Jia, Y., Shu, Q., and Wu, D., 2010. "Carbon nanotube sponges." *Advanced Materials,* **22**(5), pp. 617–621. 27

[97] Bhushan, B., and Jung, Y. C., 2011. "Natural and biomimetic artificial surfaces for superhydrophobicity, self-cleaning, low adhesion, and drag reduction." *Progress in Materials Science,* **56**(1), pp. 1–108. 27

[98] Nosonovsky, M., and Bhushan, B., 2009. "Superhydrophobic surfaces and emerging applications: Non-adhesion, energy, green engineering." *Current Opinion in Colloid and Interface Science,* **14**(4), pp. 270–280. 27

[99] Al-Jumaili, A., Alancherry, S., Bazaka, K., and Jacob, V. M., 2017. "Review on the antimicrobial properties of carbon nanostructures." *Materials,* **10**(9). 27

[100] Hoyos-Palacio, L. M., Garca, A. G., Prez-Robles, J. F., Gonzlez, J., and Martnez-Tejada, H. V., 2014. "Catalytic effect of fe, ni, co and mo on the cnts production." *IOP Conference Series: Materials Science and Engineering,* **59**(1), p. 012005. 27

[101] Kang, S., Herzberg, M., Rodrigues, D. F., and Elimelech, M., 2008. "Antibacterial effects of carbon nanotubes: Size does matter!." *Langmuir,* **24**(13), pp. 6409–6413. 27

[102] Gong, Q. M., Li, Z., Bai, X. D., Li, D., Zhao, Y., and Liang, J., 2004. "Thermal properties of aligned carbon nanotube/carbon nanocomposites." *Materials Science and Engineering a-Structural Materials Properties Microstructure and Processing,* **384**(1-2), pp. 209–214. 27, 34

[103] Gong, Q. M., Li, Z., Li, D., Bai, X. D., and Liang, J., 2004. "Fabrication and structure: a study of aligned carbon nanotube/carbon nanocomposites." *Solid State Communications,* **131**(6), pp. 399–404. 27, 34

[104] Han, Z. J., Tay, B. K., Shakerzadeh, M., and Ostrikov, K., 2009. "Superhydrophobic amorphous carbon/carbon nanotube nanocomposites." *Applied Physics Letters,* **94**(22), p. 223106. 27

[105] Han, Z., Tay, B., Tan, C., Shakerzadeh, M., and Ostrikov, K., 2009. "Electrowetting control of cassie-to-wenzel transitions in superhydrophobic carbon nanotube-based nanocomposites." *ACS Nano,* **3**(10), pp. 3031–3036. 27

[106] Hanna, B. H., Fazio, W. C., Tanner, J. D., Lund, J. M., Wood, T. S., Davis, R. C., Vanfleet, R. R., and Jensen, B. D., 2014. "Mechanical property measurement of carbon infiltrated carbon nanotube structures for compliant micromechanisms." *Journal of Microelectromechanical Systems,* **23**(6), pp. 1330–1339. 27, 34

[107] Jones, K., Jensen, B. D., and Bowden, A., 2013. "Fabrication and testing of planar stent mesh designs using carbon-infiltrated carbon nanotubes." *Journal of Nanotechnology in Engineering and Medicine,* **4**(2), pp. 020903–020903–7. 27, 34

[108] Lee, J., Kim, T., Jung, Y., Jung, K., Park, J., Lee, D. M., Jeong, H. S., Hwang, J. Y., Park, C. R., Lee, K. H., and Kim, S. M., 2016. "High-strength carbon nanotube/carbon composite fibers via chemical vapor infiltration." *Nanoscale,* **8**(45), pp. 18972–18979. 27, 34

[109] Li, X. S., Ci, L., Kar, S., Soldano, C., Kilpatrick, S. J., and Ajayan, P. M., 2007. "Densified aligned carbon nanotube films via vapor phase infiltration of carbon." *Carbon,* **45**(4), pp. 847–851. 27, 34

[110] Lau, K. K. S., Bico, J., Teo, K. B. K., Chhowalla, M., Amaratunga, G. A. J., Milne, W. I., McKinley, G. H., and Gleason, K. K., 2003. "Superhydrophobic carbon nanotube forests." *Nano Letters,* **3**(12), pp. 1701–1705. 27, 29

[111] Li, H. J., Wang, X. B., Song, Y. L., Liu, Y. Q., Li, Q. S., Jiang, L., and Zhu, D. B., 2001. "Super-"amphiphobic" aligned carbon nanotube films." *Angewandte Chemie-International Edition,* **40**(9), pp. 1743–1746. 27

[112] Li, S., Li, H., Wang, X., Song, Y., Liu, Y., Jiang, L., and Zhu, D., 2002. "Superhydrophobicity of large-area honeycomb-like aligned carbon nanotubes." *The Journal of Physical Chemistry B,* **106**(36), pp. 9274–9276. 27

[113] Liu, H., Zhai, J., and Jiang, L., 2006. "Wetting and anti-wetting on aligned carbon nanotube films." *Soft Matter,* **2**(10), pp. 811–821. 27, 29

[114] Hong, Y. C., and Uhm, H. S., 2006. "Superhydrophobicity of a material made from multi-walled carbon nanotubes." *Applied Physics Letters,* **88**(24), p. 244101. 27

[115] Li, P. H., Lim, X. D., Zhu, Y. W., Yu, T., Ong, C. K., Shen, Z. X., Wee, A. T. S., and Sow, C. H., 2007. "Tailoring wettability change on aligned and patterned carbon nanotube films for selective assembly." *Journal of Physical Chemistry B,* **111**(7), pp. 1672–1678. 28

[116] Aria, A. I., and Gharib, M., 2011. "Reversible tuning of the wettability of carbon nanotube arrays: The effect of ultraviolet/ozone and vacuum pyrolysis treatments." *Langmuir,* **27**(14), pp. 9005–9011. 28

[117] Aria, A., and Gharib, M., 2011. "Carbon nanotube arrays with tunable wettability and their applications." In *Nanotech 2011: Technical Proceedings of the 2011 NSTI Nanotechnology Conference and Expo*, Vol. 1, pp. 149–152. 28

[118] Aria, A. I., and Gharib, M., 2013. "Dry oxidation and vacuum annealing treatments for tuning the wetting properties of carbon nanotube arrays." *Journal of Visualized Experiments : JoVE*(74), p. 50378. 28, 29, 73

[119] Wang, H. Z., Huang, Z. P., Cai, Q. J., Kulkarni, K., Chen, C. L., Carnahan, D., and Ren, Z. F., 2010. "Reversible transformation of hydrophobicity and hydrophilicity of aligned carbon nanotube arrays and buckypapers by dry processes." *Carbon,* **48**(3), pp. 868–875. 28

[120] Atefi, E., Mann, J. A., and Tavana, H., 2013. "A robust polynomial fitting approach for contact angle measurements." *Langmuir,* **29**(19), pp. 5677–5688. 30

[121] Bateni, A., Susnar, S. S., Amirfazli, A., and Neumann, A. W., 2003. "A high-accuracy polynomial fitting approach to determine contact angles." *Colloids and Surfaces A: Physicochemical and Engineering Aspects,* **219**(1), pp. 215–231. 30

[122] Berg, J., 1993. *Wettability*. Taylor and Francis Group, New York. 30

[123] Gao, L., and McCarthy, T. J., 2006. "Contact angle hysteresis explained." *Langmuir,* **22**(14), pp. 6234–6237. 30

[124] Jeong, G.-H., Olofsson, N., Falk, L. K. L., and Campbell, E. E. B., 2009. "Effect of catalyst pattern geometry on the growth of vertically aligned carbon nanotube arrays." *Carbon,* **47**(3), pp. 696–704. 31

[125] Khawaji, A. D., Kutubkhanah, I. K., and Wie, J.-M., 2008. "Advances in seawater desalination technologies." *Desalination,* **221**(1), pp. 47–69. 37, 68

[126] Humplik, T., Lee, J., OHern, S. C., Fellman, B. A., Baig, M. A., Hassan, S. F., Atieh, M. A., Rahman, F., Laoui, T., Karnik, R., and Wang, E. N., 2011. "Nanostructured materials for water desalination." *Nanotechnology,* **22**(29), p. 292001. 37, 68

[127] Lee, A., Moon, M.-W., Lim, H., Kim, W.-D., and Kim, H.-Y., 2012. "Water harvest via dewing." *Langmuir,* **28**(27), pp. 10183–10191. 37, 68

[128] Prez-Lombard, L., Ortiz, J., and Pout, C., 2008. "A review on buildings energy consumption information." *Energy and Buildings,* **40**(3), pp. 394–398. 37, 68

[129] Le Fevre, E. J., and Rose, J. W., 1966. "A theory of heat transfer by dropwise condensation." *Proceedings of the Third International Heat Transfer Conference,* **2**, pp. 362–375. 37, 38, 39, 52, 53, 55, 59, 66, 80, 100

[130] Rose, J. W., and Glicksman, L. R., 1973. "Dropwise condensation–the distribution of drop sizes." *International Journal of Heat and Mass Transfer,* **16**(2), pp. 411–425. 37, 38, 52, 53, 55, 59, 66, 72, 80, 100

[131] Tanasawa, I., and Tachibana, F., 1970. "A synthesis of the total process of dropwise condensation using the method of computer simulation." *Proceedings of the 4th International Heat Transfer Conference*, pp. 1–11. 37, 39

[132] Tanaka, H., 1975. "A theoretical study of dropwise condensation." *Journal of Heat Transfer,* **97**(1), pp. 72–78. 37, 38

[133] Watanabe, N., Aritomi, M., and Machida, A., 2014. "Time-series characteristics and geometric structures of drop-size distribution density in dropwise condensation." *International Journal of Heat and Mass Transfer,* **76**, pp. 467–483. 37, 72, 81

[134] Wen, R., Lan, Z., Peng, B., Xu, W., and Ma, X., 2015. "Droplet dynamics and heat transfer for dropwise condensation at lower and ultra-lower pressure." *Applied Thermal Engineering,* **88**, pp. 265–273. 37

[135] Wen, H. W., and Jer, R. M., 1976. "On the heat transfer in dropwise condensation." *The Chemical Engineering Journal,* **12**(3), pp. 225–231. 38

[136] Maa, J. R., 1978. "Drop size distribution and heat flux of dropwise condensation." *The Chemical Engineering Journal,* **16**(3), pp. 171–176. 38, 66

[137] Abu-Orabi, M., 1998. "Modeling of heat transfer in dropwise condensation." *International Journal of Heat and Mass Transfer,* **41**(1), pp. 81–87. 38

[138] Gose, E. E., Mucciardi, A. N., and Baer, E., 1967. "Model for dropwise condensation on randomly distributed sites." *International Journal of Heat and Mass Transfer,* **10**(1), pp. 15–22. 39

[139] Mei, M., Hu, F., Han, C., and Cheng, Y., 2015. "Time-averaged droplet size distribution in steady-state dropwise condensation." *International Journal of Heat and Mass Transfer,* **88**, pp. 338–345. 39, 44

[140] Boroomandi Barati, S., Pionnier, N., Pinoli, J. C., Valette, S., and Gavet, Y., 2018. "Investigation spatial distribution of droplets and the percentage of surface coverage during dropwise condensation." *International Journal of Thermal Sciences,* **124**, pp. 356–365. 39, 44

[141] Fritter, D., Knobler, C. M., and Beysens, D. A., 1991. "Experiments and simulation of the growth of droplets on a surface (breath figures)." *Physical Review A,* **43**(6), pp. 2858–2869. 39

[142] Family, F., and Meakin, P., 1988. "Scaling of the droplet-size distribution in vapor-deposited thin-films." *Physical Review Letters,* **61**(4), pp. 428–431. 39

[143] Meakin, P., 1992. "Dropwise condensation: the deposition growth and coalescence of fluid droplets." *Physica Scripta,* **1992**(T44), pp. 31–41. 39

[144] Burnside, B. M., and Hadi, H. A., 1999. "Digital computer simulation of dropwise condensation from equilibrium droplet to detectable size." *International Journal of Heat and Mass Transfer,* **42**(16), pp. 3137–3146. 39

[145] Khandekar, S., and Muralidhar, K., 2014. "Dropwise condensation on inclined textured surfaces." *Dropwise Condensation on Inclined Textured Surfaces*, pp. 1–141. 39, 44, 51, 66

[146] Adhikari, S., Nabil, M., and Rattner, A. S., 2017. "Condensation heat transfer in a sessile droplet at varying Biot number and contact angle." *International Journal of Heat and Mass Transfer,* **115**, pp. 926–931. 41, 144

[147] Li, G., Alhosani, M. H., Yuan, S., Liu, H., Ghaferi, A. A., and Zhang, T., 2014. "Microscopic droplet formation and energy transport analysis of condensation on scalable superhydrophobic nanostructured copper oxide surfaces." *Langmuir,* **30**(48), pp. 14498–14511. 43, 44

[148] Kim, M.-K., Cha, H., Birbarah, P., Chavan, S., Zhong, C., Xu, Y., and Miljkovic, N., 2015. "Enhanced jumping-droplet departure." *Langmuir,* **31**(49), pp. 13452–13466. 43, 44

[149] Andrieu, C., Beysens, D. A., Nikolayev, V. S., and Pomeau, Y., 2002. "Coalescence of sessile drops." *Journal of Fluid Mechanics,* **453**, pp. 427–438. 44

[150] Roache, P. J., 1997. "Quantification of uncertainty in computational fluid dynamics." *Annual Review of Fluid Mechanics,* **29**(1), pp. 123–160. 49

[151] Rykaczewski, K., Scott, J. H. J., and Fedorov, A. G., 2011. "Electron beam heating effects during environmental scanning electron microscopy imaging of water condensation on superhydrophobic surfaces." *Applied Physics Letters,* **98**(9), p. 093106. 50

[152] Rykaczewski, K., and Scott, J. H. J., 2011. "Methodology for imaging nano-to-microscale water condensation dynamics on complex nanostructures." *ACS Nano,* **5**(7), pp. 5962–5968. 50

[153] Rykaczewski, K., 2012. "Microdroplet growth mechanism during water condensation on superhydrophobic surfaces." *Langmuir,* **28**(20), pp. 7720–7729. 50, 51

[154] Enright, R., Miljkovic, N., Dou, N., Nam, Y., and Wang, E. N., 2013. "Condensation on superhydrophobic copper oxide nanostructures." *Journal of Heat Transfer,* **135**(9), p. 091304. 50, 52, 88

[155] Graham, C., and Griffith, P., 1973. "Drop size distributions and heat-transfer in dropwise condensation." *International Journal of Heat and Mass Transfer,* **16**(2), pp. 337–346. 51, 62, 66

[156] Xu, Z., Zhang, L., Wilke, K., and Wang, E. N., 2018. "Multiscale dynamic growth and energy transport of droplets during condensation." *Langmuir,* **34**(30), pp. 9085–9095. 56, 65, 66, 101, 104

[157] Rose, J. W., 1967. "On the mechanism of dropwise condensation." *International Journal of Heat and Mass Transfer,* **10**(6), pp. 755–762. 62

[158] Liu, T., Sun, W., Sun, X., and Ai, H., 2010. "Thermodynamic analysis of the effect of the hierarchical architecture of a superhydrophobic surface on a condensed drop state." *Langmuir,* **26**(18), pp. 14835–14841. 70

[159] Liu, T. Q., Sun, W., Sun, X. Y., and Ai, H. R., 2012. "Mechanism study of condensed drops jumping on super-hydrophobic surfaces." *Colloids and Surfaces a-Physicochemical and Engineering Aspects,* **414**, pp. 366–374. 70

[160] Chen, X., Weibel, J. A., and Garimella, S. V., 2015. "Exploiting microscale roughness on hierarchical superhydrophobic copper surfaces for enhanced dropwise condensation." *Advanced Materials Interfaces,* **2**(3), p. 1400480. 70

[161] Hoenig, S. H., and Bonner, I. I. I. R. W., 2018. "Dropwise condensation on superhydrophobic microporous wick structures." *Journal of Heat Transfer,* **140**(7), pp. 071501–071501–7. 70

[162] Feng, J., Qin, Z., and Yao, S., 2012. "Factors affecting the spontaneous motion of condensate drops on superhydrophobic copper surfaces." *Langmuir,* **28**(14), pp. 6067–6075. 70

[163] Marr, K. M., Chen, B., Mootz, E. J., Geder, J., Pruessner, M., Melde, B. J., Vanfleet, R. R., Medintz, I. L., Iverson, B. D., and Claussen, J. C., 2015. "High aspect ratio carbon nanotube membranes decorated with pt nanoparticle urchins for micro underwater vehicle propulsion via h2o2 decomposition." *ACS Nano,* **9**(8), pp. 7791–7803. 73

[164] Song, J., Jensen, D. S., Hutchison, D. N., Turner, B., Wood, T., Dadson, A., Vail, M. A., Linford, M. R., Vanfleet, R. R., and Davis, R. C., 2011. "Carbon-nanotube-templated microfabrication of porous silicon-carbon materials with application to chemical separations." *Advanced Functional Materials,* **21**(6), pp. 1132–1139. 73

[165] Hutchison, D. N., Morrill, N. B., Aten, Q., Turner, B. W., Jensen, B. D., Howell, L. L., Vanfleet, R. R., and Davis, R. C., 2010. "Carbon nanotubes as a framework for high-aspect-ratio mems fabrication." *Journal of Microelectromechanical Systems,* **19**(1), pp. 75–82. 73

[166] Kass, M., Witkin, A., and Terzopoulos, D., 1988. "Snakes: Active contour models." *International Journal of Computer Vision,* **1**(4), pp. 321–331. 76

[167] Nam, Y., and Ju, Y. S., 2013. "A comparative study of the morphology and wetting characteristics of micro/nanostructured cu surfaces for phase change heat transfer applications." *Journal of Adhesion Science and Technology,* **27**(20), pp. 2163–2176. 88

[168] Dupeux, G., Bourrianne, P., Magdelaine, Q., Clanet, C., and Qur, D., 2014. "Propulsion on a superhydrophobic ratchet." *Scientific Reports,* **4**, pp. 5280–5280. 89

[169] Stevens, K. A., Crockett, J., Maynes, D. R., and Iverson, B. D., 2017. "An optical-based aggregate approach to measuring condensation heat transfer." In *Utah Space Grant Consortium Proceedings*. 93

[170] Weisensee, P. B., Wang, Y., Hongliang, Q., Schultz, D., King, W. P., and Miljkovic, N., 2017. "Condensate droplet size distribution on lubricant-infused surfaces." *International Journal of Heat and Mass Transfer,* **109**, pp. 187–199. 103

[171] Wasserfall, J., Figueiredo, P., Kneer, R., Rohlfs, W., and Pischke, P., 2017. "Coalescence-induced droplet jumping on superhydrophobic surfaces: Effects of droplet mismatch." *Physical Review Fluids,* **2**(12), p. 123601. 104

[172] Gao, S., Liao, Q., Liu, W., and Liu, Z., 2018. "Self-removal of multiple and multisize coalescing nanodroplets on nanostructured surfaces." *The Journal of Physical Chemistry C,* **122**(35), pp. 20521–20526. 104

[173] Wang, K., Li, R., Liang, Q., Jiang, R., Zheng, Y., Lan, Z., and Ma, X., 2017. "Critical size ratio for coalescence-induced droplet jumping on superhydrophobic surfaces." *Applied Physics Letters,* **111**(6), p. 061603. 104

[174] Adhikari, S., and Rattner, A. S., 2018. "Heat transfer during condensing droplet coalescence." *International Journal of Heat and Mass Transfer,* **127**, pp. 1159–1169. 106

[175] O'Hanlon, J. F., 2003. *A User's Guide to Vacuum Technology*., 3rd ed. John Wiley and Sons, Hoboken, New Jersey. 188

[176] National Aeronautics and Space Administration, 2018. Outgassing data for selecting spacecraft materials online. $< https://outgassing.nasa.gov/ >$. 188

APPENDIX A. CONTACT ANGLE MEASUREMENT

The following code was used to calculate the static, advancing, and receding contact angles reported in the dissertation. AngleMeasureMAIN.m is used for calculating the static contact angle, AngleMeasureVidMAIN.m is used for calculating the advancing and receding contact angles. ViewVid.m is used (before running AngleMeausreVidMain.m) to determine which frames to analyze and sliderbw.m and VideoSlider.m are functions called by the main scripts.

A.1 AngleMeasureMAIN.m

```
% Author: Kimberly Stevens
% email: kimst12@gmail.com
% June 2015; Last revision: 27-August-2015

%% User instructions:
% 1.) Take a picture of a droplet on a surface.  Make sure the droplet has a
% diameter less than 2.7 mm.  Make sure the edge rather than the center of
% droplet is in focus.
% 2.) Set the user defined values.  Imagepath aand imagename are pretty
% self-explanatory.  The variable thresh determines the threshold that is used
% to convert the image to binary.  This depends on the lighting of the image.
% If you are unsure which threshold to use, set the value to 1  and a window
% with variable thresholds will help you select the correct one.  The variable
% method allows the user to select how the
% tangent line is selected, as described below:
% 'manual' allows the user to define the line by
% manually picking the endpoints.  In this option the user is allow to pick
% as many tangent lines as desired.
% 'polynomial' has the user define a region on
```

```
% the drop by manually clicking at the top of the region.  The bottom of
% the region is defined by the base of the drop. The program then finds the
% left edge of the drop within that region and fits a 5th order polynomial
% to that edge, and uses the equation of the polynomial to define the tangent
% line.
% 'line' does the same thing as polynomial, but fits a line rather than a
% polynomial to the edge.  Therefore the edge that is used should be
% sufficiently small that the curvature of the droplet does not effect
% the line.
% 3.) Run the program.  The user is asked to crop the image and then manually
% draw a line at the base of the droplet.
%
% The code seems to be accurate to about +/- 3 degrees if used carefully.
% I personally like the polynomial method best.  The CA is relatively
% independent of threshold selected, within a reasonable range.  There is a
% section of code that plots CA as a function of threshold that you can
% uncomment.

close all
clear all
clc

%% Set User-Defined Values
imagepath=['J:\groups\biggy\goniometer\Jacob Butterfield\Stainless\2-20\'];
imagename='newDSC_00010005.jpg';
imageback=imagename;
method='polynomial'; %options are described below.
    % 'manual': to define the tangent line yourself
    % 'line': to fit a line to the left edge of the droplet
    % 'polynomial': to fit a polynomial to the left edge of the droplet
thresh=1; %set the threshold to convert the image; if set to 1, a slider
% function is called to assist the user in selecting the right threshold
subback=0; %set to 1 if you want to subtract the background image;
%% Open Image and crop
A=rgb2gray(imread([imagepath imagename]));
```

```
% frame=629;
% vidObj = VideoReader([cd '\12.8.15newSH\DSC_0009.mov'])
% vidWidth = vidObj.Width;
% vidHeight = vidObj.Height;
% numFrames = vidObj.NumberOfFrames;
% mov = struct('cdata',zeros(vidHeight,vidWidth,3,'uint8'),'colormap',[]);
% for k=1:frame
%     mov(k).cdata = read(vidObj,k);
% end
% I=rgb2gray(mov(frame).cdata);
% A=I;

if subback==1
    B=rgb2gray(imread([imagepath imageback]));
    C=(A-B)+(B-A);
    A=C;
end

imshow(A)
title('Click and drag to make box; then right click to crop')
[I,rect]=imcrop;
figure(1), imshow(I);

%% Threshold Image
if thresh==1
    sliderbw(I)
    thresh=input('What threshold value do you want to use?');
end
Ibw=im2bw(I,thresh);
figure(3), imshow(Ibw)
close(figure(1));

%% Find line for base of the droplet
title('Draw a line at the base of the droplet. (L to R for >90, % (line break)
R to L for <90)  Click and drag to move the end points. % (line break)
Double click when you are satisfied.')
```

```
h = imline;
position = wait(h);
xb=position(:,1);
yb=position(:,2);

if (strcmp(method,'line') || strcmp(method,'polynomial'))
    title('Select the upper limit of the region where you want % (line break)
    to look for an edge.')
    [xi, yi]=ginput(1);
    top=round(yi);
    bottomL=round(yb(1));
    bottomR=round(yb(2));
end

%% Look at effect of threshold--uncomment this section, and two more
% below (marked with asterisks)
% index=0;
% for t=thresh-.4:.01:thresh+.2
%     index=index+1;
%     tvect(index)=t;
%     Ibw=im2bw(I,t);
%% ************************************************************************

%% Find the edges of the droplet-----------------------------------------
if (strcmp(method,'line') || strcmp(method,'polynomial'))
    if subback ~=1
        Ibw=logical(abs(Ibw-1)); %invert the image so that the outline of
        % the drop is white and everything else is black
    end
    %left edge
    for j=top:bottomL
        for i=1:size(Ibw,2)
            if Ibw(j,i)==1
                xL(j)=i;
                break
            end
```

```
        end
    end
    yL=top:bottomL;
    xL=xL(top:bottomL);
    %right edge
    for k=top:bottomR
        for i=1:size(Ibw,2)
            if Ibw(k,size(Ibw,2)+1-i)==1
                xR(k)=size(Ibw,2)+1-i;
                break
            end
        end
        if xR(k)==size(Ibw,2) %stop searching if the it reaches the right
        % side of the image
            break
        end
    end
    yR=top:bottomR;
    xR=xR(top:bottomR);
end


%% Fit a curve-----------------------------------------------------------
if strcmp(method,'polynomial')
%     Code to fit a circle-------------
%     [xc yc R] = circfit(x,y); %least squares fit to a circle
%     viscircles([xc yc],R,'DrawBackgroundCircle',0) %draw the circle
%     xstar=xb(1);
%     ystar=yb(1);
%     dydx=(xstar-xc)/(R^2-(xstar-xc)^2)^.5; %calculate the slope of the
%     tangent vector


%   Instead fit a polynomial. Flip the x and y because otherwise it's not a
%   polynomial and doesn't fit well.  Sections which are commented out are
%   to calculate only one contact angle.
```

```
    % left side
    xstar=xL(end);
    ystar=yL(end);
    p=polyfit(yL,xL,5);
    xfit=polyval(p,yL);
    hold on
    plot(xfit,yL,'r','LineWidth',2)
    k=polyder(p); %take the derivative to find the slope.
%     m=polyval(k,ystar);
    dxdy=polyval(k,yL); %plug in a point to the derivative to calculate the
    % slope at that point
    dydx=-1./dxdy; %flip since we switched the x and y coordinates.
    lengx=40; %length of the vector that is drawn in the x direction
    yt=zeros(length(dxdy),2);
    yt(:,1)=ystar*ones(length(dxdy),1);
    yt(:,2)=(ystar-abs(dydx*lengx));

%     yt(1)=ystar;
%     yt(2)=ystar+dydx*lengx;
    xt(1)=xstar;
    if dydx(end)<0
        xt(2)=xstar-lengx;
    else
        xt(2)=xstar+lengx;
    end

    a=[xb(1)-xb(2),yb(1)-yb(2)];
%     b=[xt(1)-xt(2),yt(1)-yt(2)];
    b=[lengx*ones(length(dxdy),1),yt(:,1)-yt(:,2)];
    lenga=sqrt(sum(a.^2));
    lengb=(sum(b.^2,2)).^.5;
%     theta=180*acos(dot(a,b)/(lenga*lengb))/pi
    for i=1:length(dxdy)
        thetaL(i)=180*acos(dot(a,b(i,:))/(lenga*lengb(i)))/pi;
    end
    plot([xt(1) xt(2)],[yt(end,1) yt(end,2)],'g','LineWidth',2);
```

```
    %right side
    xstar=xR(end);
    ystar=yR(end);
    p=polyfit(yR,xR,5);
    xfit=polyval(p,yR);
    hold on
    plot(xfit,yR,'r','LineWidth',2)
    k=polyder(p); %take the derivative to find the slope.
    dxdy=polyval(k,yR); %plug in a point to the derivative to calculate the
    % slope at that point
    dydx=1./dxdy; %flip since we switched the x and y coordinates.
    lengx=40; %length of the vector that is drawn in the x direction
    yt=zeros(length(dxdy),2);
    yt(:,1)=ystar*ones(length(dxdy),1);
    yt(:,2)=(ystar-abs(dydx*lengx));
    xt(1)=xstar;
    if dydx(end)<0
        xt(2)=xstar+lengx;
    else
        xt(2)=xstar-lengx;
    end

    a=[xb(1)-xb(2),yb(1)-yb(2)];
    b=[lengx*ones(length(dxdy),1),yt(:,1)-yt(:,2)];
    lenga=sqrt(sum(a.^2));
    lengb=(sum(b.^2,2)).^.5;
    for i=1:length(dxdy)
        thetaR(i)=180*acos(dot(a,b(i,:))/(lenga*lengb(i)))/pi;
    end
    plot([xt(1) xt(2)],[yt(end,1) yt(end,2)],'g','LineWidth',2);

% *****Uncomment this line and comment the next three to look at the effect
    % of threshold*********************************************************
%     CA(index)=theta(end);
close(figure(2));
```

```
    figure, plot(xL,thetaL,xR,thetaR),xlabel('x position, pixels')
    ylabel('CA, in degrees'),legend('left','right')
    thetaL(end)
    thetaR(end)
%************************************************************************

end

% ********Uncomment next two lines to look at effect of threshold**********
% end
% figure, plot(tvect,CA),xlabel('threshold'),ylabel('CA, in degrees')
% ************************************************************************

%% To fit a line-----------------------------------------------------------
if strcmp(method, 'line')
    coeff=polyfit(xL,yL,1);
    yfit=polyval(coeff,xL);
    hold on
    plot(xL,yfit,'g','LineWidth',2)
    xt(1)=xL(end);
    xt(2)=xL(1);
    yt(1)=yfit(end);
    yt(2)=yfit(1);

    a=[xb(1)-xb(2),yb(1)-yb(2)];
    b=[xt(1)-xt(2),yt(1)-yt(2)];
    lenga=sqrt(sum(a.^2));
    lengb=sqrt(sum(b.^2));
    thetaL=180*acos(dot(a,b)/(lenga*lengb))/pi
    plot([xt(1) xt(2)],[yt(1) yt(2)],'g','LineWidth',2);
end

%% Define tangent line manually-------------------------------------------
if strcmp(method,'manual')
    keepgoing='y';
    title('Draw lines that are tangent to the edge of  % (line break)
```

```
    the drop at the triple point. Left then right. Start % (line break)
    at the base line and draw up.')
    g = imline;
    k = imline;
    while strcmp(keepgoing,'y')
        position = h.getPosition();
        xb=position(:,1);
        yb=position(:,2);
        a=[xb(1)-xb(2),yb(1)-yb(2)];

        position = g.getPosition();
        xt=position(:,1);
        yt=position(:,2);
        b=[xt(1)-xt(2),yt(1)-yt(2)];
        lenga=sqrt(sum(a.^2));
        lengb=sqrt(sum(b.^2));
        thetaLeft=180*acos(dot(a,b)/(lenga*lengb))/pi

        position = k.getPosition();
        xt=position(:,1);
        yt=position(:,2);
        b=[xt(1)-xt(2),yt(1)-yt(2)];
        lenga=sqrt(sum(a.^2));
        lengb=sqrt(sum(b.^2));
        thetaRight=180-180*acos(dot(a,b)/(lenga*lengb))/pi

        keepgoing=input('If you want to recalculate % (line break)
        the angles, move the lines and enter y.  Otherwise % (line break)
        hit any key to exit.','s');
    end
end
```

A.2 ViewVid.m

```
close all
```

```
clear all
clc

%% open video and save images in a struture.
vidObj = VideoReader(['J:\Taylor\SHS-CNT\8.29.16 CNTs Taylor\1-11,tran.mov'])
vidWidth = vidObj.Width;
vidHeight = vidObj.Height;
numFrames = vidObj.NumberOfFrames;
mov = struct('cdata',zeros(vidHeight,vidWidth,3,'uint8'),'colormap',[]);
for k=1:numFrames/2
    mov(k).cdata = read(vidObj,k);
%     imshow(mov(k).cdata)
%     title(num2str(k))
%     drawnow
end

Videoslider(mov,numFrames/2)
```

A.3 AngleMeasVidMAIN.m

```
close all
clear all
clc

%% Requirements
% Droplet and needle must be dark (backlit) and needle must be coming out
% of the top of the image.

%% User defined values--Use ViewVid to figure out what values to use here

baseFrame=30; % You want this to be the frame where the
% droplet is close to the largest it ever gets
startFrame=30;
endFrame=325;
backFrame=endFrame;
```

```
thresh=.3;
subback=0;
manbase=1;


%% open video and save images in a struture.
vidObj = VideoReader(['J:\groups\biggy\goniometer\KS\DSC_0052.mov']);
vidWidth = vidObj.Width;
vidHeight = vidObj.Height;
numFrames = vidObj.NumberOfFrames;
mov = struct('cdata',zeros(vidHeight,vidWidth,3,'uint8'),'colormap',[]);
for k=1:max(endFrame,backFrame)
    mov(k).cdata = read(vidObj,k);
%     imshow(mov(k).cdata)
%     title(num2str(k))
%     drawnow
end

% vidObjSAVE = VideoWriter('advancing.avi');
% open(vidObjSAVE);

%% Open user input image, crop, choose region to look for base, choose region
% to look for left and right edges
I=rgb2gray(mov(baseFrame).cdata);
if subback==1
    B=rgb2gray(mov(backFrame).cdata);
    C=(I-B)+(B-I);
    I=C;
end
figure, imshow(I)
title('Click and drag to make box; then right click to crop')
[I,rect]=imcrop;
figure, imshow(I);

%% Threshold Image
```

```
if thresh==1
    sliderbw(I)
    thresh=input('What threshold value do you want to use?');
end
Ibw=im2bw(I,thresh);
figure, imshow(Ibw)

%% Define the baseline, or where to look for one.
if manbase==1
    title('Draw a line at the base of the droplet.  Click and   % (line break)
    drag to move the end points. Double click when you are satisfied.')
    h = imline;
    position = wait(h);
    xbL=position(1,1);
    ybL=position(1,2);
    xbR=position(2,1);
    ybR=position(2,2);
else
    title('Click at the height of the upper region of the % (line break)
    image where the base of the droplet might be found.')
    [junk,ybaseupper]=ginput(1);
end

%% Define the region where the top of the curve will be.
title('Click once at the height of the top of the region where % (line break)
you want to look for the left edge, then the right.')
[junk,yedgeupper]=ginput(2);
figure, imshow(I);


for j=startFrame:endFrame
    I=rgb2gray(mov(j).cdata);
    if subback==1
        B=rgb2gray(mov(backFrame).cdata);
        C=(I-B)+(B-I);
        I=C;
```

```
    end
    I=imcrop(I,rect);
    Ibw=im2bw(I,thresh);
    if subback==1
        Ibw=bwconvhull(Ibw,'objects');
        Ibw=bwconvhull(Ibw,'objects');
        Ibw=logical(abs(Ibw-1));
    end
    imshow(I), title(num2str(j))

    % Look for left edge
    for k=1:size(Ibw,1)
        for i=1:size(Ibw,2)
            if Ibw(k,i)==0
                xL(k)=i;
                break
            else
                xL(k)=0;
            end
        end
        if xL(k)==1 %stop searching if the left side runs into
        % the left side of the image
            break
        end
    end
    yL=1:length(xL);

%     % Check for errant points
%     diffxL=diff(xL);
%     for i=1:length(xL)-2
%         if diffxL(i)>100
%             if diffxL(i+1)<100
%                 xL(i+1)=(xL(i)+xL(i+2))/2;
%             end
%         end
%         if diffxL(i)<100
```

```
%             if diffxL(i+1)>100
%                 xL(i+1)=(xL(i)+xL(i+2))/2;
%             end
%         end
%     end

    if manbase ~=1
        %Find the left base
        yLseekbase=yL(round(ybaseupper):end); %looks for the base
        % below the user defined point.
        xLseekbase=xL(find(yL==round(ybaseupper)):end);
        ybL=round(find(xLseekbase==max(xLseekbase),1))+ybaseupper-1; %finds
        % the furthest most left point and calls that the left point.
        xbL=max(xLseekbase);
    end


    % Find the left edge of the droplet above the base
    yLdrop=yL(round(yedgeupper(1)):round(ybL));
    xLdrop=xL(find(yL==round(yedgeupper(1))):find(yL==round(ybL)));

    %Find the left tangent line
    xstar=xLdrop(end); %one point on the tangent line--corresponds to the
    % end of the base line.  It's also the point where the edge
    % intersects the base.
    ystar=yLdrop(end);
    p=polyfit(yLdrop,xLdrop,5);
    xfit=polyval(p,yLdrop);
    hold on
    plot(xfit,yLdrop,'r','LineWidth',2)
    k=polyder(p); %take the derivative to find the slope.
    m=polyval(k,ystar); %plug in a point to the derivative to calculate
    % the slope at that point
    dydx=-1./m; %flip since we switched the x and y coordinates.
    lengx=40; %length of the vector that is drawn in the x direction
    ytL(1)=ystar;
```

```
    ytL(2)=ystar+dydx*lengx;
    xtL(1)=xstar;
    xtL(2)=xstar-lengx;


    % Look for right edge
    for k=1:size(Ibw,1)
        for i=1:size(Ibw,2)
            if Ibw(k,size(Ibw,2)+1-i)==0
                xR(k)=size(Ibw,2)+1-i;
                break
            else
                xR(k)=0;
            end
        end
        if xR(k)==size(Ibw,2) %stop searching if it reaches the left
        % side of the image
            break
        end
    end
    yR=1:length(xR);

%     % Check for errant points
%     diffxR=diff(xR);
%     for i=1:length(xR)-2
%         if diffxR(i)>100
%             if diffxR(i+1)<100
%                 xR(i+1)=(xR(i)+xR(i+2))/2;
%             end
%         end
%         if diffxR(i)<100
%             if diffxR(i+1)>100
%                 xR(i+1)=(xR(i)+xR(i+2))/2;
%             end
%         end
%     end
```

```
if manbase~=1
    %Find the right base
    yRseekbase=yR(round(ybaseupper):end);
    xRseekbase=xR(find(yR==round(ybaseupper)):end);
    ybR=round(find(xRseekbase==min(xRseekbase),1))+ybaseupper-1;
    xbR=min(xRseekbase);
end

% Find the right edge of the droplet
yRdrop=yR(round(yedgeupper(2)):round(ybR));
xRdrop=xR(find(yR==round(yedgeupper(2))):find(yR==round(ybR)));

%Find the right tangent line
xstar=xRdrop(end);
ystar=yRdrop(end);
p=polyfit(yRdrop,xRdrop,5);
xfit=polyval(p,yRdrop);
plot(xfit,yRdrop,'r','LineWidth',2)
k=polyder(p); %take the derivative to find the slope.
m=polyval(k,ystar); %plug in a point to the derivative to calculate
% the slope at that point
dydx=1./m; %flip since we switched the x and y coordinates.
lengx=40; %length of the vector that is drawn in the x direction
ytR(1)=ystar;
ytR(2)=ystar+dydx*lengx;
xtR(1)=xstar;
xtR(2)=xstar+lengx;

% Find left and right contact angles
a=[xbL-xbR,ybL-ybR];
lenga=sqrt(sum(a.^2));

bL=[xtL(1)-xtL(2),ytL(1)-ytL(2)];
lengbL=(sum(bL.^2,2)).^.5;
thetaL(j)=180*acos(dot(a,bL)/(lenga*lengbL))/pi;
```

```
    bR=[xtR(1)-xtR(2),ytR(1)-ytR(2)];
    lengbR=(sum(bR.^2,2)).^.5;
    thetaR(j)=180-180*acos(dot(a,bR)/(lenga*lengbR))/pi;

    plot(xL,yL,'w',xR,yR,'w')
    plot([xbL xbR],[ybL ybR],'b','LineWidth',2);
    plot([xtL(1) xtL(2)],[ytL(1) ytL(2)],'g','LineWidth',2);
    plot([xtR(1) xtR(2)],[ytR(1) ytR(2)],'g','LineWidth',2);
    plot([1 size(Ibw,2)],[yedgeupper(2) yedgeupper(2)],'y','LineWidth',2);
    plot([1 size(Ibw,2)],[yedgeupper(1) yedgeupper(1)],'y','LineWidth',2);
    drawnow

%     M(i) = getframe;
%     currFrame = getframe;
%     writeVideo(vidObjSAVE,currFrame);

    % Calculate the area of the drop
    xLarea=xL(1:min(find(yL==round(ybL)),find(yR==round(ybR))));
    xRarea=xR(1:min(find(yL==round(ybL)),find(yR==round(ybR))));
    width=xRarea-xLarea;
    area(j)=sum(width);
%     waitforbuttonpress
end

xvect=startFrame:endFrame;
figure,
[ax,p1,p2]=plotyy([xvect',xvect'],[thetaL(xvect)',% (line break)
thetaR(xvect)'],xvect,area(xvect))
xlabel('Frame number')
ylabel(ax(1),'CA in degrees')
ylabel(ax(2),'Area in pixels')
legend('CA left','CA right','area')

% close(vidObjSAVE);
 points=[xvect; thetaL(xvect); thetaR(xvect); area(xvect)];
```

```
 save('results','points')
```

A.4 sliderbw.m

```
function sliderbw(im)
%SLIDER Allows to the user to see how changing the threshold changes the
%binary image.
%Kim Stevens, kimst12@gmail.com

    hFig = figure('menu','none');
    hAx = axes('Parent',hFig);
    uicontrol('Style', 'slider', 'Value', .6, 'Position', % (line break)
    [150 5 300 20], 'Callback', @sliderCallback);
    T=.5;
    imbw=im2bw(im,T);
    imshow(imbw,'Parent',hAx), title('Choose threshold by using slider.')

    function sliderCallback(hObject, evt)
    T=get(hObject, 'Value');
    imbw=im2bw(im,T);
    subplot(222),imshow(imbw), title(['Threshold: ' num2str(T)])
    subplot(221), imshow(im), title('Original Image')
    maskIm=im.*uint8(imbw);
    maskImB=im.*uint8(~imbw);
    subplot(223), imshow(maskIm), title('Threshold superimposed on original')
    subplot(224), imshow(maskImB), title('Inverse')
    end

end
```

A.5 Videoslider.m

```
function Videoslider(mov,endFrame)
%VIDEOSLIDER Allows a user to scroll through a video
```

```
%Kim Stevens, kimst12@gmail.com

    hFig = figure('menu','none');
    hAx = axes('Parent',hFig);
    uicontrol('Style', 'slider', 'Value',endFrame, 'Callback', % (line break)
    @sliderCallback, 'Position',[150 5 300 20], 'Max',endFrame % (line break)
    ,'Min',1,'SliderStep',[1 1]/(endFrame));
    T=endFrame;
    imshow(mov(T).cdata,'Parent',hAx),
    title('Use slider to scroll through video')

    function sliderCallback(hObject, evt)
        T=round(get(hObject, 'Value'));
        imshow(mov(T).cdata)
        title(num2str(T))
    end
end
```

APPENDIX B. CONDENSATION SIMULATION CODE

The following code is used to simulate condensation on superhydrophobic surfaces, as described in chapter 4. The main file is Numerical_v8.m. It calls the following functions.

- XSteam.m can be downloaded from the Matlab file exchange at https://www.mathworks.com/matlabcentral/fileexchange/9817-x-steam-thermodynamic-properties-of-water-and-steam.
- fCalculator.m can be downloaded at the link provided in Adhikari et al. [146].
- Chavan.m is included below.
- Input_Param.m is included below.

The distribution function can be built using the script binning.m. An example using binning.m is given in PlotDistribution.m. When formatting the code to fit into the format of this dissertation it was occasionally necessary to break long lines of code with a hard return. When a hard return was used, a commented out section that indicates such, "% (line break)", is included at the location of the hard return.

B.1 Numerical_v8.m

```
close all
clear all
clc
fontsize=10;
fontname='Times';

%% USER DEFINED CONDITIONS
```

```
savename=('example');
savefrq=1e7;
% set up the time domain
dt=2e-5; % time step in seconds
tf=4;
t=0:dt:tf;

%set up the spatial domain
H=8e-5;
W=H;

heatTransferModel='A'; %A for Adhikari, C for Chavan,
%K for Kim, M for Miljkovic
nucleationtype=1; %1 randomly re-distributed, 0 for
%preferential nucleation cites that don't change.
jumpingmodel=0; %0: no jumping; 1: all coalescence result in jumping;
% 2: no coalescence, disappears at r=re;
% 3: no coalescence til r=re; 4: jumping for drops > rminj
rminj=0;
loss=0;

% operating conditions
Ns=1e11;% initial nucleation density
Tsat=22+273;
dT=1;
thetaa=165;
thetar=165;
thetae=acosd(0.5*cosd(thetar)+0.5*cosd(thetaa));
theta=thetaa;

% Properties and derivative parameters
[nug,hfg,kw,rhow,sig,g,Rg,alph,Ts,hi,rmin] = Input_Param(Tsat,dT);

re=1/(4*sqrt(Ns)); % Miljkovic equation for re
rsmallest=rmin;
% RMAX=(6*(cosd(thetar)-cosd(thetaa))*sind(thetae) % (line break)
```

```
%*sig/(pi*(2-3*cosd(thetae)+cosd(thetae)^3)*rhow*g))^.5;
RMAX=2e-5;

%% END USER DEFINED CONDITIONS
% distribute initial nucleation cites
N=round(Ns*H*W);
numskip=max(1,round(tf*N/(dt*1e7)));
x=W*rand(1,N);
y=H*rand(1,N);
xo=x;
yo=y;
r=rsmallest*ones(size(x));

swp_ctr=0;
ctr=0;
rcctr=0;
Qtotsim=0;
maxr=zeros(size(t));
avgr=zeros(size(t));
Qvect=zeros(size(t));
percA=zeros(size(t));
numdrop=zeros(size(t));
rc=zeros(1,3e5);

% drop=struct('x',x,'y',y,'r',r);
drop(floor((length(t)-1)/numskip)).x=zeros(size(x));
drop(floor((length(t)-1)/numskip)).y=zeros(size(x));
drop(floor((length(t)-1)/numskip)).r=zeros(size(x));

if strcmp('A',heatTransferModel) %https://www.sciencedirect.com
% /science/article/pii/S0017931017306786#b0085
    HTM=1;
    rA=logspace(log10(rsmallest),log10(RMAX),2000);
    for d=1:length(rA)
        Bi=hi*rA(d)/kw;
        f = fCalculator(Bi, thetaa);
```

```
        Q(d)=dT*pi*rA(d)^2*sind(thetaa)^2/(f*rA(d)/kw+1/(2*hi));
    end
    rl=log(rA);
    Ql=log(Q);
    pl=polyfit(rl,Ql,5);
    CFErr=(Q-exp(polyval(pl,rl)))./Q;
    disp(['Maximum error due to curve fitting is ' num2str(max(CFErr))])
    if CFErr>.02
        disp('CF Error is greater than 2 percent.  Continue with simulation?')
        waitforbuttonpress
    end
elseif strcmp('C',heatTransferModel)
    HTM=2;
elseif strcmp('K',heatTransferModel)
    HTM=3;
    A1=dT/(2*rhow*hfg);
    A2=theta*(pi/180)*(1-cosd(theta))/(4*kw*sind(theta));
    A3=1/(2*hi) + delta*(1-cosd(theta))/(kcoat*sind(theta)^2);
elseif strcmp('M',heatTransferModel)
    A1=dT/(hfg*rhow*(1-cosd(theta))^2*(2+cosd(theta)));
    A2=theta*(pi/180)/(4*kw*sind(theta));
    % A3=1/(2*hi*(1-cosd(theta)))+1/(kHC*sind(theta)^2) % line (break)
    *[kP*phi/(deltaHC*kP+h*kHC)+kw*(1-phi)/(deltaHC*kw+h*kHC)]^(-1);
    A3=1/(2*hi*(1-cosd(theta)));
    HTM=4;
else
    disp('Not a valid HT model')
end

if jumpingmodel==3
    r_coal_lim=re;
else
    r_coal_lim=0; %it's important to keep this expression b/c this way the
    %simulation only tries to coalesce drops that exist, i.e. that are
    %greater than 0
end
```

```
for tstep=2:length(t)
   %% grow the drop
    for d=1:size(x,2)
        if r(d)>0
            if HTM==1 % Adhikari
                Q=exp(polyval(pl,log(r(d))));
            elseif HTM==2 % Chavan 2016
                Bi=hi*r(d)*sind(thetaa)/kw;
                [Nu] = Chavan(Bi,thetaa*pi/180);
                Q=Nu*kw*r(d)*sind(thetaa)*(Tsat-Ts);
            elseif HTM==3 % Kim and Kim (eqn 15)
                Q=pi*dT*r(d)*(r(d)-rmin)*(1-cosd(theta))/(A2*r(d)+A3);
            elseif HTM==4 %Miljkovic 2013 Modeling (eqn 13)
                Q=pi*dT*r(d)*(r(d)-rmin)/(A2*r(d)+A3);
            end
            %% all
            Qtotsim=Qtotsim+Q;
            dV=Q*dt/(rhow*hfg);
            V=pi*r(d)^3*(2-3*cosd(theta)+cosd(theta)^3)/3+dV;
            % for a spherical cap
            r(d)=(3*V/(pi*(2-3*cosd(theta)+cosd(theta)^3)))^(1/3);
        end
    end

    %% check for coalesence
    for d=1:size(x,2)
        if jumpingmodel==2
            if r(d)>re
                r(d)=0;
                x(d)=W;
                y(d)=H;
            end
        else
            if r(d)>r_coal_lim % if this drop has already been deleted,
            % skip it.
```

```
dist=((x(d)-x).^2+(y(d)-y).^2+(r(d)-r).^2 % (line break)
*cosd(theta)^2).^(.5)-r-r(d);   % distance between drop d and
% every other drop, minus the radius of that drop
indc=find(dist<0);
indc(find(indc==d))=[]; %remove the 0 one.
if jumpingmodel==3
    rpot=r(indc);
    indc(find(rpot<re))=[]; % don't coalesce drops drops
    % that are less than re
end
if ~isempty(indc)
    if jumpingmodel==0 || jumpingmodel==3
        for i=1:length(indc)
            rc(rcctr+1:rcctr+length(indc)+1)=[r(d) r(indc)];
            rcctr=length(nonzeros(rc));
            x(d)=(r(d)^3*x(d)+r(indc(i))^3* % line (break)
            x(indc(i)))/(r(d)^3+r(indc(i))^3);
            %new drop @ COM (Barati 2018 Cha2016)
            y(d)=(r(d)^3*y(d)+r(indc(i))^3*y % line (break)
            (indc(i)))/(r(d)^3+r(indc(i))^3);
            r(d)=(r(d)^3+r(indc(i))^3)^(1/3);
        end
    elseif jumpingmodel==1
            rc(rcctr+1:rcctr+length(indc)+1)=[r(d) r(indc)];
            rcctr=length(nonzeros(rc));
        x(d)=W;
        y(d)=H;
        r(d)=0;

    elseif jumpingmodel==4
        for i=1:length(indc)
           dist=((x(indc(i))-x).^2+% (line break)
           (y(indc(i))-y).^2+% (line break)
           (r(indc(i))-r).^2*cosd(theta)^2).^(.5)%(line break)
           -r-r(indc(i));
            % check for coalescence between the secondary
```

```
                    % drops and all other drops
                    newindc=find(dist<0);
                    newindc(find(newindc==indc(i)))=[]; %remove the
                    % 0 one.
                    newindc(find(newindc==d))=[]; %remove the 0 one.
                    if ~isempty(indc)
                        indc=[indc newindc];
                    end
                end

                if length(find([r(d) r(indc)]>rminj,2))==2
                    % to have it leave
                    x(d)=W;
                    y(d)=H;
                    r(d)=0;
                else
                    % to have it stay
                    x(d)=(r(d)^3*x(d)+sum(r(indc).^3% line break)
                    .*x(indc)))/(r(d)^3+sum(r(indc).^3));
                    %new drop @ COM (Barati 2018, Cha2016)
                    y(d)=(r(d)^3*y(d)+sum(r(indc).^3% line break)
                    .*y(indc)))/(r(d)^3+sum(r(indc).^3));
                    r(d)=(r(d)^3+sum(r(indc).^3))^(1/3);
                end
            else
                disp('you havent done your logic right')
            end

            %the other ones always depart
            x(indc)=W;
            y(indc)=H;
            r(indc)=0;
        end % if indc isn't empty
    end
end
end
```

```
    %% check for sweeping
    for d=1:size(x,2)
        if r(d)>RMAX
% %visualize before sweeping
% figure(3), cla
% viscircles([x; y]', r','LineWidth',.5,'Color','r');
% viscircles([x(d); y(d)]', r(d)*sind(theta)','LineWidth',.5,'Color','g');
% hold on
% plot([x(d)-r(d)*sind(theta) x(d)-r(d)*sind(theta)], [0 y(d)],'k--')
% plot([x(d)+r(d)*sind(theta) x(d)+r(d)*sind(theta)], [0 y(d)],'k--')
% axis square;
% xlim([0 W]);
% ylim([0 H]);
            for d2=1:size(x,2)
                if abs(d-d2)>0 %skip the case when d=d2
                    % only look at drops below the midpoint of the sweeper
                    if y(d2)<y(d)
                        % to remove drops which would coalesce during sweeping
                        dist=((x(d)-x(d2)).^2+(r(d)-r(d2)). % (line break)
                        ^2*cosd(theta)^2).^(.5)-r(d)-r(d2);
                        if dist<0
                       % visualize every drop before it's swept
% figure(3), plot(x,y,'.');
% viscircles([x; y]', r');
% hold on
% plot([x(d)-r(d) x(d)+r(d)], [y(d) y(d)],'k')
% plot([x(d)-r(d) x(d)-r(d)], [0 y(d)],'k')
% plot([x(d)+r(d) x(d)+r(d)], [0 y(d)],'k')
% viscircles([x(d2) y(d2)], r(d2),'Color','g');
% axis square;
% xlim([0 W]);
% ylim([0 H]);
% hold off
% waitforbuttonpress
                            x(d2)=W;
```

```
                        y(d2)=H;
                        r(d2)=0;
                    end
                end
            end
        end

        x(d)=W;
        y(d)=H;
        r(d)=0;
        swp_ctr=swp_ctr+1;
        disp(['swp ctr=' num2str(swp_ctr)])
        % %visualize the drops that are left
% viscircles([x; y]', r','Color','b','LineWidth',.5);
% hold on
% axis square;
% xlim([0 W]);
% ylim([0 H]);
% hold off
% set(gca,'FontSize',fontsize,'FontName',fontname);
% set(gcf,'PaperPosition',[1 1 3 3]);
% set(gcf, 'Units', 'Inches', 'InnerPosition', [2 5 3 3]);
% print('-depsc','-r300',[cd '\figures\sweepinga']);
% print('-dpng','-r300',[cd '\figures\sweepinga']);
%
% figure(4), cla
% viscircles([x; y]', r','Color','b','LineWidth',.5);
% hold on
% axis square;
% xlim([0 W]);
% ylim([0 H]);
% hold off
% set(gca,'FontSize',fontsize,'FontName',fontname);
% set(gcf,'PaperPosition',[1 1 3 3]);
% set(gcf, 'Units', 'Inches', 'InnerPosition', [7 5 3 3]);
% print('-depsc','-r300',[cd '\figures\sweepingb']);
```

```
% print('-dpng','-r300',[cd '\figures\sweepingb']);
% waitforbuttonpress
        end
    end
    %% check for new nucleation
    if nucleationtype==1
        egg=sortrows([x; y; r]'); %put all the L's to the back.
        x=egg(:,1)';
        y=egg(:,2)';
        r=egg(:,3)';

        indd=find(x==W,1); %find where the end of the drops are

        % make new nucleation cites
        A=sum(pi*r.^2*sind(theta)^2);
        n_old=length(nonzeros(r));
        n_new=round((Ns-n_old/(W*H))*((W*H)-A)); %calculate the #
        % of new nucleation cites
        if n_new>0
            cntrsnew=zeros(2,n_new);
            while n_new>0
                cntrsnew(2,1:n_new)=W*rand(1,n_new);
                cntrsnew(1,1:n_new)=H*rand(1,n_new);
                for i=1:size(cntrsnew,2)
                    egg=((cntrsnew(2,i)-x).^2+ % (line break)
                    (cntrsnew(1,i)-y).^2+(rsmallest-r).^2* % (line break)
                    cosd(theta)^2).^(.5)-(r+rsmallest);
                    % distance between new drop and every other drop,
                    % minus the radius of the new drop and every other drop
                    if min(egg)<0
                        cntrsnew(:,i)=[0;0];
                    end
                end
                cntrsnew=sortrows(cntrsnew')';
                n_new=size(cntrsnew,2)-length(nonzeros(cntrsnew))/2;
            end
```

```
            x(indd:indd+size(cntrsnew,2)-1)=cntrsnew(2,:);
            y(indd:indd+size(cntrsnew,2)-1)=cntrsnew(1,:);
            r(indd:indd+size(cntrsnew,2)-1)=rsmallest;
        end
    else % preferential nucleation cites--x and y stay the same throughout
    % the simulation; nucleation occurs whenever one of the original
    % cites is uncovered
       for d=1:size(xo,2)
           dist=((xo(d)-x).^2+(yo(d)-y).^2+(rsmallest-r). % (line break)
           ^2*cosd(theta)^2).^(.5)-r-rsmallest;
           if min(nonzeros(dist))>0 %cite is uncovered
               ind=find(r==0,1);
               if min(r)~=0
                   r(end+1)=rsmallest;
                   x(end+1)=xo(d);
                   y(end+1)=yo(d);
               else
                   r(ind)=rsmallest;
                   x(ind)=xo(d);
                   y(ind)=yo(d);
               end
% %visualize
% cla
% viscircles([x; y]', r','Color','b');
% viscircles([x; y]', r'*sind(theta),'Color','g');
% hold on
% viscircles([x(ind); y(ind)]', r(ind)','Color','r');
% axis square;
% xlim([x(ind)-20*r(ind) x(ind)+20*r(ind)]);
% ylim([y(ind)-20*r(ind) y(ind)+20*r(ind)]);
% hold off
% waitforbuttonpress
           end
       end
    end
```

```
    %% save results from this time step
    if mod(tstep,numskip)==0
        ctr=ctr+1;
        disp(['time step: ' num2str(tstep)])
        % save the data from this time step
        drop(ctr).x=x;
        drop(ctr).y=y;
        drop(ctr).r=r;
    end
    avgr(tstep)=mean(nonzeros(r));
    maxr(tstep)=max(r);
    Qvect(tstep)=Qtotsim-sum(Qvect);
    percA(tstep)=sum(pi*r.^2*sind(theta)^2)/(W*H);
    numdrop(tstep)=length(nonzeros(r));
   if mod(tstep,savefrq)==0
       save(savename)
       disp('-------saved-------------')
   end

%       % visulalize
%     figure(3), cla
%     viscircles([x; y]', r','LineWidth',.5);
%     viscircles([x; y]', r'*sind(theta),'LineWidth',.5,'Color','b');
% %     viscircles([x(find(r<re)); y(find(r<re))]', % (line break)
% r(find(r<re))','LineWidth',.5,'Color','g');
%     axis square;
%     xlim([0 W]);
%     ylim([0 H]);

end

allr=[drop(:).r];
disp([num2str(swp_ctr) ' ' num2str(max(allr))])
disp(['q" from sim is ' num2str(Qtotsim*dt/(tf*W*H))])
if HTM==1
```

```
    disp(['Maximum error due to curve fitting is' num2str(max(CFErr))])
end
save(savename)

%% if running in GUI:
if HTM==1
    figure, semilogx(rA,100*CFErr)
    ylabel('% Error due to the curve fit')
    xlabel('drop size')
end

%% plot results over time:
q=Qvect/(W*H);
for i=1:length(q)
    qmean(i)=mean(q(1:i));
end
figure,
[ax]=plotyy(t,q,t,100*(qmean-mean(q))/mean(q));
ylim(ax(2),[-5 5])
ylabel(ax(2),'% Change')
ylabel(ax(1),'q" (W/m^2)')
xlabel('time (s)')

%% plot other stuff
if exist('drop','var')
    if ~exist('percA','var')
        for d=1:size(drop,2)
            percA(d)=sum(drop(d).r.^2*pi*sind(theta)^2)/(W*H);
        end
    end
end
figure, subplot(211), ax=plotyy(t,avgr, t, maxr);
ylabel(ax(1),'average drop radius, m')
ylabel(ax(2), 'max drop radius, m'),xlabel('time, s')
subplot(212), ax=plotyy(t,numdrop,t,percA);
ylabel(ax(1),'number of drops'), ylabel(ax(2),'A_b/A_{tot}')
```

```
figure, plot(t,Qvect/(W*H)), ylabel('q", W/m^2'), xlabel('time, s')
disp(['average drop radius: ' num2str(mean(avgr))])
disp(['average N: ' num2str(mean(numdrop)/(W*H),'%10.3e')])
disp(['average percent of area covered by drops: ' num2str(mean(percA))])
plotyes=1;
binning;

%% max sizes
for i=1:length(drop)
    rt=sort(nonzeros(drop(i).r),'descend');
    rm1(i)=rt(1);
    rm5(i)=mean(rt(1:5));
    rm10(i)=mean(rt(1:10));
    rm100(i)=mean(rt(1:100));
    rm(i)=mean(rt);
end
t2=(1:length(drop))*dt*numskip;
figure, ax=plotyy(t2,[rm1; rm5; rm10; rm100],t2,rm);
ylabel('radius (m)')
ylabel(ax(2),'mean radius (m)')
xlabel('time (s)')
legend('max','top5','top10','top100','mean')
```

B.2 Input_Param.m

```
function [nug,hfg,kw,rho,sig,g,Rg,alph,Ts,hi,rmin] = Input_Param(Tsat,dT)
% Properties
nug = XSteam('vV_T',Tsat-273); % m3/kg specific volume of water vapour
hfg = (XSteam('hV_T',Tsat-273)-XSteam('hL_T',Tsat-273))*1000; % J/kg
%latent heat of vaporization
kw = XSteam('tcL_T',Tsat-273);  % W/m.K conductivity of water
rho = XSteam('rhoL_T',Tsat-273); % kg/m3 Demsity of water
sig = XSteam('st_T',Tsat-273);   % N/m surface tension of water

% constants
```

```
g=9.81;
Rg=461.5; %J/kgK specific gas constant
alph=1;

Ts=Tsat-dT;

% in their modeling paper, they use Ts, not Tsat
hi=2*alph*hfg^2/((2-alph)*sqrt(2*pi*Rg*Tsat)*nug*Tsat);
% from http://heattransfer.asmedigitalcollection.asme.org/article.aspx?
%articleid=1742210
% hi = (8*alpha/(2-0.798*alpha))*((gamma-1)/(gamma+1))*
% (1/sqrt(2*pi*Rc*Ts))*(hfg^2)/(vg*Tsat);
% from Rose Heat transfer coefficient - On Interphase Matter Transfer,
%the Condensation Coefficient and Dropwise Condensation (1987), eqn 7

rmin=2*Tsat*sig/(hfg*rho*dT); %Van Carey eqn 9.21 uses Ts;
% Miljkovic and Kim uses Tsat
```

B.3 Chavan.m

```
function [Nu] = Chavan(Bi,thetaa)
%CHAVAN Calculate the Nu for heat transfer to an individual drop from Bi,
% thetaa [RADIANS!!], based on the fit.  Based on numerical simulations
% from Chanvan et al. in Heat Transfer through a Condensate Droplet on
% Hydrophobic and Nanostructured Superhydrophobic Surfaces
%   https://pubs.acs.org/doi/full/10.1021/acs.langmuir.6b01903
if Bi<=0.5
    Nu=3*thetaa.^.65*Bi^.83+0.007*thetaa.^5.1*Bi^(-0.23);
elseif Bi<=2
    Nu=0.29*thetaa.^2.24*Bi^(-.17)+3.33*thetaa.^(-.3)*Bi^0.72;
elseif Bi<=10e5
    Nu=5.76*exp(-.28*thetaa.^.68)*log(1+5*Bi^0.82-2.79*Bi^.83);
else
    disp('Bi too high!')
    Nu=0;
```

```
end
end
```

B.4 PlotDistributionDEMO.m

```
close all
clear all

filename1='filename';
load(filename)
plotyes=1;
binning
r_bina=r_bin;
r_binla=r_binl;
r_binra=r_binr;
na=n;

%% fancy error bars
figure,
loglog(r_bina,na,'r-')
hold on
fill([r_binla';flipud(r_binra')],[na';flipud(na')], % (line break)
'r','linestyle','none');
alpha(0.1)

p1=loglog(r_binla,na,'r-.');
p1.Color(4) = 0.25;
p1=loglog(r_binra,na,'r-.');
p1.Color(4) = 0.25;

xlabel('{\it r} (m)')
ylabel('{\it N} (drops/m^3)')
```

B.5 binning.m

```
percchange=1e-2;
trans=5e-6;

ylim1=1e11;
ylim2=1e18;
xlim1=1e-8;
xlim2=1e-3;

if ~exist('ctr','var')
    ctr=length(t);
end

if plotyes==1
    % traditional bins
    rhist10=logspace(log10(min(nonzeros(allr))),log10(max(allr)),10);
    nhist10=histcounts(allr,rhist10)/((W*H)*ctr);
    ncntr10=nhist10./diff(rhist10);
    rcntr10=0.5*(rhist10(1:end-1)+rhist10(2:end));
    rcntr10l=rhist10(1:end-1);
    rcntr10r=rhist10(2:end);
end

%% bins based on dr increments
r_bin_e=min(nonzeros(allr));
i=1;
if ~exist('HTM')
    if exist('Bi','var')
        HTM=2;
        disp('Heat transfer model is Chavan')
    else
        HTM=4;
        disp('Heat transfer model is Miljkovic')
    end
end
while r_bin_e(i)<trans
    i=i+1;
```

```
    if HTM==1 % Adhikari
        Bi=hi*r_bin_e(i-1)/kw;
        f = fCalculator(Bi, thetaa);
        Q=dT*pi*r_bin_e(i-1)^2*sind(thetaa)^2/(f*r_bin_e(i-1)/kw+1/(2*hi));
        if exist('pl','var')
          Q=exp(polyval(pl,log(r_bin_e(i-1))));
        end
    elseif HTM==2 % Chavan 2016
        Bi=hi*r_bin_e(i-1)*sind(thetaa)/kw;
        [Nu] = Chavan(Bi,thetaa*pi/180);
        Q=Nu*kw*r_bin_e(i-1)*sind(thetaa)*(Tsat-Ts);
    elseif HTM==3 % Kim and Kim (eqn 15)
        Q=pi*dT*r_bin_e(i-1)*(r_bin_e(i-1)-rmin)*(1-cosd(theta))/(A2*r(d)+A3);
    elseif HTM==4 %Miljkovic 2013 Modeling (eqn 13)
        Q=pi*dT*r_bin_e(i-1)*(r_bin_e(i-1)-rmin)/(A2*r_bin_e(i-1)+A3);
    end
    dV=Q*dt/(rhow*hfg);
    V=pi*r_bin_e(i-1)^3*(2-3*cosd(theta)+cosd(theta)^3)/3+dV;
    r_bin_e(i)=(3*V/(pi*(2-3*cosd(theta)+cosd(theta)^3)))^(1/3);
end

histK=histcounts(allr,r_bin_e);
n_dr=histK./(diff(r_bin_e)*W*H*ctr);
r_dr=0.5*(r_bin_e(1:end-1)+r_bin_e(2:end));

allr=sort(allr);

% determine the transition by the percentage of change in drop radius
%(once the diff starts decreasing)
indmax=find(diff(r_bin_e)==max(diff(r_bin_e)));
if min(diff(r_bin_e(indmax:end))./r_bin_e(indmax:end-1))<percchange
    ind=find(diff(r_bin_e(indmax:end))./r_bin_e(indmax:end-1)<percchange,1);
    r_bin_e=r_bin_e(1:ind+indmax+1); %and truncate r_bin_e @ this point
end

% mark a transition
```

```
t1=r_bin_e(end);
disp(['transition @ r=' num2str(t1)])

%make logrithmically spaced points
egg=logspace(log10(r_bin_e(end)),log10(max(allr)),25);
r_bin_e=[r_bin_e egg(2:end-1)];

% make histogram
histK=histcounts(allr,r_bin_e);
n=histK./(diff(r_bin_e)*W*H*ctr);
r_bin=0.5*(r_bin_e(1:end-1)+r_bin_e(2:end));
r_binl=r_bin_e(1:end-1);
r_binr=r_bin_e(2:end);

rrose=logspace(log10(min(nonzeros(allr))),log10(max(allr)),100);
rmax=max(allr);
nrose=(rrose/rmax).^(-2/3)./(3*pi*rrose.^2*rmax);

if plotyes==1
    figure, subplot(211), loglog(r_bin,histK,'x-'),
    xlabel('radius, m (bin center)'),ylabel('# of drops/bin')
    subplot(212), loglog(r_bin,n,'x-'),
    xlabel('radius, m (bin center)'), ylabel('N(r), drops/m^3')
    ylim([ylim1 ylim2])
    figure, loglog(rcntr10,ncntr10,'x-',r_bin,n,rrose, nrose,'--')
    hold on
    errorbar(r_bin,n,r_bin-r_binl,r_binr-r_bin,'horizontal')
    loglog([t1 t1],[ylim1 ylim2]);
    legend('10 log-spaced bins','composite','rose','bin edges','t1')
    ylim([ylim1 ylim2])
    xlim([xlim1 xlim2])
    xlabel('radius, m (bin center)'), ylabel('N(r), drops/m^3')
end


%% CALCULATE THE TOTAL HEAT TRANSFER
```

```
clear Qd
for i=1:length(r_bin)
    if HTM==1 % Adhikari
        Bi=hi*r_bin_e(i)/kw;
        f = fCalculator(Bi, thetaa);
        Qd(i)=dT*pi*r_bin_e(i)^2*sind(thetaa)^2/(f*r_bin_e(i)/kw+1/(2*hi));
        if exist('pl','var')
          Qd(i)=exp(polyval(pl,log(r_bin_e(i))));
        end
    elseif HTM==2 % Chavan 2016
        Bi=hi*r_bin_e(i)*sind(thetaa)/kw;
        [Nu] = Chavan(Bi,thetaa*pi/180);
        Qd(i)=Nu*kw*r_bin_e(i)*sind(thetaa)*(Tsat-Ts);
    elseif HTM==3 % Kim and Kim (eqn 15)
        Qd(i)=pi*dT*r_bin_e(i)*(r_bin_e(i)-rmin)*(1-cosd(theta))/(A2*r(d)+A3);
    elseif HTM==4 %Miljkovic 2013 Modeling (eqn 13)
        Qd(i)=pi*dT*r_bin_e(i)*(r_bin_e(i)-rmin)/(A2*r_bin_e(i)+A3);
    end
end

r=r_bin;
Qr=n.*Qd;
Ar=n*pi.*r.^2*sind(theta)^2;
Atot=trapz(r,Ar);
Qtot=trapz(r,Qr);
Ntot=trapz(r,n);
disp(['The rate of heat transfer is ' num2str(Qtot) ' Watts']);
disp(['The average % of the area covered by droplets is ' num2str(Atot)]);
disp(['The total drop density is ' num2str(Ntot,'%10.3e')]);

clear Acum Qcum
for i=2:length(r)
    Acum(i)=trapz(r(1:i),Ar(1:i));
    Qcum(i)=trapz(r(1:i),Qr(1:i));
end
```

```
if plotyes==1
    figure, ax=plotyy(r,Ar,r,Qr);
    xlabel('r, m')
    ylabel(ax(2),'n(r)*Q_d(r), W/(m^2*m)')
    ylabel(ax(1),'n(r)*A_b(r), 1/m')

    figure, loglog(r,Acum/Atot,r,Qcum/Qtot,[3.86e-7 3.86e-7],[0 1])
    xlabel('R, m')
    ylabel('% of the contribution to Qtot, Abtot that occurs from r=0 to R')
    legend('A','q"','Location','SouthEast')
end
```

APPENDIX C. DROP TRACKING CODE

The following code tracks drops in condensation videos and analyzes the results. It was used to obtain the data presented in chapters 5 and 6. The code is spread between a few main scripts which call several functions. The main scripts are listed first, followed by the functions which were all located in a folder called "functions". The following outline describes the purpose for each of the main scripts and lists the functions they use. Besides the codes listed below, depending on the conditions of the video, other drop-tracking approaches were also employed, and are implemented in scripts and functions that would replace those listed in steps 2 and 3. For the sake of brevity, the code for the alternative approaches is not included, but can be found in the BYU Thermal Fluids Transport groups folder, or will be provided upon request. When formatting the code to fit into the format of this dissertation it was occasionally necessary to break long lines of code with a hard return. When this was done, a commented out section that says line break is included at the location of the hard return.

1. Use savestruct.m to create a structure containing the frames that will be analyzed. It calls the function VideosliderObj.m.

2. Use ThreshPickerSnakes.m to select the settings to use to track the drops. It calls sliderbw.m (in Appendix A) and ThreshPickerSliderSnakes.m. ThreshPickerSliderSnakes lets the user see the effect of changing the threshold settings, minimum seed size, and edge sensitivity on the drop detection in a single frame. The user can use this information to select appropriate values for each video. Two thresholds are used — one (the higher of the two) determines the "seed" points from which drops grow. The second (the lower one) determines how large drops can grow. The min and max thresholds selected by the user initially based on the output of sliderbw.m are simply to pick reasonable ranges for ThreshPickerSliderSnakes. If too low of a threshold is used in ThreshPickerSliderSnakes the code will crash. Therefore, use sliderbw to select a minimum threshold that shows some distinction between the drops,

and then use ThreshPickerSliderSnakes to select the exact thresholds that will be used in FindDrops.m.

3. Use FindDrops.m to find drops in every frame of the structure. This code uses the parfor function so the code can be run in parallel, resulting in a dramatic speed increase if run on a supercomputer. Calls DistributionGutsHomemadeSnakes.m.

4. Use DropViewer.m to view the results of the drop tracking. If they are satisfactory, proceed and and analyze the results. If not, try (1) rerunning FindDrops.m with different settings, (2) try a different approach than snakes (i.e. active contour modeling), like the hough transform or connected components (found in alternative scripts in the groups folder), or (3) try correcting the results automatically using Corrector.m or manually using CorrectorManual.m (both found in the groups folder).

5. Use MakeDistribPlots3.m to make the distribution function. Calls binningExperimental.m

6. Use MakeRhatPlots.m (calls FindRs.m) to plot $R_{\max 10}$, $\hat{r}$, etc. as a function of time.

Other useful files are listed below and can be found in the groups folder or provided upon request.

- superslider.m is called by several functions and can be downloaded from the matlab file exchange at https://www.mathworks.com/matlabcentral/fileexchange/43285-superslider.

- If the original video was broken up into several segments (parts a, b, c, etc.), use CombineResults.m to combine the results into one results file.

- GetScale.m — Obtains the resolution of the camera using a video of a surface with regularly spaced ribs. The resolution should be recalculate every time the imaging setup changes (e.g. for each zoom on the lens, if the thickness or spacing of the polycarbonate window between the surface the lens changes, etc.) Output is a pixel to micron ratio.

- SubtractBacground.m — If the lighting of the surface varies spatially it can be difficult to select a single threshold value appropriate for the entire image. This code can be used to subtract out the background of a surface.

- One way to detect drop departure is to track individual drops through time, rather than finding their location independently in each frame of the video. A series of scripts and functions located in the folder "ForTrackingThroughTime" does this using a combination of the Hough and Connected Components approaches. It uses many of the functions located in the folder labeled "functions". The code currently works well for low nucleation site densities, where there is good contrast between the drops and the background. The code could be modified to use the active contour modeling approach outlined above; it is expected that using active contour modeling would produce more accurate results.

C.1 savestruct.m

```
%calls VideosliderObj.m

clear all
close all
clc

addpath([cd '\functions'])

%% USER INPUT
pathname='pathname';
filename='1020_16d_250x_5min';
savename=[filename 'd']; %sometimes you may want to break up a long video into
%several shorter sections.  This could be specified by appending a character
%at the end, e.g. part a, b, c, etc.
s=1;
%%

vidObj = VideoReader([pathname '\' filename '.mov']);
vidWidth = vidObj.Width;
vidHeight = vidObj.Height;
numFrames = vidObj.NumberOfFrames;
fr=vidObj.FrameRate;
```

```
VideosliderObj(vidObj,numFrames)
startFrame=input('Which frame do you want to start on? ');
endFrame=input('Which frame do you want to end with? ');
%startFrame=5100;
%endFrame=5900;
%% to choose a new rectangle
title('Click and drag a box to crop the image')
[I,rect]=imcrop;
%rect=[493.510000000000,0.510000000000000,1070.98000000000,1079.98000000000];
mov = struct('cdata',zeros(round(rect(4)),round(rect(3))),'fr',[],'s',[]);

ctr=0;
for k=startFrame:s:endFrame
    ctr=ctr+1;
    mov(ctr).cdata = rgb2gray(imcrop(read(vidObj,k),rect));
%     mov(ctr).cdata = imcrop(read(vidObj,k),rect);
%     imwrite(imcrop(read(vidObj,k),rect),[filename num2str(k) '.tif']);
    disp(['Analyzed frame number ' num2str(k)])
end


mov(1).fr=fr;
mov(1).s=s;
save([cd '\structures\' savename])
```

C.2 ThreshPickerSnakes.m

```
load('structurename') %or run this after running save struct
frameNumber=1;
A=mov(frameNumber).cdata;

sliderbw(A)
minthresh=input('What is the lowest threshold you want to use? ');
maxthresh=input('What is the highest threshold you want to use? ');
```

```
ThreshPickerSliderSnakes(A,minthresh, maxthresh)
```

C.3 FindDrops.m

```
% Author: Kimberly Stevens
% email: kimst12@gmail.com

close all
clear all
clc

addpath([cd '\functions'])
addpath([cd '\structures'])
addpath([cd '\results'])


%% User Input=============================================================
thresh=[.43,.46,.9,2];
dT=0;
% micronperpix=.772338*1e-6; %500x
micronperpix=2.124208*1e-6; %250x

strutname='1022_13d_250x_5mind';
tracktype='s';
filenamer=['results_' strutname '_' tracktype];

load(strutname);
drop(1).H=size(mov(1).cdata,1);
drop(1).W=size(mov(1).cdata,2);
drop(1).tracktype=tracktype;
drop(1).fr=mov(1).fr;
drop(1).s=mov(1).s;
drop(1).micronperpix=micronperpix;
drop(1).dT=dT;
```

```
drop(1).thresh=thresh;

startFrame=1;
endFrame=length(mov);
objpolarity='bright';
%% End User Input============================================================

fr=mov(1).fr;
s=mov(1).s;
fr=fr/s;
t=0:1/fr:length(mov)/fr-1/fr;

parfor F=startFrame:endFrame
    disp(['Frame #: ' num2str(F)])
    [ r,centers ] = DistributionGutsHomemadeSnakes(mov(F) % (line break)
    .cdata,thresh(1),thresh(2),thresh(3),thresh(4),F,0);
    drop(F).x=centers(:,1);
    drop(F).y=centers(:,2);
    drop(F).r=r;
end

save(filenamer,'drop')
disp('Finished!')
```

C.4 DropViewer.m

```
num2view=2;

strutname='1020_16a_250x_5mina';
filenameR=['results_' strutname '_s2'];
load(filenameR);
load(strutname);
% binningExperimental
drop1=drop;
```

```
if num2view==2
    filenameR=['results_' strutname '_s3'];
    load(filenameR);
%     binningExperimental
    drop2=drop;
end

for F=1:length(drop)
%     to visualize
    if num2view==2
        subplot(121)
    end
    imshow(mov(F).cdata)
    viscircles([drop1(F).x drop1(F).y], %(line break)
    drop1(F).r,'EdgeColor','r','DrawBackgroundCircle',0,'LineWidth',.5);
    title(['Frame #: ' num2str(F) '/' num2str(size(mov,2))])
    if num2view==2
        subplot(122)
        imshow(mov(F).cdata)
        viscircles([drop2(F).x drop2(F).y],  %(line break)
        drop2(F).r,'EdgeColor','r','DrawBackgroundCircle',0,'LineWidth',.5);
        title(['Frame #: ' num2str(F) '/' num2str(size(mov,2))])
    end
    drawnow
end
```

C.5 MakeDistribPlots3.m

```
close all
clear all
clc
fontname='Times';
fontsize=10;

%% User input
```

```
bintype=1; %should the bin width be variable (type 1) or a
% constant 10% (type 2?)
figname='5min';
numlines=3;
structname{1}='1015_19a_250x_5minall';
prefix{1}='results';
postfix{1}='s2';
structname{2}='1020_16a_250x_5minall';
prefix{2}='results';
postfix{2}='s3';
structname{3}='1022_13b_250x_5minall';
prefix{3}='results';
postfix{3}='s';
structname{4}='1015_19e_250x_5minall';
prefix{4}='results';
postfix{4}='s';
figwid=3;
figheight=3;
lgdpos=[0.21 0.18 0.49 0.26];
xlimit=[1e-5 1e-3];
ylimit=[1e7 2e13];
%% End User Input
pc={'r','b','g','c'};

addpath([cd '\functions'])
addpath([cd '\structures'])
addpath([cd '\structures\AnalyzedStructures'])
addpath([cd '\results'])


for k=1:numlines
    load([prefix{k} '_' structname{k} '_' postfix{k}]);
    binningExperimental
    r=r10o;
    if bintype==1
        n=n10o;
```

```
    else
        n=n10o2;
    end
    dT{k}=['\DeltaT = ' num2str(drop(1).dT) ' ^oC'];
    hold on
    figure(9), h(k)=loglog(r,n,pc{k});
    hold on
    if bintype==1
        fill([[(1-bwvect).*r]';flipud([(1+bwvect).*r]')], % (line break)
        [n';flipud(n')],pc{k},'linestyle','none');
        alpha(0.1)
        p1=loglog((1-bwvect).*r,n,[pc{k} '-.']);
        p1.Color(4) = 0.25;
        p1=loglog((1+bwvect).*r,n,[pc{k} '-.']);
        p1.Color(4) = 0.25;
    else
        fill([[(1-bw).*r]';flipud([(1+bw).*r]')],  % (line break)
        [n';flipud(n')],pc{k},'linestyle','none');
        alpha(0.1)
        p1=loglog((1-bw).*r,n,[pc{k} '-.']);
        p1.Color(4) = 0.25;
        p1=loglog((1+bw).*r,n,[pc{k} '-.']);
        p1.Color(4) = 0.25;
    end
end
xlabel('{\it r} (m)')
ylabel('{\it N} (drops/m^3)')


figure(9), hold on
rmax=4e-4;
rrose=logspace(log10(min(nonzeros(allr))),log10(rmax),100);
nrose=(rrose/rmax).^(-2/3)./(3*pi*rrose.^2*rmax);
h(end+1)=loglog(rrose,nrose,'k--','LineWidth',1);

lgd=legend(h,'\DeltaT = 2.52 ^oC','\DeltaT = 4.54 ^oC',  % (line break)
```

```
'\DeltaT = 5.69 ^oC', 'Le Fevre and Rose');

legend('boxoff')
set(lgd,'Position',lgdpos)
xlim(xlimit)
ylim(ylimit)
ax=gca;
ax.TickLength = [0.02 0];
xticks([1e-6 1e-5 1e-4 1e-3 1e-2])
set(gca,'FontSize',fontsize,'FontName',fontname);
set(gcf,'PaperPosition',[1 1 figwid figheight]);
set(gcf, 'Units', 'Inches', 'InnerPosition', [5 5 figwid figheight]);
print('-depsc','-r600',[cd '\figures\' figname]);
print('-dpng','-r600',[cd '\figures\' figname]);
```

C.6 MakeRhatPlots.m

Additional parts of this code can be found in the version found on the groups folder.

```
close all
clear all
clc

fontname='Times';
fontsize=10;

addpath(genpath([cd '\results']))
addpath(genpath([cd '\functions']))

filenames=dir('results\constTemp\all\*.mat');
figure,

%% plot for paper
for j=1:size(filenames,1)
    load(filenames(j).name)
    c=strsplit(filenames(j).name,'_');
```

```
    if strcmp(c{2},'1015')
        pm='bo';
    elseif strcmp(c{2},'1020')
        pm='r^';
    else
        pm='gs';
    end
    FindRs
    rmax10(j)=mean(rm10);
    dT(j)= str2num(drop(1).dT);
    vidTime(j)=drop(1).videoTime;

    figure(1),
    hold on
    plot(vidTime(j),rmax10(j),pm)
end
%%
xlabel('Elapsed Time (min)')
ylabel('{\itr}_{max 10} (m)')
h1=plot(NaN,NaN,'bo',NaN,NaN,'r^',NaN,NaN,'gs');
lgd=legend(h1,'\DeltaT = 2.52 ^oC','\DeltaT = 4.54 ^oC', % (line break)
'\DeltaT =5.69 ^oC','Location','northeastoutside');
legend('boxon')
% set(lgd,'Position',lgdpos)
ax=gca;
box on
ax.TickLength = [0.02 0];
set(gca,'FontSize',fontsize,'FontName',fontname);
set(gcf,'PaperPosition',[1 1 4.5 3]);
set(gcf, 'Units', 'Inches', 'InnerPosition', [5 5 4.5 3]);
print('-depsc','-r600',[cd '\figures\rmax']);
print('-dpng','-r600',[cd '\figures\rmax']);
```

C.7 VideosliderObj.m

```
function VideosliderObj(vidObj,endFrame)
%VIDEOSLIDER Allows a user to scroll through a video
%Kim Stevens, kimst12@gmail.com
%called by savestruct

    hFig = figure('menu','none');
    hAx = axes('Parent',hFig);
    uicontrol('Style', 'slider', 'Value',endFrame, 'Callback', %(line break)
    @sliderCallback, 'Position',[150 5 300 20], 'Max', endFrame,%(line break)
    'Min',1,'SliderStep', [1 1]/(endFrame));
    T=1;
    imshow(read(vidObj,T),'Parent',hAx)
    title('Use slider to scroll through video')

    function sliderCallback(hObject, evt)
    T=round(get(hObject, 'Value'));
%     imshow(mov(T).cdata)
    imshow(read(vidObj,T))
    title(num2str(T))


end
end
```

C.8 ThreshPickerSliderSnakes.m

```
function ThreshPickerSliderSnakes(A,minthresh, maxthresh)
%Kim Stevens, kimst12@gmail.com

    hFig = figure('menu','none');
    hAx = axes('Parent',hFig);
    x=superSlider(gcf,'position',[0.75,.15,0.25,0.03],%(line break)
    'numslides',2,'max',maxthresh,'min',minthresh,%(line break)
    'stepsize',.01,'Callback',@sliderCallback);
    y=superSlider(gcf,'position',[0.75,.1,0.25,0.03],'numslides',%(line break)
```

```
    1,'max',.95,'min',.9,'stepsize',.01,'Callback',@sliderCallback2);
    z=superSlider(gcf,'position',[0.75,.05,0.25,0.03], %(line break)
    'numslides',1,'max',.3,'min',.01,'stepsize',.01, %(line break)
    'Callback',@sliderCallback3);

    imshow(A,'Parent',hAx), title('Choose thresholds by using % (line break)
    slider. Do not drag bar.')%Make sure you have the correct slider selected
    % (gray) then use the bars on the end to move each slider distinct steps
    global T1 T2 T3 rmin
    T1=maxthresh;
    T2=maxthresh;
    T3=.9;
    rmin=10;

    function sliderCallback(hObject, ~)
    infoMatrix = get(hObject, 'UserData');
    T1=infoMatrix(1,1);
    T2=infoMatrix(1,2);

    [TargetRadii,TargetCenters]=DistributionGutsHomemadeSnakes%(line break)
    (A,T1,T2,T3,rmin,1,0);
    %show the circles
    subplot('position',[0 .15 .75 .75]),
    imshow(A)
    viscircles(TargetCenters, TargetRadii,'EdgeColor','g', % (line break)
    'DrawBackgroundCircle',0,'LineWidth',1);
    title(['T1: ' num2str(T1) '; T2: ' num2str(T2) '; T3: % (line break)
    ' num2str(T3) '; rmin: ' num2str(rmin)])
    subplot('position',[.75 .65 .25 .25]),imshow(im2bw(A,T1)),
    title('Negative energy')
    subplot('position',[.75 .25 .25 .25]),
    imshow(imfill(im2bw(A,T2),'holes')),title('Seed points')

    end

function sliderCallback2(hObject, ~)
```

```
    infoMatrix = get(hObject, 'UserData');
    T3=infoMatrix(1,1);

    [TargetRadii,TargetCenters]=DistributionGutsHomemadeSnakes%(line break)
    ( A,T1,T2,T3,rmin,1,0);
    %show the circles
    subplot('position',[0 .15 .75 .75]),
    imshow(A)
    viscircles(TargetCenters, TargetRadii,'EdgeColor','g', % (line break)
    'DrawBackgroundCircle',0,'LineWidth',1);
    title(['T1: ' num2str(T1) '; T2: ' num2str(T2) '; T3:  % (line break)
    ' num2str(T3) '; rmin: ' num2str(rmin)])
    subplot('position',[.75 .65 .25 .25]),
    imshow(im2bw(A,T1)),title('Negative energy')
    subplot('position',[.75 .25 .25 .25]),
    imshow(imfill(im2bw(A,T2),'holes')),title('Seed points')

end

function sliderCallback3(hObject, ~)
    infoMatrix = get(hObject, 'UserData');
    rmin=infoMatrix(1,1)*100;

    [TargetRadii,TargetCenters]=DistributionGutsHomemadeSnakes % (line break)
    ( A,T1,T2,T3,rmin,1,0);
    %show the circles
    subplot('position',[0 .15 .75 .75]),
    imshow(A)
    viscircles(TargetCenters, TargetRadii,'EdgeColor','g', % (line break)
    'DrawBackgroundCircle',0,'LineWidth',1);
    title(['T1: ' num2str(T1) '; T2: ' num2str(T2) '; T3: % (line break)
    ' num2str(T3) '; rmin: ' num2str(rmin)])
    subplot('position',[.75 .65 .25 .25]),
    imshow(im2bw(A,T1)),title('Negative energy')
    subplot('position',[.75 .25 .25 .25]),
    imshow(imfill(im2bw(A,T2),'holes')),
```

```
    title('Seed points')

end
end
```

C.9 DistributionGutsHomemadeSnakes.m

```
B=im2bw(A,T1);
C=imfill(im2bw(A,T2),'holes');
stats=regionprops(C,'Area','Centroid');
drop_ctr=0;
Radii=zeros(length(stats),1);
Centers=zeros(length(stats),2);
for i=1:length(stats)
    r=(stats(i).Area/3.14)^.5;
    if r>rmin
        drop_ctr=drop_ctr+1;
        center=stats(i).Centroid;
        e=AvgInensity(B, center, r);
%         rctr=0;
        while e>T3
            r=r+1;
            e = AvgInensity( B, center, r);
        end

        Radii(drop_ctr)=r;
        Centers(drop_ctr,:)=center;
    end
end

%remove overlapping circles (removes the smaller one)
overlap=OverlappingCircles(Centers,Radii );
Radii(overlap)=[];
Centers(overlap,:)=[];
```

```
if showresults==1
    imshow(A)
    viscircles(Centers, Radii,'EdgeColor','r', % (line break)
    'DrawBackgroundCircle',0,'LineWidth',.5);
    title(['Start Frame #: ' num2str(F)])
end
end
```

C.10 binningExperimental.m

```
%% calculate drop statistics
micronperpix=drop(1).micronperpix;
ctr=size(drop,2);
W=drop(1).W*micronperpix;
H=drop(1).H*micronperpix;

biggest=0;
for i=1:length(drop)
    if length(drop(i).r)>biggest
        biggest=length(drop(i).r);
    end
end
allr=zeros(length(drop),biggest);
for i=1:length(drop)
    rt=drop(i).r*micronperpix;
    allr(i,1:length(rt))=rt;
end
allr=nonzeros(allr);

% traditional bins
r20=logspace(log10(min(nonzeros(allr))),log10(max(allr)),20);
hist20=histcounts(allr,r20); %convert into #/m^2 averaged over time
n20=hist20./(diff(r20)*(W*H)*ctr);
rcntr20=0.5*(r20(1:end-1)+r20(2:end));
rcntr20l=r20(1:end-1);
```

```
rcntr20r=r20(2:end);

% overlapping bins variable bin width
r10o=logspace(log10(min(nonzeros(allr))),log10(max(allr)),100);
n=zeros(size(r10o));
bwvect=zeros(size(r10o));
for i=1:length(r10o)
    bw=.1;
    n(i)=sum(allr<=r10o(i)*(1+bw) & allr>r10o(i)*(1-bw));
    while(n(i)<1000)
        bw=bw+.01;
        if bw>=.2
            break
        end
        n(i)=sum(allr<=r10o(i)*(1+bw) & allr>r10o(i)*(1-bw));
    end
    bwvect(i)=bw;
end
n10o=n./(W*H*ctr*r10o.*bwvect*2);

% overlapping bins
bw=.1;
r10o=logspace(log10(min(nonzeros(allr))),log10(max(allr)),100);
r_bin_c=r10o;
n=zeros(size(r_bin_c));
for i=1:length(r_bin_c)
    n(i)=sum(allr<=r_bin_c(i)*(1+bw) & allr>r_bin_c(i)*(1-bw));
end
n10o2=n./(W*H*ctr*r_bin_c*bw*2);

% % even number of drops in each bin
% r_bin_e = binbynumexp(allr,10000);
% hist_e=histcounts(allr,r_bin_e);
% n_e=hist_e./(diff(r_bin_e)*(W*H)*ctr);
% r_e=0.5*(r_bin_e(1:end-1)+r_bin_e(2:end));
```

```
% figure, loglog(rcntr10,hist10,'x-',rcntr20,hist20,'x-')
% figure, loglog(r_e,hist_e,'x-')

figure, loglog(r10o,n10o,'x-',r10o,n10o2,'x-',rcntr20,n20,'x-')
legend('100 overlapping (+/- 10-20%)','100 overlapping % (line break)
(+/- 10%)','20 regular')
xlabel('radius, m (bin center)'), ylabel('N(r), drops/m^3')
```

C.11 FindRs.m

```
%% calculate drop statistics
fr=drop(1).fr;
micronperpix=drop(1).micronperpix;
t=0:1/fr:size(drop,2)/fr-1/fr;

clear rm numdrops rm1 rm5 rm10 rm
rm1=zeros(1,length(drop));
numdrops=zeros(1,length(drop));
rm5=zeros(1,length(drop));
rm10=zeros(1,length(drop));
rm=zeros(1,length(drop));

biggest=0;
for i=1:length(drop)
    if length(drop(i).r)>biggest
        biggest=length(drop(i).r);
    end
end
allr=zeros(length(drop),biggest);
for i=1:length(drop)
    rt=drop(i).r*micronperpix;
    allr(i,1:length(rt))=rt;
end
allr=nonzeros(allr);
```

```
for i=1:length(drop)
    rt=sort(nonzeros(drop(i).r),'descend')*micronperpix;
    rm1(i)=rt(1);
    numdrops(i)=length(rt);
    rm5(i)=mean(rt(1:5));
    rm10(i)=mean(rt(1:10));
    rm(i)=mean(rt);
end

ctr=size(drop,2);
W=drop(1).W*micronperpix;
H=drop(1).H*micronperpix;

% figure, plotyy(t,[rm1; rm5; rm10; rm],t,numdrops)
% xlabel('time, s')
% ylabel('radius, m')
% legend('max','top 5','top 10','average','number')

figure, plot(t,[rm1; rm5; rm10; rm])
xlabel('time, s')
ylabel('radius, m')
legend('max','top 5','top 10','average')
ylim([0 7e-4])

set(gca,'FontSize',fontsize,'FontName',fontname);
set(gcf,'PaperPosition',[1 1 3 3]);
set(gcf, 'Units', 'Inches', 'InnerPosition', [5 5 3 3]);
% print('-depsc','-r600',[cd '\figures\TrackR' strutname num2str(F)]);
% print('-dpng','-r600',[cd '\figures\TrackR' strutname num2str(F)]);
```

APPENDIX D. COPPER OXIDE FABRICATION INSTRUCTIONS

The following instructions describe the procedures for making copper oxide superhydrophobic surfaces, as described in chapter 6.

D.1 Pre-Steps

1. Cut off of diameter circular Copper 102 rod 1/8" or 1/4" disks.
2. Grind down faces of the disk until most of the extremely deep grooves are gone.
3. Drill a hole in the side of the sample with a #55 drill bit. Hole needs to go half-way through the sample (7/16").

D.2 Polish and Clean

1. Polish the Cu surface. Go to the polish room in CB 104. Use the polishing wheel as follows:
   (a) Find polish cylinder and ring
   (b) Place cylinder on wheel and turn speed to 150 RPM
   (c) Turn on water and wet wheel
   (d) Turn off water
   (e) Turn off rotation
   (f) Start with 200 grit sandpaper
   (g) Stick paper on the cylinder
   (h) Turn on wheel to 75 RPM and turn on water
   (i) Once paper is completely wet, begin running copper sample along sand grains
   (j) Do random polish

(k) Sand in one direction

(l) Rotate 90° and sand other direction

(m) Repeat with 400, 600, 800, 1200, and 1200 Fine grit, with an increase in 25 RPM for each increase in grit size after 400 RPM. i.e: 400 Grit → 75 RPM, 600 Grit → 100 RPM, 800 Grit → 125 RPM, 1200/1200 Fine Grit → 150 RPM

(n) Locate Alumina pad (pitch 1 μm)

(o) Find Alumina particles of 1 μm diameter

(p) Place Imperial pad and put alumina paste in the center of pad

(q) Turn spinner to 150 RPM

(r) Move outwards and add paste as needed

(s) Blow off with air

2. Clean in an ultrasonic bath with acetone for 20 min 2X.

3. Change out acetone after each saunicaction

4. Rinse with ethanol, IPA, and DI water 5X

5. Dry with N2 or Ar

6. Make 2.0 M HCL Solution, ratios as follows: 165-167 mL HCL / 1 L DI Water (ph of solution should be about -0.2)

7. Place copper in solution for 20 min

8. Triple rinse with DI water (Rinse dry, rinse dry, rinse dry)

9. Dry with N2 or Ar

D.3 Chemical Oxidation

1. Make Alkaline solution to chemically oxidize and create nanostructures with the following ratios: NaClO2, NaOH, Na3PO412H2O, and DI water (3.75:5:10:100 wt %), i.e. NaClO2: 3.75 g; NaOH: 5 g; Na3PO412H2O: 10 g; DI Water: 100 mL (100 g)

2. Heat solution to 96 °C (96 3 °C)

3. Use thermometer to monitor temperature

4. Keep temperature on the upper end of 96 3 °C

5. Place copper sample in solution for either 5, 10, 20, or 45 min depending on size of desired nanostructures (see [35].

6. Rinse in DI water 5 times

7. Dry with N2 or Ar

D.4 Functionalization

D.4.1 PTFE

1. When using teflon coating, put on two coats of Teflon

2. Create 2% by weight Teflon solution. (1 gram of 6% Teflon for every 2 g of FC-40)

3. Super-glue copper sample to center of silicon wafer.

4. Place wafer on headway spinner. Set spinner to 3000 RPM and spin for 30 sec

5. Place copper sample on hot-plate that has been pre-heated to 180 C

6. Use laser thermometer to observe the surface temp of the copper block. Let the sample heat until it is at 180 °C, then set a timer for 10 min and keep the copper block on the hot plate for that amount of time.

7. Allow sample to cool for 15 min.

D.4.2 Glaco

1. Pour out 20-25 mL of Glaco into a small beaker.

2. Pre-heat hot plate to 150 °C

3. Dip sample into Glaco moving it up and down in the solution

4. Remove sample from Glaco and place on hot plate for 30 min

5. Remove sample from hot plate and let it cool for 3 min

6. Repeat steps 3-5 3X

APPENDIX E. CONDENSATION CHAMBER CONSTRUCTION NOTES

The follow notes describe materials used in the construction of the vacuum chamber used for condensation. The presence of noncondensable gases (NCG) has significant implications for heat transfer, requiring construction of a chamber that could maintain a vacuum for extended periods of time. To maintain a vacuum, the chamber needs to minimize pressure rise due to leaks allowing entrance of air from outside the chamber, and outgassing of components interior to the chamber. Outgassing is liberation of gases and vapors from the walls of and components interior to a vacuum chamber, and includes vaporization, desorption, diffusion, and permeation [175]. While all materials outgass, some materials are much worse than others, so care is required when selecting materials and components for vacuum chamber construction. The National Aeronautics and Space Administration maintains a repository containing information regarding outgassing rates of common materials, which was used select materials used in construction [176]. The vacuum chamber was constructed in house and machined from stainless steel. Access ports consisted of KF flanges welded onto the outside of the machined chamber, and all exterior valves and connections were KF flange. The front and rear of the vacuum chamber are constructed of polycarbonate. The front of the chamber is transparent to allow visual access into the chamber. The rear of the chamber consists of a piece of polycarbonate with a 7/8" hole in the center into which a 7/8" copper block was epoxied use Loctite EA 1C adhesive, which is a vacuum compatible adhesive. After the copper block was epoxied in place, the polycarbonate-copper block assembly was faced off so that the copper was flush with the polycarbonate, and Celvaseal High Vacuum Leak Sealant Spray was used on the reverse side to ensure a good vacuum seal. The rubber o-rings between the chamber body and front and rear were constructed of Viton. The holder used to clamp the condensing surface in place was 3D printed from PLA plastic. Viton, polycarbonate, the epoxy, PLA, and stainless steel were all selected to minimize the leak and outgassing rates.

Exterior to the chamber, rigid thermocouples from Omega (TJC36-CPSS-020E-6) were used to ensure precise placement. The heat exchanger was purchased from Custom Thermoelectric (WBA-1.00-0.60-CU-CH)